DESIGN AND CONTROL OF HYPER REDUNDANT MULTI-SEGMENT PNEUMATIC-DRIVEN CONTINUUM ROBOT

ZHAO QINGXIANG

PhD

The Hong Kong Polytechnic University

2022

The Hong Kong Polytechnic University

Department of Mechanical Engineering

Design and Control of Hyper Redundant Multi-Segment Pneumatic-Driven Continuum Robot

Zhao Qingxiang

A thesis submitted in partial fulfilment of the requirements for the degree of Doctor of Philosophy

Jun 2022

Certificate of Originality

I hereby declare that this thesis is my own work and that, to the best of my knowledge and belief, it reproduces no material previously published or written, nor material that has been accepted for the award of any other degree or diploma, except where due acknowledgement has been made in the text.

_____(Signature)

Zhao Qingxiang (Name of Student)

Abstract

Automatic equipment plays an increasingly important role in human daily life, for which can free human beings from tedious and repetitive tasks, can improve effectiveness and can standardize the workflow of implementation. Therefore, the automation level of a country somehow marks the industrialization degree and the development of manufacturing industry. Robot arms are typical representatives in automatic equipment. The wide application of them, such as in manufacturing industry, medical surgery, and search and rescue, have contributed to effectiveness enhancement and cost decrease. Especially with the rapid development of Artificial Intelligence (AI), robot arms are capable of completing complicated tasks requiring little human intervention. This indeed promotes the flexibility in achieving diversified tasks, and the collaboration with human workers or with other robots creates more possibility in replacing traditional working steps. Conventionally, rigid robot arms are common in applications because of the high pose precision, load-carrying performance and robustness. However, due to their inherent structural characteristics including rigid robot body, bulky encoders, motors and transmission mechanisms, rigid robot arms may not be applicable in constrained environments.

In contrast, soft robots that are made of hyper elastic materials exhibit obvious advantages in terms of the safety issue, cost, flexibility, dexterity, and compliance. Through diversified fabrication technologies, many soft robots have been created for specific scenarios, like exploring undersea scenarios and minimally invasive surgery (MIS). Biology has inspired researchers to explore soft robots that are capable of locomotion and manipulation in cluttered environments. Therefore,

researchers desired to develop robots with flexible body. Continuum robots whose body is similar to snakes, elephant's trunk and octopus tentacles, have drawn significant research interest in the past two decades. The definition of a continuum robot can be a continuously deformable, infinite DoF and elastic manipulator and they can mitigate some drawbacks of cumbersome rigid robot arms. There are generally three chambers radially distributed inside a single soft segment, where the longitudinal forces along them lead to length difference in each chamber, such that the deformation towards omni direction occurs. The soft material and structure also render continuum robots safe to touch, which further benefits manipulating soft objects, working in narrow space and safe collaboration with human. On the other hand, the high degree of compliance also poses difficulty in against external loads, attracting significant interest of designing robust controllers. Continuum robots are also easy to be disturbed by external forces, making a traditional analysis-based controller infeasible. Researchers in recent years paid significant attention to designing robust controllers for diversified continuum robots.

Although remarkable achievements have been made in continuum robotics, pursuing better actuation mechanisms, finding sensors and achieving high accuracy of control schemes are still hot spots for researchers. As externally configured sensors like stereocameras, can real-time sense the shape and the tip configuration of the continuum robot, this sensing mechanism is not able to work in constrained and occluded scenarios. The first contribution of this thesis is proposing a shape estimation module and a closed-loop controller, forming visualization manipulation system. Strain gauges were employed to act as embedded sensors to sense the robot deformation, and curve fitting algorithms connect the predicted key points by LSTM-MLP NNs. This data-driven method provides a simple solution with the mapping between sensor readings and the true shape configuration. Closed-loop controller scheme integrating accurate feedback contributes to high accuracy of tip configuration control, and the shape reconstruction module can not only sense the shape but the tip position, so that the controller directly obtains the real-time

tip position. Data-driven method was also considered to simplify the control architecture, which was based on the inverse of Jacobian matrix. An adaptive step distance mechanism was proposed to adjust the step distance between steps to automatically bypass the obstacles. Specifically, when the tip position is close to the destination, smaller step distance was set, and when the deviation between the planned and the actual is larger, showing obstacles or external forces present, robot system considered bigger step distance to offset the influence.

Additionally, it would reduce complexity of designing controller if the external forces could be accurately obtained, including the acting direction, position and the magnitude. Working in unstructured environment means any external force could present uncertainly, and the shape of the manipulator is jointly determined by the external force and actuation inputs. The second objective of this thesis is to propose a method to estimate the information of the external force. Similarly, proprioceptive mechanism should be pursued to sense the uncertain external force (UEF). Being different from some existing works, we aim at estimating the UEF acting at the circumferential surface of the soft manipulator, and the area where an UEF is likely to present was labelled by a 2D map. Each area was marked by a row position and a column position accordingly. Once detecting the presence of an external force, the column position indirectly reflects the deviation orientation and the row position was related to the deviation degree. Therefore, Hidden Markov Model(HMM) was employed to estimate the column position. Then, to find the corresponding row position and the magnitude, virtual work principle assuming the robot was in balance was utilized. To simplify the calculation process and to pursue accurate estimation, iteration algorithm integrating an optimization factor was designed in finding the magnitude.

Apart from investigating deformation and load-compensation characteristics, this thesis also proposed a novel mechanism that enables omnidirectional bending and continuous rotation simultaneously. The challenge lies achieving rotation along the deformed backbone while maintaining the shape unchanged. To the best

of our knowledge, this is the first rotational continuum robot with the capability of omnidirectional bending and rotation. To address the tube twining issue between the actuators and the manipulator, a slip ring was employed to decouple the transmission of the pressurized air. As the newly added revolve joint did not expand the task space, the motion velocity of the manipulator could be enhanced. Based on this, an optimization algorithm was proposed using Genetic Algorithm (GA) to control the tip configuration with the objective of time effectiveness. The continuous rotation along the deformed backbone was achieved by integrating the motion of the base and the deformation. This thesis additionally designed the algorithm to control the rotational behaviour.

Acknowledgements

Looking back my Ph.D. period, I shall show my sincere thanks to my supervisor, Dr. Henry K. Chu. He gave me an opportunity to pursue what I want to do. I still clearly remember the first day when I met him, and he clarified me the research orientation very carefully. The 102 papers he provided to me at that day inspired me significantly for the subsequent research. His patience and profession in reviewing my manuscripts, discussing key scientific problems and instructing students have deeply impressed me, all of which gives me an outstanding image of being a supervisor. Staff members in PolyU also helped a lot for in rear services. Mr. YUEN, the technician in our lab, always keeps the lab in a tidy way and provided us with a nice research atmosphere. Michelle always clearly tells me the details when I have any administrative issues. Technician officer, Mr Jack, also played an important role in my research. He instructed me patiently in manufacturing some key components of my robot platform. I will also show my thanks to my friends. Your practical help and emotional assistance always kept me accompany during the tough time I spent in the past years. Impressively, Zhiyi Jiang never lost confidence in preparing the ICRA publication. His meticulous habit and patience are necessary to this project. I will appreciate Sam, Kaicheng, Jiacong, Wang shuai, Tommy and Athena for your instruction and cooperation.

Finally, I would express thanks to my parents. Although we generally do not have frequent communication on every aspect of our life, I know that your love is always surrounding me wherever I am. Your kindness and support encourage my whole life.

Contents

List of Figures

List of Tables

Chapter 1

Introduction

Remarkable achievements in technical innovations have bettered daily life of human beings. Traditional manual production modes can not satisfy the fundamental requirements of social development, so they should be upgraded and replaced by advanced automatic equipment, which provides high-level, effective, low-cost, and high-quality products. The implementation of 'Industrial 4.0' and 'Made in China 2025' promotes the advancement of intelligent instruments. The whole industrialization ecosystem has been developed a lot including high-end instruments, complicated industrial software, and industrial communication systems.

Robot is one of the typical representative in modern industrialization. It covers knowledge ranging from mechanical design, manufacturing, mechanics, sensors, actuators, to algorithms, etc. Robots also play a significant role in modern society. Tedious and repetitive jobs have gradually be modified or replaced by industrial robots, and the work done by robots sometimes is with higher quality. Rapid programming technology enables flexible motion for robots, which is also a fundamental requirement in actual application. Robots also exhibit smarter performance. They will replace humans in many kinds of dull, dirty and dangerous jobs, relieving them for more creative pursuits. 'Industrial 4.0' describes a bright future of intelligent and productive factories where the production pipelines are optimized real-time in response to the variations arising from factors like socio-economic and political changes. Intelligent robot systems would make this possible. These robots can complete tasks in unstructured and dynamic environments, and can

learn to collaborate with humans and other robots, while learning new skills and sharing knowledge with them. Such robots can be rented cheaply by small and medium enterprises. The global changes will give rise to robot-based automation at an affordable cost. Typically, by connecting rigid bars in series with 6 Degree of Freedom (DoFs), a dexterous robot arm can be built. Equipped with a proper end effector, the motion of the robot arm can bring the end effector into diversified position and orientation in its workspace. Similarly, once mounting the robot arms on a mobile platform, the task space is greatly expanded, so that a mobile robot can be more flexible and contribute more to human beings. Diversified robots have been successfully applied in manufacturing, medical surgery, exploration and rescue, etc.

Conventional rigid robot arms are typical representatives, and manipulation with different end effectors has indeed benefited many aspects. However, the shortcomings of rigid robot arms are also obvious, such as high cost in maintenance, cumbersome body, and unsafe to perform collaborative with human. As a functional replenish for rigid robot arms, soft robots gradually attracted much attention in the past two decades owing to their great advantages. Organized by soft or elastic materials and actuated by effective mechanisms, novel continuum robots have achieved remarkable results in the past years. A soft robot characterizes light weight, high degree of compliance, low cost, and miniature in size. Continuum robot is one hot topic in this research community. The novel fabrication methods, appropriate sensors, actuators, and algorithms together lead to better continuum robot systems and broaden application horizons.

The flexible body is generally realized by soft materials or local rigid rings connected flexibly. Low Young's Modulus of material enables safe contact with human, and this also provides capabilities of easy interaction and manipulation. Fig. 1.1 shows several common continuum robots with slender backbone, enabling navigation inside constrained environments and manipulating objects dexterously equipped with proper end effectors. Generally, its motion is realized by unsym-

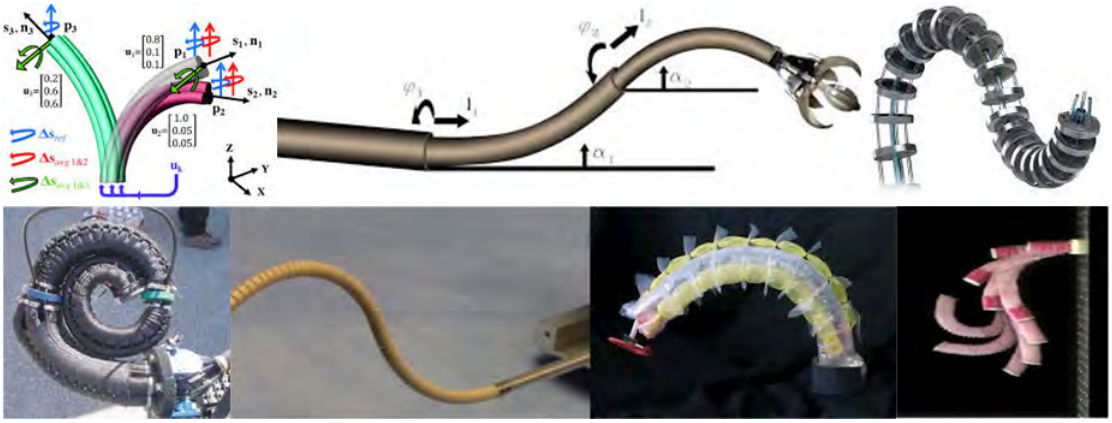

Fig. 1.1. Some common continuum robots.

metrical force or bending moment acted on the flexible body, and the shape is like an arch after deformation. Concentric continuum robot is a special case. It is assembled by multiple pre-deformed arc NiTi tendons. The tendons with smaller curvature are configured through the one with bigger curvature, and the elongation from its host tube make the whole manipulator deformable towards different direction.

1.1 Basics of Continuum Robot

To mitigate the shortcomings of conventional rigid robots, researchers have tried to find more inspirations from other fields. Biology provides examples to investigate novel soft robots. Flexible animals like snakes, elephant's trunks, tongues, and octopus tentacles have inspired researchers to develop continuum robots based on their incredible capabilities in locomotion, manipulation, and dexterity in confined environments. The origin of continuum robot can date back early to 1960s (see [1] page 110 and [2] page 115). They were organized by spaced joints and form the shape of soft body. However, the continuum robots characterized low precision and poor payload capacity. In 1970s, sustained development in this area re-emerged, with pioneering work achieved by *Hirose* and his team [3]. During this time, industrial continuum manipulators were developed including spine robot, and miniature fluid-driven actuators. Other remarkable contribution continued in many new and innovative applications, in both commercial and academic research

forums [4]. Later in 1980s, continuum robots stepped further into industrial scenarios, where the flexible and slender shapes were applicable in spray-painting [5] and grasping [6]. Before 1990s, many continuum robots were not well controlled due to the marginal progress in computation performance and control algorithms. As stated in [7] and [3], significant progress was achieved in 1990s in modelling the controller of continuum robots, which laid theoretical foundation for future models. The first decade of the 21st century witnessed lots of advancements in design, fabrication, modelling and application of continuum robotics. Fundamental analysis towards this area came from the group of *Walker et al* [8–10]. Active areas of current research by many groups include continued advancement in the application of beam theory to create increasingly sophisticated models of continuum robots, and the constant-curvature approximation. In addition to models, advanced sensors, materials and actuators all contribute to progress in continuum robotics. Current continuum robots are developing towards compact body, accurate sensing mechanisms, and precise control schemes.

In terms of the applications, Anderson and Horn [11] proposed a continuum robot system to manipulate objects in undersea environment in 1970s, where no electronic parts were attached at the soft manipulator so that waterproof issue was avoided. In 1993, Owen [3] developed a car painter through soft continuum robots. The central hollow configuration enabled continuous painting transmission, and the flexible motion collaborated well with workers. Later, in 1999, Morecki further employed the hollow central backbone to conduct liquid transport tasks, which did not need accurate dimension like rigid pipes and the central backbone can be controlled well through actuators, so that the transportation of liquid was greatly automated [12]. Natural disasters pose emergent requirements of rescue and search in confined ruins. The slender and compact soft continuum robots are able to locomote inside these areas carrying with sensors and foods for the stucked people [13]. More industrial applications of continuum robots can be found in the Table 1 of work [14], including waste storage tank remediation, inspection

of unstructured environments and pipes. Another notable application exists in medical surgery. With the valuable application, patients are only operated with a small incision, making them can recover within a shorter time and little pain will cause to them, which is also named as Minimal Invasive Surgery (MIS). In recent decade, lots of useful medical devices like catheters and colonoscopes were developed based on tendon-driven continuum robots, aiming at different specific operations. Surgeons just control the devices via teleoperation, while Magnetic Resonance Imaging (MRT) or color ultrasound vision provides them with true shape configuration of the devices. It is not necessary to conduct big incision. For example, forceps is attached at the tip area and its closure or open can be controlled via a tendon. Combining the flexibility of soft manipulator, laparoscopic surgery can be effectively conducted [15]. Similarly, tools like flexible needles [16], endoscopes [17], arthroscopes [18], colonoscopy [19], and laser manipulators [20] attached on the tip as an end effector enables more useful instruments. Examples of the specifically designed surgical devices also include multi-backbone surgery system, the hyper-redundant cardio arm, and concentric tube robots. Of course, the advantages also pose challenges in implementation. For example, the hyper compliance makes it unable to maintain working state when faced with external payloads. Therefore, more and more researchers have done deep investigation on control schemes. There are also some bottlenecks that restrain the development and application of continuum robots, as summarized in the next section.

1.2 Problem Statement

Currently, although diversified kinds of continuum robots have come into being, it is still unable to put into practice in a large scale. The main bottlenecks include:
1) Developing internal sensors for control and for visualization
Continuum robots are anticipated to work in constrained environment, where users are unable to observe the actual shape. The inherent fabrication imperfections and compliance pose much difficulty for open-loop control because uncertain external

forces deteriorate an control scheme. Using feedback to adapt controller with working environment benefits users manipulating continuum robots as desired. Therefore, sensing the shape and position of end effector becomes a necessary task in practice. Using externally configured sensors like cameras is a direct method, but they are not feasible in some occluded scenarios (holes, caves, and dark area). Being structurally different from rigid robot arms, soft robots are not easy to integrate encoders to sense the shape, such that developing self-sensing mechanisms for this task should be a good alternative. It means that sensor should be embedded into the flexible body, and the deformation of continuum robot leads to signal change in the sensors. In addition, the integration of the sensors should not cause side effect such as resistance in the original deformation towards robot itself. Some existing proprioceptive mechanisms are time-consuming and labour-consuming in fabrication.

2) Constructing control schemes for practical application

Developing kinematic models is key to realize precise control of continuum robots, which relate between the tip configuration/ shape configuration and actuators inputs. In practice, the actual task configuration is expected to move as desired, like given path points and users' setting points, but the complex structure and the uncertain cluttered environments pose much difficulty. On one hand, the models are essentially non-linear, as material properties, structural setup, and working conditions should be considered to build an analytical control scheme. In general, a delicate set controller can only work on one platform because mounting methods, actuation mechanisms and other environmental factors could make a sophisticated model infeasible. More importantly, the uncertainty of external payloads poses difficulty in building the controller, for the action position, direction and magnitude are all unknown for robot system. Besides, to manipulate proper objects, dynamics model should also be considered for the motion precision is highly involved in inertia and acting forces.

3) Reconstructing external forces

In an open-loop control, the task configuration is only related to actuators inputs, but in application external forces are unavoidable. The forces not only make controllers inaccurate, but also make some given path points unattainable. It would be significant advancement if the external forces acting on the soft body can be accurately estimated, which means the barrier in workspace can be indirectly observed. Controller can specifically adjust actuation configuration to adapt environment, such as avoiding hard barriers and overcoming soft barriers. The challenge lies in finding the position, direction and the magnitude of a single force. The external force can present at any position along the soft body, and three components in three directions (x, y, z) of the force should be estimated. This also requires sensors output proper readings and requires models should be properly designed.

4) High motion velocity with accuracy

Conventionally, there is a trade-off between the motion velocity and the accuracy in controlling a soft manipulator. Due to the softness in nature, deforming the soft body at a high velocity could cause significant vibration and inaccuracy in positioning the end-effector. Purely adjusting the controller of the actuators may not be able to achieve satisfactory result in reducing the fluctuation. To address this issue, adding additional degree of freedoms to the soft manipulator through mounting on a mobile platform is a possible solution, which thereby increases the redundancy of the overall system. For example, to reconfigure a single-segment soft manipulator in positioning its end-effector, part of the position discrepancy can be corrected through the linear stage, reducing the degree of deformation and the velocity required by the soft body.

5) Rotation along the deformed backbone

Although the deformation behaviour of continuum robot has been widely explored, making continuum robots work in diversified conditions, it is still expected that they can rotate within the limited space. Ideally, with the deformation, they can rotate around the deformed backbone, such that holes can be drilled without

adding a flexible central shaft to transmit drilling motion.

Apart from structural innovation, algorithms should also be investigated to conduct proper self-rotation mechanism. The rotation should not influence the bending state, and rotation precision should be maintained. This requires two controllers to be synchronized. Similarly, the newly added DoF can also ease the design of kinematics since the rotation of the manipulator could be achieved by the original actuators and the newly added collaboratively.

In summary, both the hardware and software need further investigation to lower down cost and to improve control precision. This research focuses on the four main tasks, researching different internal sensors to realize proprioceptive sensing mechanisms both for shape reconstruction and external force estimation. Controllers can be extended to other similar configurations.

1.3 Outline of This Dissertation

This dissertation aims to provide some feasible solution for the above-mentioned problems in continuum robotics, especially focusing on the control with embedded sensors, real-time shape reconstruction, estimating the external acting on the robot whole body, and developing novel continuum-robot-based tools in actual applications. The rest of this dissertation is organized as follows:

In Chapter 2, I summarized the overall technical innovations in continuum robotics. This chapter starts from the origin of continuum robots and the gradual development of them since the midterm of the last century. The technical innovations in this area was also summarized, including novel actuators, fabrication methods, sensing mechanisms, and control strategies. Most achievement concerning the approaches to deal with the mentioned problems was also included in this chapter.

In Chapter 3, a shape reconstruction method with proprioceptive sensing mechanism using AI model and piecewise curve fitting methods was detailed, with which a novel control strategy also integrating the feedback was built. Consider-

ing that one obvious characteristic of continuum robot is working in narrow and constrained environment so that external configured sensors are not applicable, I developed an embedded sensing system to estimate the true shape of the backbone in a real-time. The estimation also includes the tip position, playing a significant role for the subsequent feedback control. Apart from proposing a controller for the inverse kinematics model, an adaptive step distance mechanism was put up when the robot was performing a point-to-point task. The two modules worked in collaboration while moving, benefiting users to visualize the robot shape and to control the bending motion. They were both built with data-driven method.

In Chapter 4, the method that estimating the external force acting on the robot body rather than the tip area solely was detailed. First, the area where an uncertain external force is likely to present was labelled by a 2D map. The presence of the force was detected by the position deviation in the tip when the robot is acted. This deviation between the load-free and load scenarios in a same actuation input was built via ANN model, which can be applied on other similar platforms. Each of a small area on it was indexed by a column position and a row position. Then, the column position that is involved in the deviation direction was solved by a probability model. All the forces, including internal actuation forces and the external force, will make the robot reach a balance state, such that virtual work principle can be employed to further find the row position and the corresponding magnitude. The whole sensing mechanism was built using eutectic gallium indium (eGaIn) sensors.

In Chapter 5, I designed a novel mechanism to achieve full rotation along the deformed backbone, and novel algorithm to control the whole robot was outlined. This was inspired by some applications where a dexterous manipulator was required to perform manipulation in constrained space and rotation was also simultaneously anticipated, while the two behaviors have not been simultaneously achieved yet. To avoid tube twining issue, a slip ring was employed to decouple the air transmission in the actuation hardware. Another DoF, stepper motor was

mounted at the robot base to rotate the deformable manipulator continuously. This brings two advantages: 1) the shape configuration can be achieved by more combinations of actuation inputs, and 2) continuous rotation along the deformed backbone, is realized. With the novel structure, I designed algorithms to control the movement with fast response and to control the rotation motion.

Finally, chapter 6 concluded this work and detailed the future work.

Chapter 2

Literature Review

A continuum robot system consists of robot body, actuators, sensors, and control models. Technical innovations in recent decades have pushed the rapid development of continuum robotics, making them can be widely applied in diversified scenarios. In this chapter, key components of a continuum system is summarized.

2.1 Soft slender manipulator design

Multiple design with diversified materials and structures formed the robot body. The central backbone is generally the core of some designs, and some soft manipulators have no backbone.

1) Soft concentric tube design

As a special design in continuum robotics, concentric tube robot has been attractive for the high length-to-diameter ratio. It was first proposed by *Webster et al.* [21] in 2006, as Fig. 2.1 shows. Most of them were made of Nitinol alloy and some were developed by polyether block amide using 3D printing [22]. They are organized by hollow pre-curved tubes inserted into each other in series, and the stiffness of them decreases from the proximal segment to the distal one. Rotation and translation between each segment make the entire shape deform and elongate in task space. The actuators are configured behind the manipulator base, so the obvious advantage of them is compactness, such as the 0.8mm-diameter manipulator in [23], which is beneficial for robot surgery. However, the kinematics model of them is also special, and the snapping problem that the robot snaps quickly

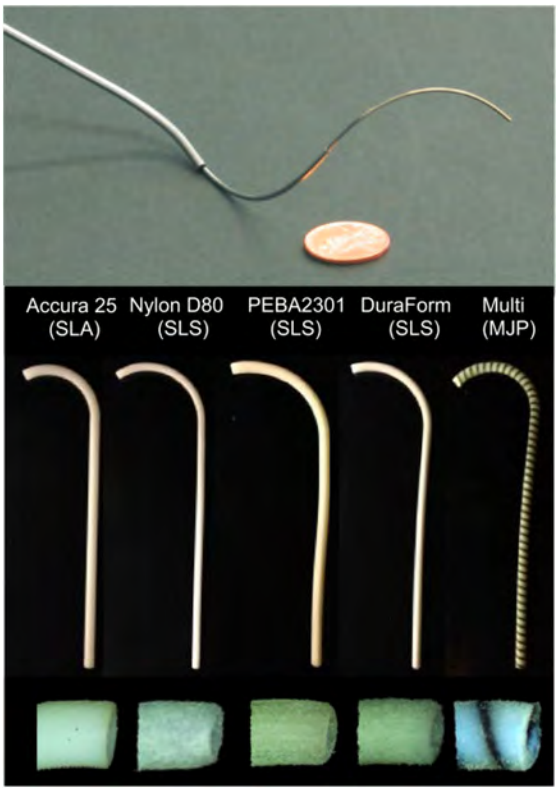

Fig. 2.1. Concentric-tube design.

at the connection part poses challenge to the controller. Additionally, the friction between tubes should be very minimal to ensure smooth extension. Kim et al. [24] proposed a variable-stiffness design to enhance the stiffness of concentric tubes for manipulating heavy payloads.

2) With-backbone design

This design style includes an elastomer configured at the central backbone. The backbone, secondary backbones, and rigid disks are assembled to form the manipulator, and the material of the backbone is commonly NiTi and polypropylene, as Fig. 2.2 shows. The secondary backbone are used for actuation, in which actuators generate tension to deform the manipulator. The length restore depends on the elasticity of the backbone and other secondary backbones. The control model for this design is relatively easier to build since the deformation can be directly quantified through the length variation of the secondary backbones, but the stiffness of them is difficult to regulate.

3) Without-backbone design

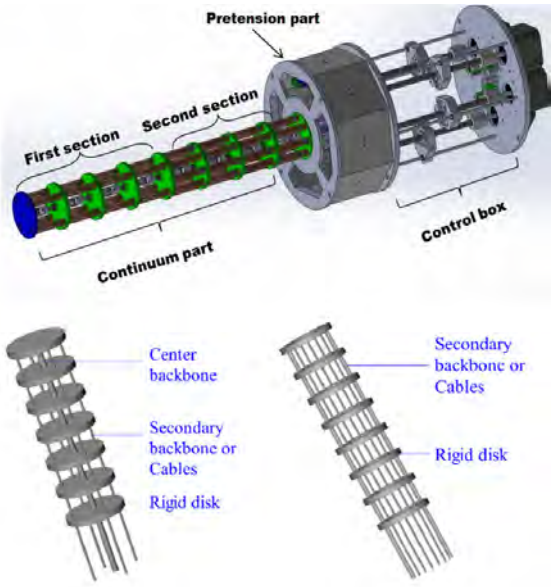

Fig. 2.2. The design with an elastic central backbone.

In contrast to the with-backbone design whose shape is not a smooth arch and the rigid disk may hurt ambient environment, without-backbone design was proposed.

◇ Soft tube design

The whole robot body is an elastomer, as Fig. 2.3 shows. The chambers along the axial direction play a role of guidance, through which the cables can be mounted to tense to bend. With the low stiffness of the material, such as silicone rubber, the manipulator often characterizes high compliance. On the other hand, the low rigidity also leads to buckling upon actuation. To deal with this problem, researchers considered twining thin threads around the robot body to limit the radial expansion [25], and algorithm to avoid over actuation [26].

◇ Notched backbones.

As Fig. 2.4 shows, a flexible manipulator was cut to form notches and deformation towards the notched sides occurs easily [27]. The distance between the notches is very minimal so the deformation is almost an arch after tension.

◇ Spring-based backbone

Low-stiffness springs are compliant and it can be used to build the elastic body. After deformed by actuators, the strain stored in the spring returns the manipulator to the rest state, as Fig. 2.5 shows. Actuators are required to provide higher

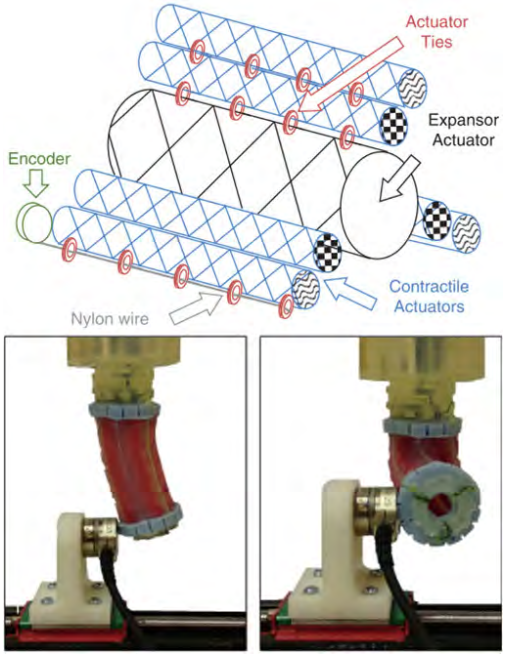

Fig. 2.3. Soft-tube design.

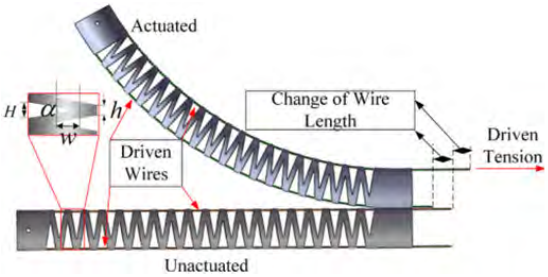

Fig. 2.4. Notched design.

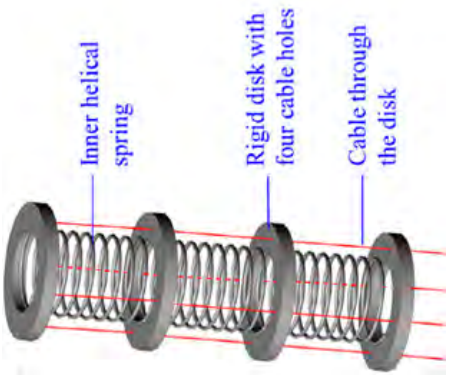

Fig. 2.5. Spring-based backbone.

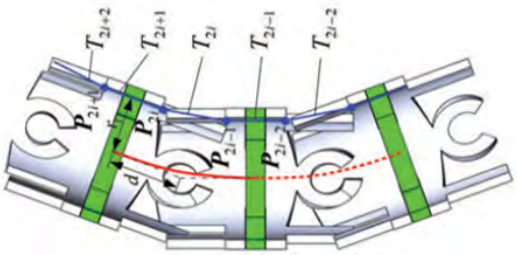

Fig. 2.6. Manipulator with joints rotating around the previous unit.

force if deformation degree is anticipated to increase because larger force is needed to deform a spring.

◇ With joint design

Similar to the with-backbone design, joints with small thickness rotates around the previous joint, as Fig. 2.6 illustrates. In each joint, there are holes to set cables for tension. Most joints are fabricated by polyethylene acrylonitrile butadiene styrene (ABS), and NiTi. In deformation, the relative rotation angle between joints is roughly same, making it easier to design the kinematics model [28]. The stiffness of this design is higher, but it can only deform towards one direction because the rotation can only occur in 2D manner.

◇ Bellow design

For most of the aforementioned designs, they can deform while maintaining the original backbone length. The task space is therefore, limited within a small area. Fig. 2.7 shows this design. Inside the manipulator, chambers are set radially for deformation, which are actuated by fluids. The gap distance between the bellows can be adjusted by the actuation inputs, enabling backbone-elongation design [29].

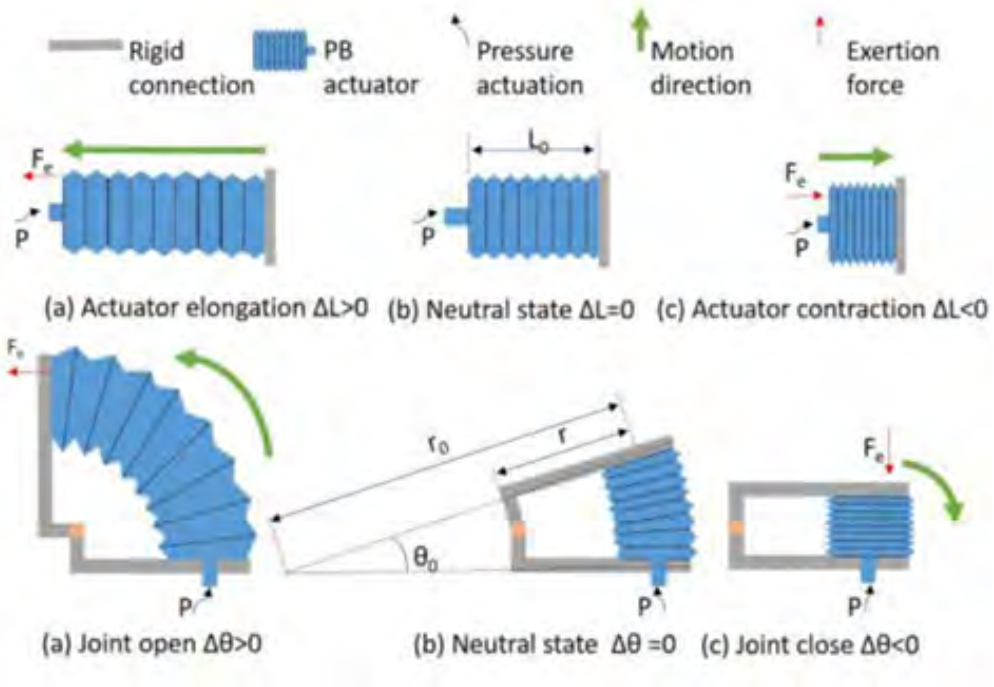

Fig. 2.7. Bellow design.

It is light weight and is with a smooth shape. The stiffness is also marginal because of the soft material.

◇ Origami design

Foldable mirror and bombs inspired origami-styled soft robots [30], as Fig. 2.8 shows. They are made of photopolymer resin or similar flexible material, and actuated by cables. Being actuated, it can perform 2D or 3D deformation, and the connection part between each piece can be regarded as a revolute DoF. Also,

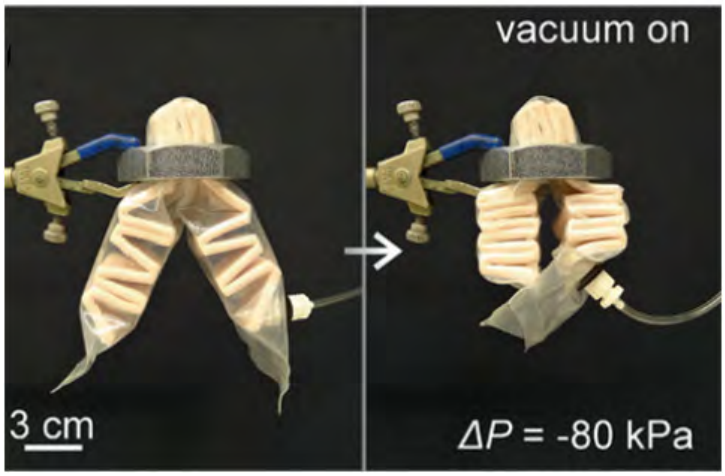

Fig. 2.8. Origami style.

the soft structure is beneficial for contact with ambient environment.

2.2 Stiffness Adjustable Manipulator

In load-free condition, soft continuum robots are anticipated to locomote faster with little energy, which means the stiffness is desired to be smaller. On the contrary, while in manipulating objects and in meeting external disturbances, they should characterize higher stiffness to minimize the effect from external forces. Therefore, the robot manipulator would be better if it can adjust the stiffness to adapt specific tasks. Researchers investigated particle jamming, special alloys, and antagonistically-driven approaches and designed mechanisms to change the stiffness quickly.

2.2.1 Particle Jamming

Actually, the robot can be designed with multiple hollow areas to fill other rigid materials. The density of the material is involved in the stiffness. Fig. 2.9 shows the basic working principle [31]. It includes layer jamming and granular jamming. The stiffness is determined by the friction between the soft layer and the particles. To regulate the friction, namely the interaction among the particles, air pressure is considered, where higher pressure (negative pressure) promotes larger friction. To avoid buckling, negative pressure is generally used. In terms of the particles, rigid granules, layer jamming, layer jamming with supporting internal structure, and hybrid mode were employed [32].

2.2.2 Special Alloy

Special alloy like shape memory alloy (SMA) exhibits phase transition in temperature variation, which can be controlled by electrical current. The SMA-made spring functions 'lock' and 'unlock' to adjust the stiffness. Additionally, low-melting alloy, such as eGaIn whose melting temperature relies on the component ratio of the alloy, increases the overall stiffness of the manipulator when the temperature is lower than the melting point. *Peters et al.* embedded this alloy into

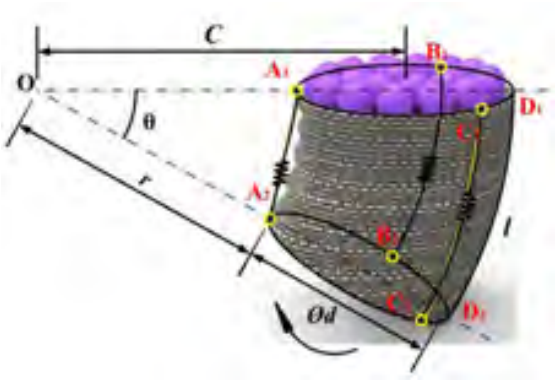

Fig. 2.9. The robot body is designed with hollow part where granular particles can be filled.

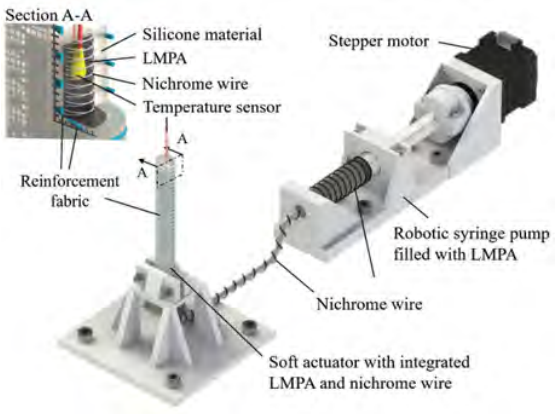

Fig. 2.10. Low-melting alloy for actuation and stiffness regulation.

a silicone manipulator [33] for actuation and stiffness controlling, where the tube for the alloy transmission was coated with Nichrome wire for heating, as Fig. 2.10 illustrates. This benefits actuation and stiffness variation, but cooling and heating require long time. The alloy is not cost-friendly, and the fabrication process is complicated.

2.2.3 Delicate Design for Stiffness Control

Stiffness is manifested by EI (E is Young's Elasticity modulus and I is the inertia), so through controlling I the stiffness can also be changed, which is relatively simple and requires little response time. Fig. 2.11 shows two typical designs to control the stiffness. In [24], relative rotation between segments was employed to change the inertia of a concentric tube robot. In each tube surface, a array of notches was engraved by laser cutting, and the length of the notch is only 0.5mm, benefiting

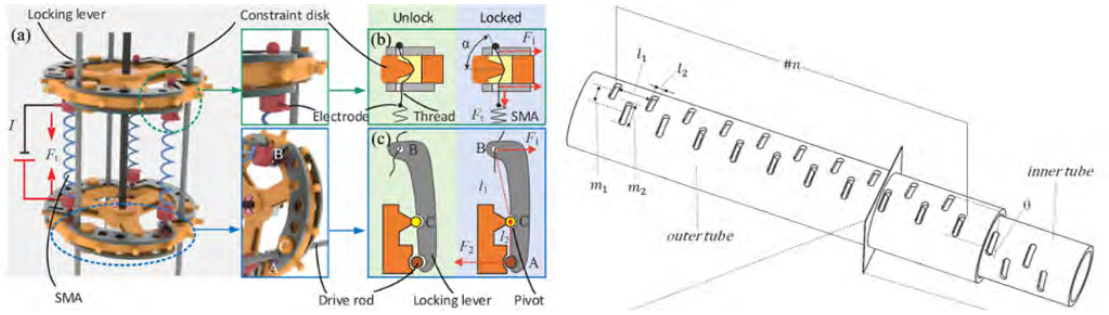

Fig. 2.11. Structural design for stiffness controlling.

small-sized soft manipulator design in MIS. In [34], authors considered a 'Locking lever' mechanism to constrain the cable length and actuation forces (Fig. 2.11-left). The locker was individually controlled by SMA actuators. With the short locomotion distance, the response is faster.

2.3 Actuators

Omni deformation in task space is the fundamental function that a continuum robot system should exhibit, and the deformation enables the end effector mounted at the tip area to complete diversified tasks, which is the balance between actuation forces and the elastic forces in load-free condition. There are generally three chambers distributed radially along the manipulator for actuation, where the difference in the force leads to deformation degree and orientation. The working principle of the actuation inputs varies, but all the actuators act by varying the length of the chambers. The bending of the whole manipulator is reflected by length difference in the chambers. It is the unsymmetrical force on the manipulator's chambers that contributes to moment and further generates various shape. In order to elongate or shorten chambers, diversified actuator mechanisms have been developed.

2.3.1 Tendon-Driven Methods

Tendon-sheath mechanism is a common method [35–39]. The length variation of the chambers is realized by pulling the tendons mounted inside the chambers. Through pulling the tendon, the length is decreased and elastic property of the

robot returns the chamber to the rest length. Generally, a rigid ring is attached at the top side of a manipulator and three tendons are respectively connected to the rings with 120° radially apart. The length variation is precisely regulated to ensure one actuation input maps to one shape/tip configuration, so the tendon is inextensible and thin, like NiTi coil. At the other side of the tendon, actuators are needed to provide tension. Stepper motors and servo motor [36, 37, 40] were employed to pull or release the tendon. Tendons are connected to the motor shaft through pulleys so that the rotation of motor will pull the tendons to change the chamber length. The rotation velocity and displacement of the motors can be accurately regulated by pulse cycle and counts. To decrease the friction between the tendon and the chamber surface, the cables are housed inside sheath with lubricative oil. Miniature of tendons benefits fabricating compact continuum robots that are flexible in Minimal Invasive Surgeries (MIS) [41–43] and other constrained environments. However, it needs relatively complicated configuration to transmit motion when a continuum robot has multiple segments, making cumbersome mechanical structures behind the soft manipulator, and the thin cable is twined at motor shaft so that the rotation of shaft can not be directly used to calculate chamber length. Besides, tendon can not generate tension for the chamber, and the stiffness is somehow reduced because of the tensioned coil.

Apart from motors, Shape Memory Alloy (SMA) provides another alternative [44–48] for actuation, as shown in Fig. 2.12. SMA is a material that undergoes phase transition when exposed in temperature gradients. Namely, when being heated, phase transition from martensite to austenite presents, which contracts the material and leads to deformation. The temperature of the material maps to the deformation degree of SMA. Because of the metal property that it has electronic resistance essentially, electrifying SMA generates Joul heat and deformation appears. Thus, a tendon connected to SMA coil can contract the chamber and it can be used as soft actuators. As for this configuration, the actuators can be small and simple in comparison to motor-driven tendons, and transmission of the

tension could be easier, since only two electric wires are needed for each chamber. Controlling the voltage of current of the circuit can regulate the power of the actuator. However, in terms of the effectiveness, the heating and cooling both require relatively longer time and thus robot cannot response rapidly as compared to motor-driven setup. Researchers added cooling system [49] (water cooling and fan) to accelerate the temperature variation process.

For the both actuators, returning from shorten state to the rest state of chambers just depends on elastic energy stored during manipulation, which is not robust enough and hysteresis of material leads to uncertainty for further control. Then pre-tensioned tendons somehow stiffen the manipulator, so controlling the length and the tension enable controlling shape configuration and stiffness regulation.

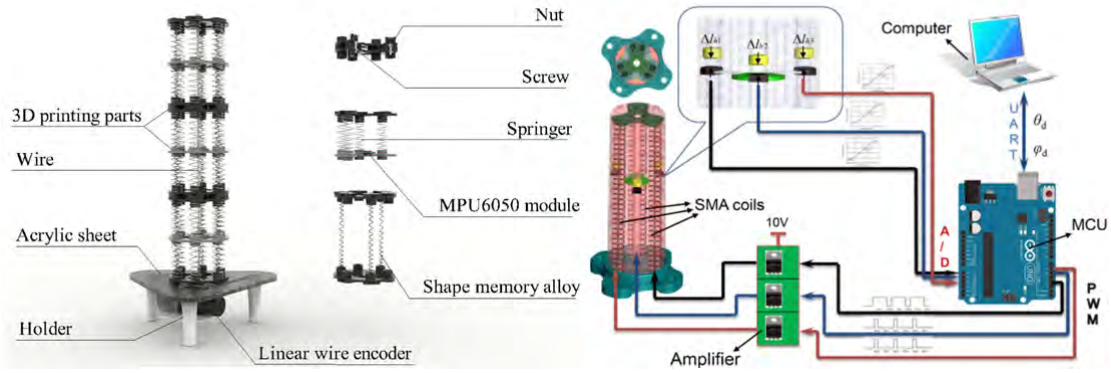

Fig. 2.12. SMA-driven continuum robots.

2.3.2 Fluid-Driven Actuators

In contrast with tendon-driven mechanisms, elongation in length is achieved in the chambers by fluid-driven actuators [30, 50], which also can generate length difference in the chambers. Each chamber is connected to a tube to transmit fluid. This does not need specific design on energy transmission parts, and the pressure of the fluids (air or water) quantifies the actuation inputs. Without complicated energy transmission components, the effectiveness is relatively higher and the response time is shorter than that of SMAs.

Pneumatic-driven continuum robot systems are also notable [51–55]. The tech-

nical development in pneumatic transmission is sophisticated in recent years, and the precision in terms of the pressure and flowrate can be very high via advanced valves and accessories. The pressurized air directly acts at the chambers, elongating the chambers and deforming the manipulator. While shortening, the pressurized can be released to ambient environment. The tubes for transmission can be flexibly configured, which eliminates significant cost in preparing mechanical structure. Fig. 2.13 shows three pneumatic-driven continuum robots. Basically, the length of backbone is limited to maintain elastic property. Besides, expansion of pressurized chambers consists of radial and longitudinal directions, but only axial expansion is desired so that radial expansion should be constrained during fabrication [30,56,57]. At the power source side, pump, gas regulators and pressure sensors are indispensable because the precision of pneumatic pressure is highly involved in precision of controller. Since the pressurized fluid acts at omni direction of the chamber, constraints should be added at the circumferential direction and to promote length in axial direction, such as twining thin Nylon thread spirally along the outer surface of the manipulator. Other fluids, like water and oils can also be employed, and the effectiveness will be higher for they are regarded as incompressible, but they should not be ejected into air when decreasing pressure. At this end, fluid-driven mechanisms also require delicate design.

In addition, some fluids present stiffness under lower temperatures, which achieves deformation controlling and stiffness controlling simultaneously [58]. This is desirable when manipulating objects, where lower temperature could be set to enhance the stiffness of the soft arm, and higher temperature is prepared in load-free motion. Consequently, the collaboration between multiple 2D-deformation elastomers can be integrated into an artificial hand.

2.3.3 Dielectric Elastomer Actuators

The need of developing actuators with high flexibility, compliance and compactness is still a hot research orientation. Dielectric elastomers (DE) provides a solution.

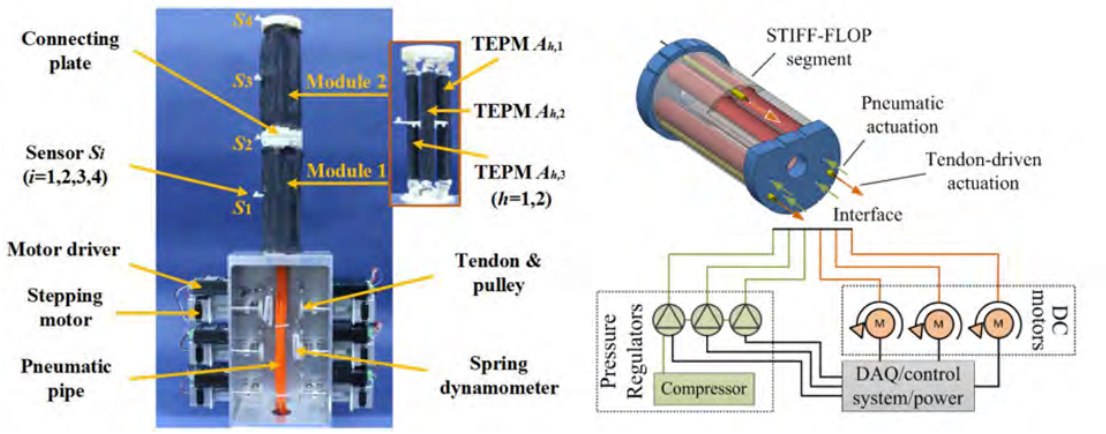

Fig. 2.13. Snapshots of pneumatic-driven continuum robots

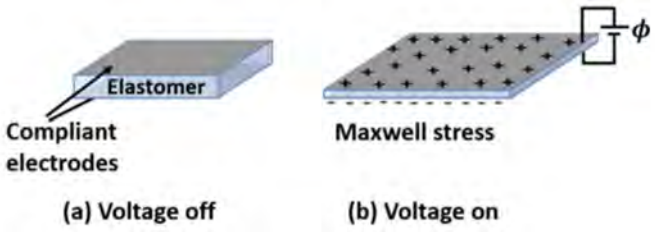

Fig. 2.14. Illustration of DEA's working principle.

Voltage applied the thickness ends of a soft material could generate large strain, as a result of Maxwell stress between charges on the two electrodes [59–61]. Fig. 2.14 shows the fundamental working principle of DEAs. It features high elongation rate (>100%), high energy density (0.4 J/g) and high energy efficiency (>80%) [62]. A large number of works have shown that soft actuators based on DE are extraordinarily attractive because they exhibit big energy density and muscle-like response. Another advantage of this actuator is that the shape variation of the elastomer can also lead to capacitance variation, so that it can provide sensor readings without need of other sensors in application [61], which is also named as self-sensing mechanism. Some relevant examples of DEA include manipulators [63], prostheses [64], and stiffness-tunable muscles [65]. Fig. 2.15 shows several DEA-based soft robots. This actuation method is structurally different from others. Dielectric field directly acts at thin membrane which is also an unique motion part in the robots. On the basis of this, notably rolled configuration like spring-roll actuators exhibits large strains and forces, where pre-strain process is simplified. It also

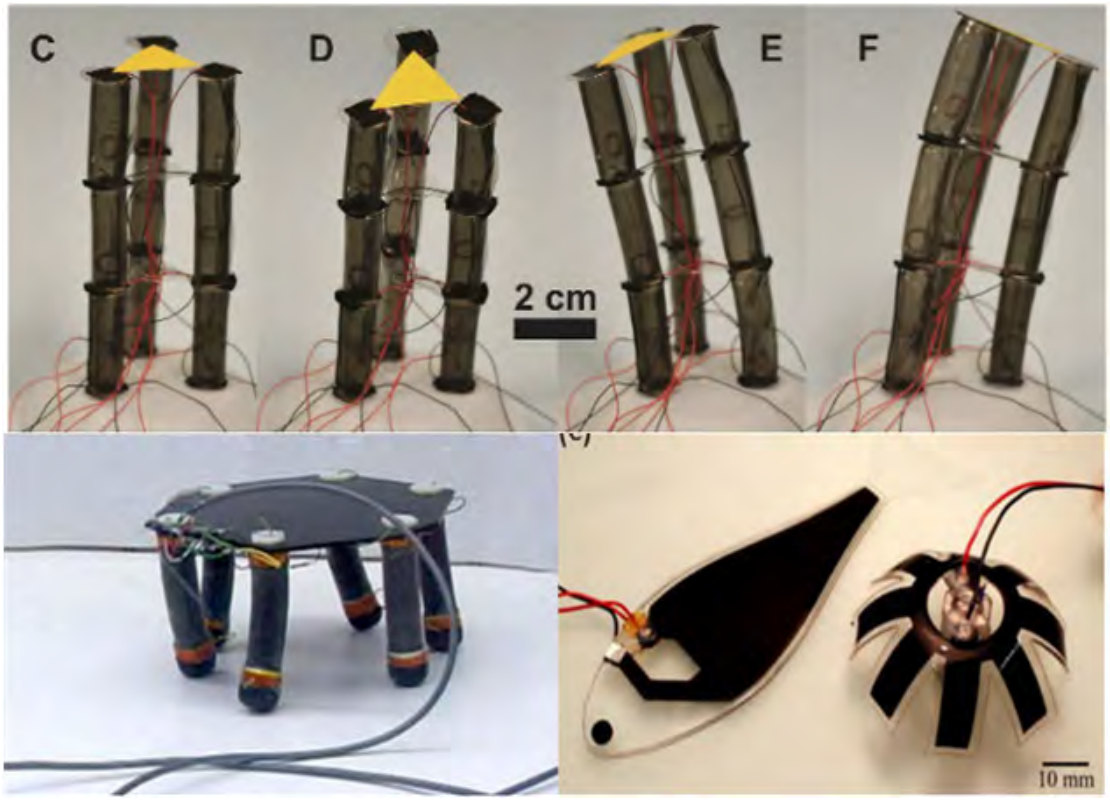

Fig. 2.15. DEA-driven soft robots.

does not need complicated power transmission parts and the effectiveness is high. On the other hand, it needs high voltage to drive the thin membrane, which is up to 6KV [66]. Thus, some modules involved in transferring low direct voltage into high-frequency AC should be employed. Additionally, when the actuators are required to interact with dynamic environment, the position and the actuation force are both anticipated to be controlled.

2.3.4 Magnetic Actuation

The configuration of magnet inside a continuum robot can also miniaturize the entire manipulator, because the magnetic field is generally added externally. This non-touching actuation mechanism does not require complicated mechanical structures, and enhances dexterity of the robot [67]. External magnetic fields can deflect the tip and deform the robot by attracting or pushing the magnet mounted at the tip [68]. In addition, during fabrication, magnetic powder can also be evenly incorporated into the liquid silicone, which generates uniform force at the robot body

and brings flexibility in control. Interestingly, the distance between two adjacent magnets can act as sensors to detect the tip configuration. The challenge lies in fabricating a soft elastomer with desired amount of magnetic powder, so this work [69] considered 3D printing technology——magnetic field-assisted projection stereolithography process. At the anterior and posterior legs, two magnets are attached playing a role of worm's legs. Also, [69] proposed a soft microrobot steering a guidewire within a 3D phantom vascular network. By applying external magnetic field, this microrobot can locomote inside very tiny space, and the change of the magnetic field guides the locomotion direction and velocity. Researchers in recent years investigated the dexterity of magnetic-driven continuum robot without hinder the miniaturization. Although it provides an untethered solution for soft robotics, they are not able to work within a big space range and ferromagnetic environment will significantly influence actuation effectiveness. The setup of accurate external magnetic field is expensive and time-consuming.

2.4 Sensors for Continuum Robots

The shape and the tip position of a rigid robot arm can be directly obtained through the encoder mounted at the motor or other external vision systems. However, it is impossible to consider encoders for continuum robots due to the distinct working principle, so investigating proper sensors is indispensable in this field. Real-time and accurate sensing the key points and the whole shape of a continuum robot are fundamental to achieve visualization and to achieve feedback control. Therefore, sensors are necessary, which can be categorized into external sensors and internal sensors, based on the mounting location.

2.4.1 External sensors

External sensors are mounted outside of continuum robot, such that the shape and any interested key point can be easily and directly observed. Optical cameras [70]

are commonly employed to sense the markers attached at the robot body. Fusing digital image process technologies eliminates background noise and the position of ROI w.r.t the universal frame is obtained via calibration system. Therefore, the precision of results depends on the precision of camera matrix and position of markers. Besides, near-infrared camera [71, 72], RGB-D camera [73], structural light vision, and optical trackers [74] are also applied to sense tip position and shape of manipulator. As for cameras, they set some basic requirements such as dark environments are not allowed and more importantly scope between object and camera cannot be occluded, making they are not applicable in some constrained environments. This promotes the requirement of investigating internal sensors to build proprioceptive mechanisms.

2.4.2 Internal sensors

To mitigate the disadvantages of external sensors, internal sensors gradually play important roles. They are embedded inside manipulator and work with the shape change of the chambers. There are generally three aspects should be considered: 1) sensors should be easy to integrate into robot, 2) sensors should leave little negative influence on deformation, 3) precise and unique sensor signals should be output during operation, namely one deformation status maps to one set of sensor readings.

Scharff *et al.* [75] proposed a novel color-based 2-D shape measurement method, where the deformation of the soft manipulator leads to the change in color and the change was detected by color sensors. Nevertheless, payloads were not considered, for which may distort the bellows such that the color sensors could not percept the detecting area. Similarly, deformation of elastomer can lead to length change in the chamber filled with liquid metal, like EGaIn, resulting the change of electronic resistance [76]. EGaIn-based sensors are widely embedded into soft robotics [77, 78]. The volume of EGaIn metal is constant, and the elongation in axial direction leads to sectional area decrease. This increases electronic resistance,

and the signal can be transferred into voltage for measurement. A novel soft sensor made by embedding conductive silicon into nonconductive silicone was proposed by Thomas *et al.* [79]. They succeeded sensing the shape and estimating external force applied on the robot's tip. Venka-tasubramanian *et al.* [80] discretized a flexible robot as multiple serially connected pseudo rigid links, but solving the unknown angle of each joint to obtain the shape is computationally burdensome. Measuring the length of the actuated chamber with linear Hall sensors is also feasible [81]. However, this shape-sensing method is based on piecewise constant curvature (PCC) model that is not necessarily exact when robot interacts with payloads. Electromagnetic (EM) sensors are another way to measure the relative pose (distance) between a reference point (sensor) and the deformable body (magnet) [39, 82–85]. It works with an externally configured magnetic field and the area of task space is limited. Similar to Hall sensor, its performance could be interfered by strong magnetic fields, which also features high cost in application. Non-toxic liquid metal provides another alternative. Different degrees of deformation can lead to strain change on a local area of robot, which inspired the use of strain/stress related sensors. For instance, Fiber Bragg Gratings (FBG) [80,86–88] can sense the change in the curvature of an optical fiber by detecting the shift in the wavelength travelling in the fiber. The fiber can be very small in diameter and is immune to noise. FBG-related models generally regard the strain change of FBG as linearly elastic. As a result, it has marginal ability to elongate, limiting the deformation degree of soft robot. Besides, optical fibers need to be manually inserted after fabrication of the soft body, increasing the overall manufacturing cost.

2.5 Development of Controllers

Controller design is a core in this research field, for which maps between the desired tip/shape configuration and the actuation inputs. No matter in any condition, the end effector mounted at the robot tip should be controlled accurately for achieving

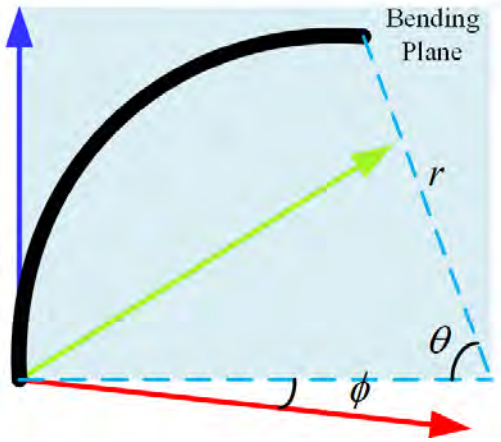

Fig. 2.16. Illustration of PCC model, where the backbone is assumed as an arch.

tasks, requiring accurate models between actuation inputs and configuration of end effectors. Also, the controller in load-free condition can be modelled using PCC assumption, since the position of end effector is just related to actuation inputs. Fig. 2.16 shows the shape of backbone with the PCC assumption [14]. The shape of the backbone is assumed as an arch with curvature $\kappa = 1/r$, bending angle θ and direction angle ϕ. Therefore, the position of the tip is determined by the shape configurations. The kinematics models (including forward and inverse kinematics models) can be built using the three parameters. First, the mapping of the tip position $P(x, y, z)$ and the three parameters is:

$$\phi = \text{atan2}(y, x), \theta = 2\text{acos}(\frac{z}{\sqrt{x^2 + y^2 + z^2}}), r = l/\theta. \tag{2.1}$$

Second, the length of each chamber is also related to the three parameters:

$$l_1 = l(1 - \kappa)r\cos(\phi), l_2 = l(1 - \kappa)r\cos(\phi + \tfrac{2}{3}\pi), l_3 = l(1 - \kappa)r\cos(\phi + \tfrac{4}{3}\pi) \ . \tag{2.2}$$

where r denotes the configuration radius of the chambers. In this way, the mapping both for inverse kinematics and forward kinematics models can be built via the shape configuration. However, for tendon-driven robots, this is feasible, but for others like pneumatic actuators, the actuation inputs are implicitly related to the chamber length, so that this model is not accurate. It is then necessary to find another mapping between the length and the pressure. In addition, as the shape can sometimes be assumed as an arch, (2.2) is not right because the

shape configuration, especially when the direction angle is not solely determined by actuators but also influenced by external forces. With the knowledge of robot arms, the kinematics could be built using D-H model, where the deformed arch is virtually connected by multiple rigid bars. The connection part is assumed as a joint that controls the relative angle between two bars. In theory, more bars contribute to more accurate kinematics but the computation of the inverse kinematic model is complex [89].

More importantly, to control a soft continuum manipulator accurately under disturbance, versatile methods have been investigated. The uncertainties of material and external forces are essentially unavoidable, so fuzzy control theory with Neural Networks [90] and with Jacobian-based method [91] are feasible. Jacobian matrix maps between the velocity of end effector and change of actuation inputs. Therefore, in a short interval, the velocity can be revised as displacement, but it is not always with full rank. To overcome the limitation of Jacobian matrix that singular position occurs for robots with infinite DoFs, Giorelli *et al.* [92] fused Jacobian and Neural Networks, and solved the inverse kinematics of a cable-driven robot. Singular value decomposition (SVD) method is often employed to address the inverse of Jacobian matrix. Yip *et al.* [93] proposed an convex optimization algorithm to form feedback control in constrained environments. Online estimation was investigated by Fang in [94], where kinematics can be assumed as a local Gaussian model and updated continuously. Notably, some continuum robots [95–97] can adjust the stiffness of robot to alleviate the influence of external payloads. Reinforcement learning provides a novel solution [98] to this challenge, where soft robot is commanded to learn the optimal control model, requiring little human intervention. It, however, needs longer time to train the model. Li *et al.* [99] assumed the Jacobian matrix is constant within a local area, and estimated it by moving actuators with small increments and sensing the change of the end effector, which is time-consuming. Similarly, a novel Strong Tracking Kalman Filter (STKF), was proposed by Li *et al.* [100] to work adaptively, in which a fading

factor was introduced to accelerate the convergence and the covariance matrix was updated by an innovation sequence. Apart from them, model-based methods also contribute to the controller of continuum robot. Cosserat rod theory [101], virtual work [34], improved PCC algorithm [102] and stiffness of material [103,104] are employed to find the mapping between forces (actuation inputs and external forces) and the pose of robot's end effector, which is an inverse process in control. One segment of continuum robot can also be virtually modelled as multiple rigid revolve joints connected serially, and the configuration of each joint determines the task configuration, which can be modelled using Denavit-Hartenberg parameters [27, 105, 106]. In theory, more virtual revolve joints contribute to higher accuracy, but it also sets higher computation requests.

Besides, dynamics models are also pursued during application since the acting force of end effector is also an important object. Rucker *et. al* [107] proposed statics and dynamics models with Cosserat rod theory on a tendon-driven continuum robot platform. Mustaza *et. al* [108] proposed a dynamics model with Lagrangian algorithm, which considered Euler-Lagrange equation and energy formulation. Reinforcement learning [109] provides another solution for this problem. However, the dynamic control in soft robotics is still an open problem to be explored and analysed.

2.6 Shape Reconstruction Approaches

For users or handlers, the shape of the continuum robot is desired to be visualized during operation and they could perform better manipulation based on the actual shape feedback. To further visualize the robot in motion, converting sensor readings into shape information is also an important step to achieve, which is generally the subsequent work of internal sensor setup. Analysing above sensors, some can directly find the position of key points while others just show a variation trend. Sensors generally are not able to measure the 3D information or even the length of backbone, so the raw sensor readings should be modelled in response to the

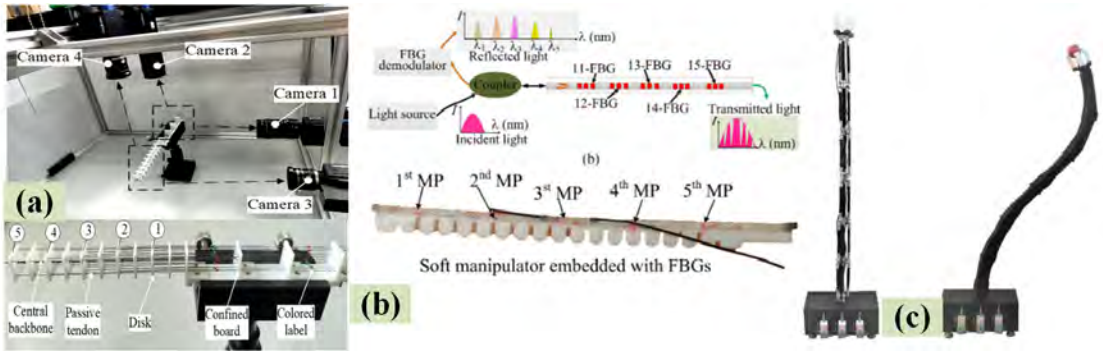

Fig. 2.17. Some shape sensing experimental settings.

true shape state. In load-free condition, the shape of manipulator is traditionally treated as an arch, namely PCC assumption, and the length of each chamber can be directly obtained from actuators like motor encoders, pneumatic pressure and temperature of SMA. However, this assumption is not accurate enough when the robot is experiencing external payloads.

Like the linear elastic approximation applied on FBG sensors, it is equally important to build mathematical models to relate between the sensor readings and the manipulator shape (Fig. 2.17 (a) and (b)). Song *et al.* [110, 111] fitted backbone using piecewise quadratic Bezier curve and the position of key points were obtained by EM sensors. Constraints were set at the connection points between adjacent Beizer curves, which strictly require the two curves should be tangent with each other. For large-scale continuum robots, inertial sensors are competitive (Fig. 2.17 (c)), which can be mounted at the end of each segments to sense the relative posture variation [112]. Inderjeet *et al.* [113] adopted Hodograph curve to fit 3-D backbone, where the original curve function is essentially too complicated to achieve real-time calculation. Other related methods include: cubic spline [114], microarc interpolation [115, 116], and cubic Bezier curve [117]. However, most existing curve fitting algorithms only focused on 2-D curves, which did not consider the spatial shape of robot when it's influenced by external force, so the fundamental curve function should be at least a 3D curve. As for all curve fitting algorithms, the accuracy of given points is highly involved the final fitted curve, so that the fitting method should be tolerate with this error in some extent. In

addition, Scimeca *et al.* [118] fabricated a capacitive tactile array that is mounted at the bottom of continuum robot. By sensing the force change of the sensors and using Neural Networks, they solved the shape in 2D manner. This is a simple solution, but 'one to many' issue exists due to indirect measurement. Regard continuum robot as a cantilever beam, and the 3D shape can be modelled by material properties and all forces acting on it. Beam theory [95, 119–121] regards a flexible manipulator as a cantilever beam, and the spatial displacement of a manipulator is solved using internal payloads (from actuators) and external forces. This is theoretically feasible but quantifying every external force is indeed not practical. The acting point of external forces and the corresponding magnitude are both uneasy to solve during computation.

2.7 External Force Localization Solutions

As external forces pose significant challenge in designing control schemes, estimating them will be useful in practical control. Intuitively, robot could bypass the uncross-able barriers and specifically control actuators to overcome smaller or fragile obstacles. Since the end effectors are generally mounted at the tip, external forces acting at the tip areas are often the focus in estimation. A multi-DoF force gauge can be mounted at the tip area [122], to estimate the force and wrench. Additionally, Thuruthel *et al.* [79] considered embedded sensors and deep learning to estimate the load at the tip (Fig. 2.18 (a)). Venkiteswaran etal. [80] virtually discretized a small-diameter catheter with pseudo rigid body and estimated the load along the manipulator using electronic coils (Fig. 2.18 (b)). Ashwin *et al.* [123] proposed an optimization-based method estimate an obstacle present in task space, which the motion is only two-dimensional (Fig. 2.18 (c)). Qiao *et al.* [124] localized and estimated the magnitude of external force acting on flexible instruments (Fig. 2.18 (d)), and the real-time shape was simultaneously solved. The flexible body was modelled using Cosserat rod theory. The magnitude and the positions were assumed as states to be estimated in each control instances,

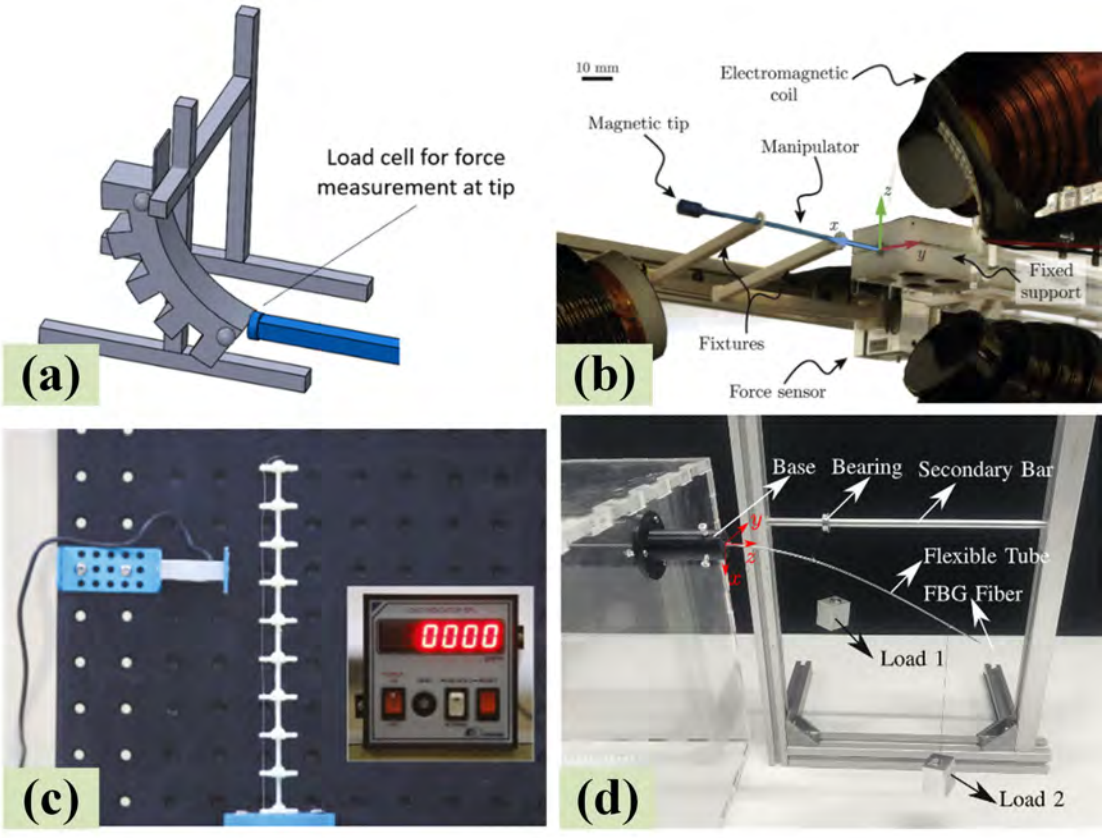

Fig. 2.18. Several existing external force estimation experimental setups.

which were then solved using Extended Kalman Filter (EKF).

With the information of real-time external forces, the complexity in designing controllers will be reduced since some excitations (disturbances) to the beam are known. However, most existing works only focused on small interested areas and assumed a single acting force, while the external forces are uncertain. In terms of hardware, embedded flexible sensors are still more attractive and applicable since continuum robots are anticipated to work in confined scenarios, so force estimation is built on the basis of internal sensors. In applications, when the diameter increases, the areas where external forces may present increase significantly, which differs from thinner designs. Accordingly, the complexity of finding the areas increases a lot.

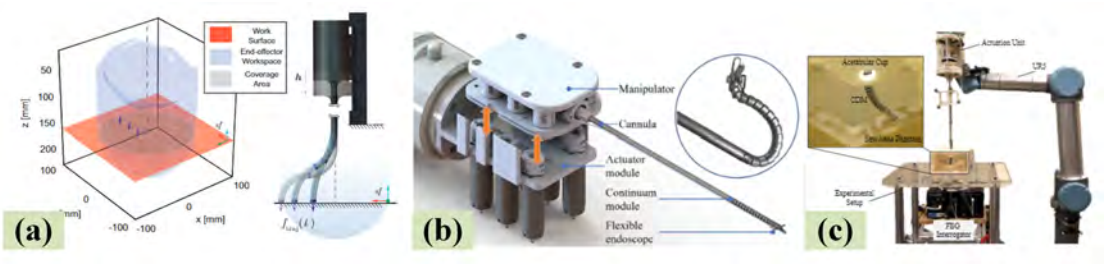

Fig. 2.19. Continuum robot designs mounted on mobile platforms. (a) On linear stage. (b) On a revolve motor. (c) On a six-DoF rigid robot.

2.8 Multiple Motions with More DoFs

Essentially, it is difficult to integrate a three-segment continuum robot pursuing small diameters, for each segment needs three chambers for actuation. Common continuum robots have only one or two segments and the length is generally constant. Each segment deforms in task space and the tip's movement is with the change of position and orientation. For two-segment designs, the orientation and position could not be decoupled, while in some scenarios simple translation or rotation is indispensable, which requires more DoFs. Adding the soft manipulator at a linear platform is a common alternative. It generates translation motion to the tip and the orientation variation depends on the soft robot itself [125], as shown in Fig. 2.19 (a). In this configuration, the tip can conduct planar movement keeping vertical to the horizontal plane. Similarly, Fei et al. [126] considered a 3-D gantry robot to translate a soft gripper. It expands the task space. To simplify the actuators, a revolve joint was designed at the flexible manipulator's base [127], so that the proximal segment only needs to deform to generate bending angle while the direction angle is varied by the revolve joint (Fig. 2.19 (b)). In MIS, flexible manipulator is mounted on a thin catheter which is pushed/pulled by a surgeon. A rigid robot arm could conduct this work automatically [127], enabling diversified pose of the soft robot (Fig. 2.19 (c)). More importantly, the imported DoFs not only promote new motions, but contribute to higher redundancy. However, the integration may also cause complexity in actuating the soft manipulators. For example, the revolve joint is unable to rotate constantly since the tendons for

actuation will be twined around the motors shaft. For the UR5 robot, the entire actuators that were bulky were attached at its end effector, which did not promote to enhance task space because the mobile bulky actuators are not applicable in constrained spaces. In designing controllers, the precision of the new actuators is regarded as much higher than that of the soft manipulators. Also, they bring difficulty for controllers, as a desired tip configuration maps to multiple actuators inputs for the hyper redundant settings.

Chapter 3

Shape Reconstruction and Control under Uncertain External Disturbance

3.1 Motivation

Continuum robots have been attractive for use in surgery, inspection/repair, and self-exploring applications. No matter for any operation, flexible continuum robots need to be controlled accurately. In addition, the shape of the flexible manipulator is anticipated to be visualized so that surgeons can perform better handling. In load-free condition, the visualization and the control can be roughly achieved by PCC model. However, manoeuvring and visualizing flexible manipulators in unstructured environments with high precision is challenging, as uncertain external payloads are unavoidable.

First, the visualization issue is to find the position of points located on the backbone of manipulator. The visualization problem can also be regarded as a shape reconstruction (SR) issue. This is also equal to finding the position of key points on the backbone, where more accurate position and more key points contribute to better SR results, and computation complexity should also be considered to ensure obtaining the result in a real time. It means that external sensors (like cameras) are not practical in constrained environments, so that developing proprioceptive shape sensing is indispensable. Sensors and algorithm to translate the sensor readings into shape information are two important modules for

this issue. Current internal sensors include: FBG, EM, color-based deformation measurement, and Hall effect-based. They need complicated fabrication process and are not robust in some environments. Therefore, I tried to explore an easier fabrication method to embed internal sensors with high robustness. The mapping between sensor readings and shape position was built using a simple approach, so as to apply this method to other categories of continuum robots. This also requires SR model to work in both load-free and load scenarios. As such, the estimated shape can not only act as a feedback for users but an important position feedback for the controllers, since compensation the effect of load is a core part.

Second, manoeuvring a continuum robot accurately requires robust and proper kinematics models both in the two scenarios. Due to the uncertainty of EF, conventional analytical models are not practicable in non-free conditions, because system can not find the precise acting position and the magnitude of all external forces. Any of them can invalidate an analytical controller. For example, the direction angle of the PCC model deviates from the theoretical value due to an lateral external force; Jacobian matrix reaches a singular value position with the force, and then the controller fails to set proper actuation inputs for the task; Statics models need the information of all acting forces, but external forces' position and magnitudes are unknown. In path-following tasks, robot is likely to face kinds of disturbance, which is required to pass through consecutive points. Therefore, controller in the tasks should characterize load-compensation ability to flexibly adjust the actuators to approximate the destination. The hyper redundancy and high compliance of continuum robots pose difficulty in building a desirable controller. To control it well, integrating the real-time pose error is a feasible alternative and models could compensate the deviation. Ideally, the results of real-time shape reconstruction can act as pose feedback for the controller, inspiring to develop a self-feedback mechanism for continuum robot. A simple sensor system was embedded into a dual-segment soft manipulator to deform together with the robot itself, while little reduce was generated.

3.2 System Description

Before proposing the methodology, an experimental testbed was fabricated at first for further validation. As analysed above, pneumatic actuators were finally selected as the actuation mechanism because gas can be exhausted into atmosphere directly when setting a lower pressure and air transmission does not need complicated parts. The material of the robot body is silicone, which is highly soft, and it consists of two segments so that the end-effector can form different pose through different actuator inputs.

3.2.1 Fabrication of Soft Manipulator

Fig. 3.1 (a) shows the fabrication process for a segment of the soft manipulator. First, silicone rubber (E605, Hongyejie, Shenzhen, China) was poured into a 3D-printed mold (Fig. 3.1 (a)-(I)) and cured in an oven (60^oC). Then, two rings (PLA material) with a diameter of $35mm$ were placed at the two ends respectively, and an inextensible Nylon thread was attached at the center of the rings to limit the total length of one segment as $150mm$ long (Fig. 3.1 (a)-(II)). Three channels (chambers) with a length of $130mm$ were created along the body to enable inflation and they are distributed at 120° apart (Fig. 3.1 (a)-(IV)). To constrain the body to expand radially, Nylon thread was spirally wrapped around the manipulator. Then the chambers can only be elongated by the pressurized air and the effectiveness of the actuators is enhanced.

Three sophisticated commercial strain gauges were placed approximately at the midpoint of one segment, to measure large bending-induced stresses during deformation. Strain gauges were first housed in a 3D-printed Thermoplastic Urethane (TPU) box, and they were embedded beneath the surface of the manipulator. These TPU boxes are flexible with negligible effect on the bending, and they can help to synchronize the bending experienced by the sensors and the manipulator, and to protect the sensors from breakage (Fig. 3.1 (a)-(III)). The change in the sensors' resistance values were converted into voltage signals through a converter.

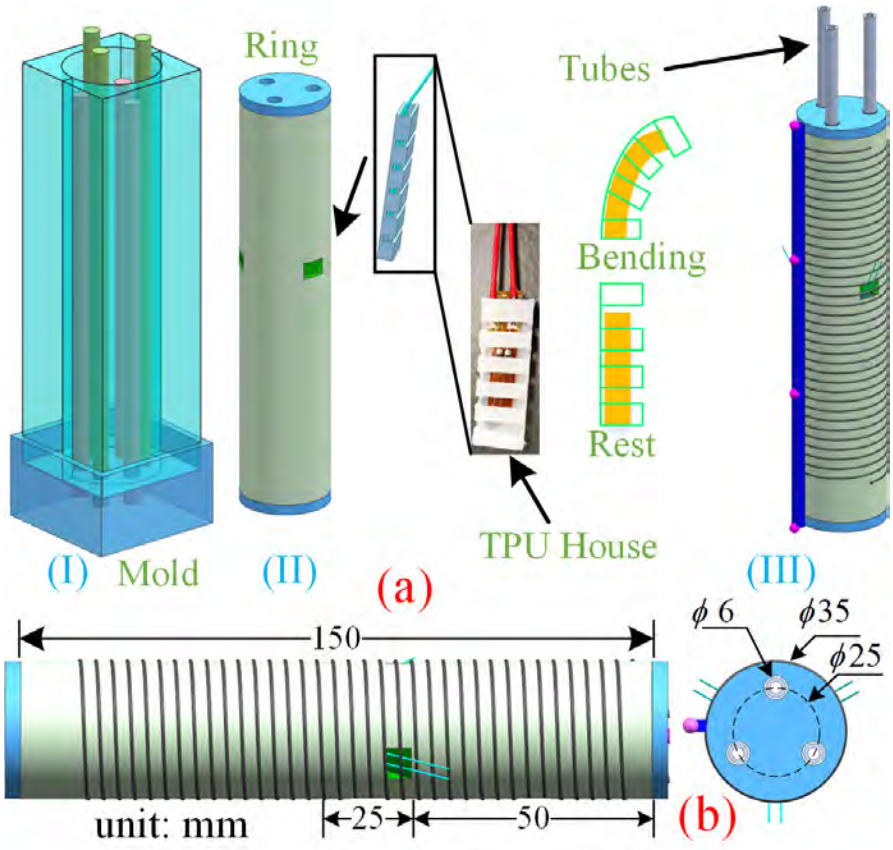

Fig. 3.1. Illustration of a soft manipulator. (a) Fabrication process. (b) Configuration of sensors. (unit: mm)

Fig. 3.1 (b) illustrates dimensions of the manipulator and the locations of the sensors. To enable visual verification, pink markers were labelled along the body as the key control points and the intermediate points were labelled in blue marker. For higher degree of dexterity, another segment was fabricated using the same method and was attached at the end of the first segment with 60° phase shifted. The whole pneumatic-driven manipulator was mounted on an aluminium frame, as shown in Fig. 3.2. The inner tubes were connected to pneumatic pressure regulators (SMC, ITV0030-BL). To evaluate the true position of the backbone, an RGB-D camera (Intel Realsense D415) was employed at a rate of 60 fps. The RGB-D camera was properly calibrated which can detect the Cartesian positions of different markers as the ground truth. Readings from the bending sensors were collected via Arduino, and sent to MATLAB 2019b for further processing. Fig. 3.2 (a) shows the commands and signals stream among hardware.

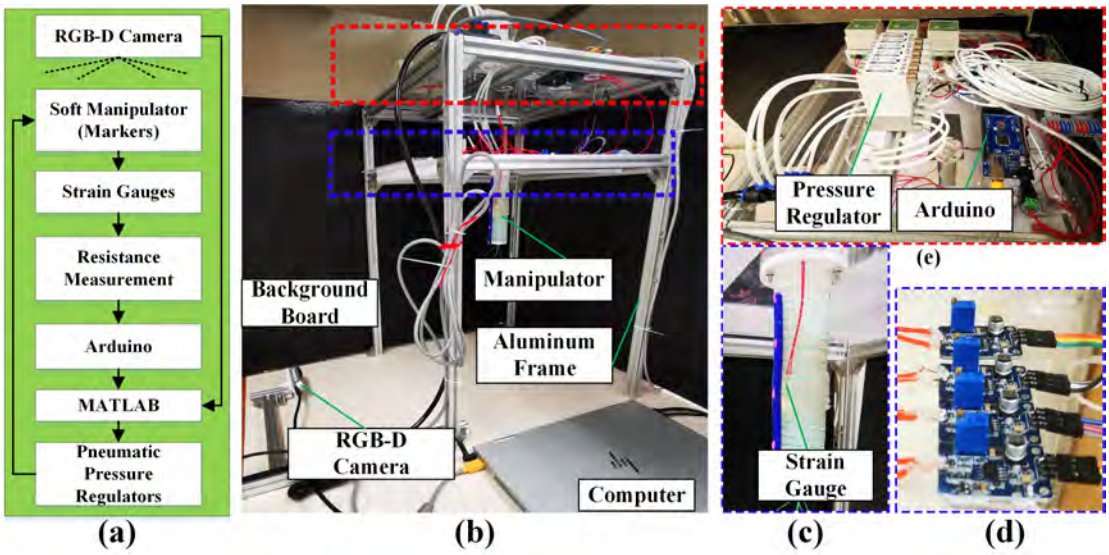

Fig. 3.2. Overview of the experimental testbed. (a) System operation flowchart among hardware. (b) Overview of hardware setup. (c) Detail of manipulator. (d) Electronic resistance to voltage converter. (e) Pneumatic pressure regulators.

3.2.2 Sensor Selection and Performance

A total of six strain gauges (BF350-6AA) were employed to sense the deformation of the continuum robot for the two segments. As the robot continues to bend, the sensors can output a signal according to the change in the curvature due to the bending. The advantages of thin strain gauges over other sensors such as FBG is that it has a relatively low stiffness, which can cause less influence to the specimen being measured. In addition, strain gauges can be mounted on the surface of the manipulator, rather than at a distance from the neutral axis, which can help to improve the maximize the sensor reading due to the bending effect. The advantages of thin strain gauges over other sensors such as FBG is that the readings can better sense the change in the curvature on the surface of the manipulator due to its large deformation angle, and immunity to environmental change. A single-segment manipulator was used as an example to investigate the performance of the bending sensors. We actuated two chambers and increased the pressure from 0 bar to 0.7 bar at an increment of 0.1 bar. Load-free and load conditions were compared to investigate sensors' performance. For the load scenario, an aluminum block (119g) was attached at the distal end of manipulator.

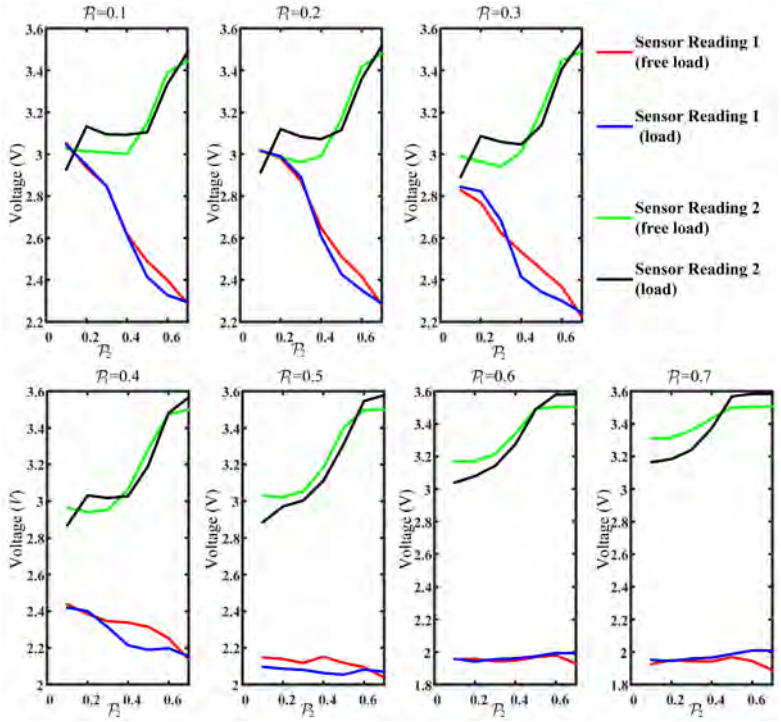

Fig. 3.3. Sensor readings from two strain gauges under load-free and load scenarios. Take a single segment and two sensors to investigate the sensor performance.

Fig. 3.3 shows the comparison of the readings from the two sensors in the two scenarios. Increasing actuation pressure leads to a higher degree of deformation, and the sensor readings responded accordingly. The effect of the additional load on the sensor readings was obvious, which confirms that the sensors output a different sets of sensor readings. In addition, as shown in Fig. 3.3, both pressure inputs and sensor readings can provide useful information to evaluate the shape of the manipulator, but the sensor readings are unique to the load status. Although an analytical approach could be used to convert the sensor readings into the degree of deformation of the manipulator, other information parameters, such as the material properties, geometrical parameters of the manipulator as well as the sensor locations are all required. Hence, Neural Networks (NNs) will be employed to build a black box to map between deformation and sensor readings.

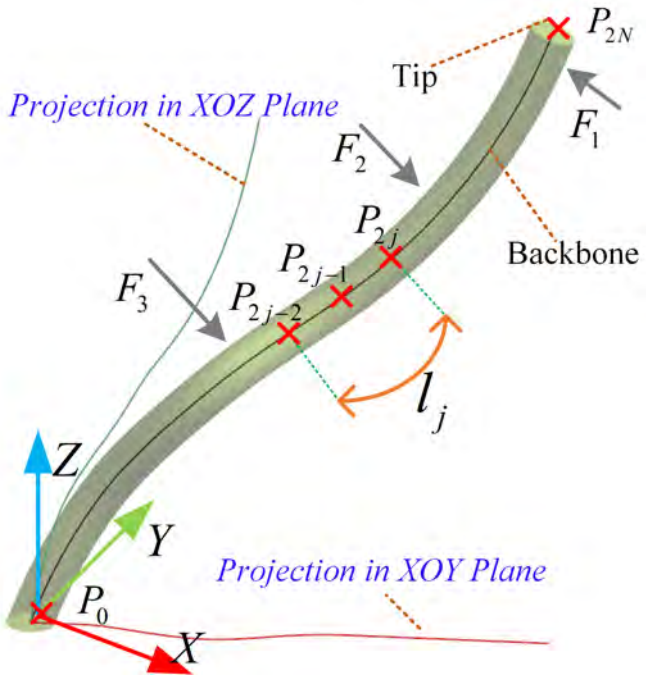

Fig. 3.4. Illustration of continuum robot being disturbed by external forces. $F_1, \cdots, F_4$ are lateral forces, which lead to spatial backbone not a simple arch.

3.3 Shape Reconstruction Approach

To reconstruct the shape of continuum robot both in free scenario and in situations with uncertain payloads, a data-driven approach was considered in this work. When a continuum robot is experiencing an external payload, as shown in Fig. 3.4, the shape does not necessarily follow the PCC approximation (the projection in XOY is not a line). An alternative way to reflect the shape is through the backbone, and the shape reconstruction problem can be converted as finding the accurate position of the points on the backbone as many as possible. This can also be divided into two steps: 1) find the control points on the backbone with reference to the global coordinate system, and then 2) use a curve fitting method to connect these control points together. To balance between the accuracy and the computation burden, one continuum robot with length of L is divided into N subsegments, labelled as l_j (See Fig. 3.4). The curvature of a subsegment can be represented by three key points $(P_{2j-2}, P_{2j-1}, P_{2j})$. Therefore, the first step is to find the position of all key points in each segment, which is achieved via NNs in this work, and the second step is to estimate the backbone using the key points

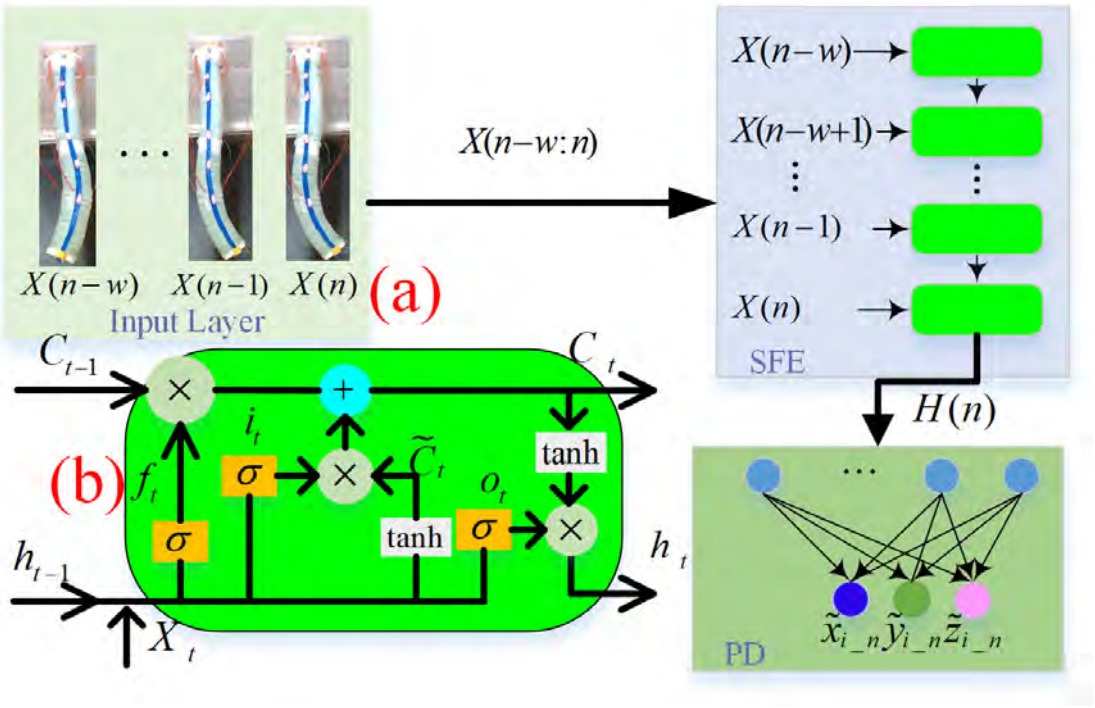

Fig. 3.5. (a) Framework of one key point prediction Neural Network. (b) Illustration of a LSTM cell.

with proper fitting algorithm.

3.3.1 Key Points Prediction

Due to the uncertainty of external loads and imperfection of fabrication, it is challenging to find the explicit mapping between the position of the key points with the sensor readings. As the actuator inputs and sensor readings are both related to the shape of robot, a data-driven approach was employed to evaluate the position of the key points and factors involved in them. Intuitively, the shape of the manipulator depends on internal forces and external forces, so actuation inputs and external payloads (reflected via sensor readings) were both regarded as the factors. Let A_n and S_n respectively denote the actuator inputs and the sensor readings in control instance n, and the position of the ith key point P_{i_n} is $(x_{i\_n}, y_{i\_n}, z_{i\_n})$. Let $X(n) = \{A_n, S_n\}$ denote the input and $Y(n) = P_{i\_n}$ is the data to be estimated. Since the positions of different key points are sequentially dependent to each other over time, the temporal relationship (w states before epoch n) between data are included, and the signal data and output data for the

key point P_{i_n} are:

$$\begin{cases} X(n-w:n) = \{A_{n-w}, S_{n-w}, \cdots, A_n, S_n\} \\ Y(n) = \{x_{i\_n}, y_{i\_n}, z_{i\_n}\} \end{cases}. \tag{3.1}$$

The data was normalized within $[-1, 1]$ using *Z-score* method before training. We set $w = 5$ in this work. A separate model was used to train and evaluate each key point, as shown in Fig. 3.5 (a). The network architecture mainly includes two components: 1) Sequence Feature Extractor (*SFE*) and 2) Position Decoder (*PD*). First, the *SFE* extracts all the input data and obtains a feature vector $H(n)$, which represents the status at current instance and previous information. Then, *PD* decodes this feature and estimates the position of the key point.

1) *SFE Layer*: the *SFE Layer* was constructed using long short-term memory Neural Networks (LSTM-NNs), which is powerful in processing sequence data. A basic illustration of LSTM cell is shown in Fig. 3.5 (b). There are three gates, namely input gate, forget gate and output gate. They work effectively to memorize pheromone in sequence and selectively forget unimportant features. It can be mathematically expressed as:

$$\begin{aligned} f_t &= \sigma(W_f X_t + w_f h_{t-1} + b_f) \\ i_t &= \sigma(W_i X_t + w_i h_{t-1} + b_i) \\ \tilde{C}_t &= \tanh(W_c X_t + w_c h_{t-1} + b_c) \\ O_t &= (W_o X_t + w_o h_{t-1} + b_o) \\ C_t &= f_t * C_{t-1} + i_t * \tilde{C}_t \\ h_t &= O_t * \tanh(C_t) \end{aligned}, \tag{3.2}$$

where W_f, W_i, W_c, W_o respectively denote the weight matrices of X_t, and w_f, w_i, w_c, w_o are the weight matrices of h_{t-1}. b_f, b_i, b_c, b_o are bias vectors, and $\sigma(\cdot)$ is sigmoid function.

2)*PD Layer*: This component is a fully connected NN (FCN), which has a hidden layer and an output layer. In the hidden layer, the kth node processes the sequence feature $H(n)$ by:

$$f_k(H(n)) = \sigma(u_k H(n) + b_k), \tag{3.3}$$

where $\sigma(\cdot) = \frac{1}{1+e^{-x}}$ is activation function, and u_k, b_k are weight and bias, respectively. In the output layer, there are three nodes to compute the coordinate of key point $\tilde{P}_i(\tilde{x}_{i\_n}, \tilde{y}_{i\_n}, \tilde{z}_{i\_n})$, each of which is obtained using linear activation function. It is calculated by:

$$\tilde{T}_{i\_n} = \sum_{k=1}^{w} u_j f_k + b_j, \tag{3.4}$$

where $\tilde{T}_{i\_n}$ denotes an item in the output layer, and u_j, b_j are weight and bias of the jth node, respectively. During the implementation, to avoid overfitting, a dropout layer with rate of 0.3 is designed between *SFE* and *PD*. The Adam optimization algorithm was used in training and the initial learning rate was set to 0.001. Mean square error was used to define the loss function in training, which is:

$$L(P_i, \tilde{P}_i) = \frac{1}{3M} \sum_{j=1}^{M} \left\| P_{j,i} - \tilde{P}_{j,i} \right\|, \tag{3.5}$$

where M is the total number of training data, and $\|\cdot\|$ is L_2 norm. Since the error between $\tilde{P}_i$ and P_i always exists for each application, the maximum deviation between the true value (obtained from vision system) and the predicted value (via *SFE-PD* NNs) can be denoted as

$$\xi = \max_{1 \le i \le 6} \left\| \tilde{P}_i - P_i \right\|, \tag{3.6}$$

which is also shown in Fig. 3.6 (a) (blue sphere). This deviation is highly involved in the accuracy of the estimated backbone.

3.3.2 Backbone Fitting

After finding the value of all the key points, system then should connect them smoothly to approximate the true backbone with curve fitting algorithm. Fig. 3.6 (a) shows the backbone of the first subsegment, in which the three key points are O, P_1, P_2. The origin O is assumed to be fixed. The continuum robot has two segments with a total of seven key points, leading to three subsegments to be fitted. For any subsegment l_j, it can be represented by a spatial function $z_j = \psi_j(x, y)$. A

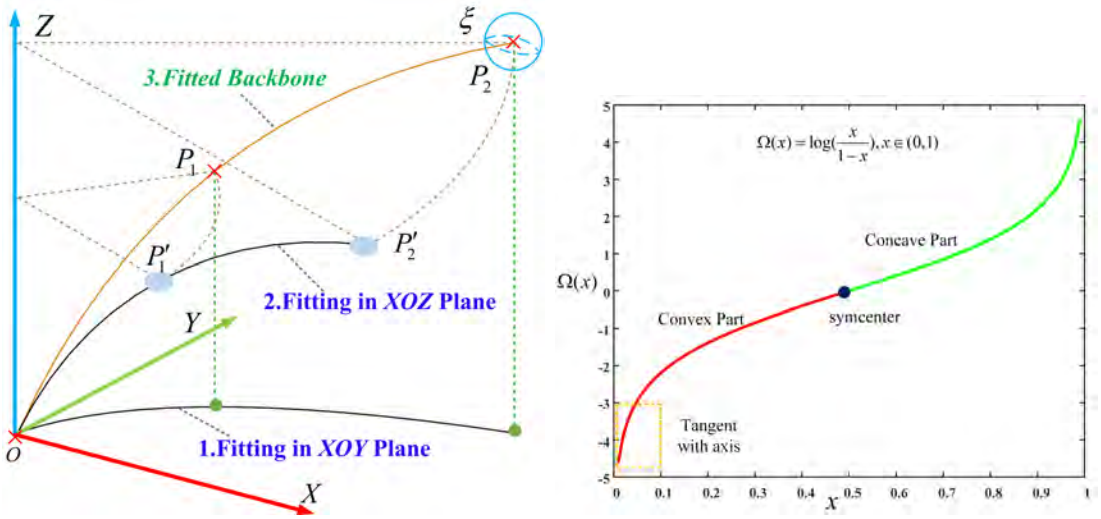

(a) (b)

Fig. 3.6. (a) Illustration of the first subsegment, whose backbone is projected onto XOY and XOZ planes for fitting separately. (b) Basic illustration of ISF. This function is smooth and the initial part (marked by yellow rectangle) is tangent with Y axis, so it is applied to fit $Z_j(x, y)$.

two-stage evaluation scheme was considered and the backbone was first projected onto the XOY plane and the XOZ plane to evaluate the y coordinates and z coordinates in terms of x. The new spatial curve functions become:

$$\begin{cases} y = Y_j(x) \\ z = Z_j(x, y) \end{cases} . \tag{3.7}$$

1) *Fitting in XOY plane*: Since the backbone projection on the XOY plane should exhibit a curvilinear shape, a parabolic equation was considered to approximate the $Y_j(x)$ function. For the key points with x-coordinates ($x \in [x_{2j-2}, x_{2j}]$), the function can be expressed as: $Y_j(x) = A_j x^2 + B_j x + C_j$, where A_j, B_j, C_j are parameters to be solved. This function should satisfy two conditions: 1) output of this function at the three key points must be equal to their respective true y value, and 2) the slope at the starting end of the segment must be equal to the slope at the end of the previous segment $Y_{j-1}(x)$ for continuity. With totally four constraints and three parameters, an optimization algorithm was used to solve for

the unknown parameters, which is:

$$\begin{aligned} &\text{minimize} \sum_{i=2j-1}^{2j} \|Y_j(x_i) - y_i\| \\ &s.t. \begin{cases} {Y'}_{j-1}(x_{2j-2}) = {Y'}_j(x_{2j-2}) \\ Y_j(x_{2j-2}) = y_{2j-2} \end{cases} . \end{aligned} \tag{3.8}$$

2) *Fitting in XOZ plane*: The three key points were then projected onto the XOZ plane and $P_i(x_i, y_i, z_i)$ was updated to: $P_i' = (\sqrt{x_i^2 + y_i^2}, 0, z_i)$, as depicted in Fig. 3.6 (a). Due to the large variation on the z-curve for different backbone shapes, the inverse of sigmoid function (ISF) was considered to approximate the z function. The basic illustration of ISF is illustrated in Fig. 3.6 (b). It consists of two parts: convex part and the concave part, divided by the symcenter. The convex part is similar to the shape of the backbone. It is tangent with the y axis and keeps smooth with the increase of x. Therefore, the fitting can be expressed as:

$$\begin{cases} t = \sqrt{x^2 + y^2} \\ Z_j(x, y) = Z_j(t) = D_j \log[\frac{t - E_j}{F_j - (t - E_j)}] + G_j \end{cases} . \tag{3.9}$$

where $x \in [x_{2j-2}, x_{2j}]$, $y \in [y_{2j-2}, y_{2j}]$, and $D_j \cdots G_j$ are parameters to be solved. Similar to fitting $Y_j(x)$, constrained optimization algorithm was applied to solve the control parameters, which is:

$$\begin{aligned} &\text{minimize} \sum_{i=2j-1}^{2j} \|Z_j(x_i, y_i) - z_i\| \\ &s.t. \begin{cases} 0 < D_j \\ E_j < \min(t) \\ 2\max(t - E_j) < F_i \\ Z_j(x_{2j-2}, y_{2j-2}) = z_{2j-2} \\ {Z'}_{j-1}(x_{2j-2}, y_{2j-2}) = {Z'}_j(x_{2j-2}, y_{2j-2}) \end{cases} . \end{aligned} \tag{3.10}$$

The five constrains are summarized as follows. 1) to ensure that $Z_j(x, y)$ is positive; 2) to ensure that numerator of (3.9) is positive; 3) to ensure $Z_j(x, y)$ is in the convex part of ISF, which is similar to the backbone; 4) to ensure the continuity between $Z_j(x, y)$ and $Z_{j-1}(x, y)$; and 5) to ensure the continuity of slope. Note that the last constraint in (3.10) is only feasible for $j \geq 2$, and $Z_1'(x_0, y_0) = \tan(89°)$ was set for $j = 1$.

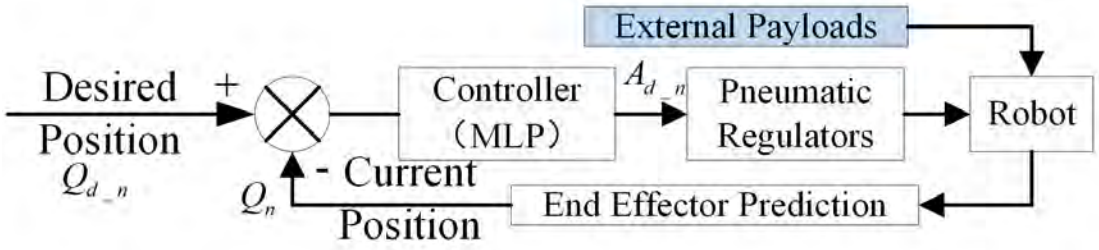

Fig. 3.7. Closed-loop control scheme with self-feedback mechanism.

3.4 Control Scheme

The properties of a flexible manipulator under uncertain external payloads make it difficult to control the robot accurately. Hence, closed-loop control was incorporated to deal with this problem. Based on the position estimated from the SR module, a control scheme was developed as shown in Fig. 3.7. It should be noted that robot's tip is the same as a key point predicted by one *SFE-PD* frame. Let Q_d and Q_n respectively denote the desired position and current position of the tip, and A_{d_n} is the theoretical actuation inputs computed via controller in control instance n.

3.4.1 Jacobian-Based Control Scheme

In robotics, the Jacobian matrix can be used to map between the velocity of end effector and the actuator configuration, which is:

$$Q'_n = JA'_n, \tag{3.11}$$

where J is Jacobian matrix, and $(\cdot)'$ is the first derivative. Theoretically, within a short time interval, (3.11) can be rewritten as:

$$Q_d - Q_n \approx J(A_{d\_n} - A_n). \tag{3.12}$$

Using (3.12), the required A_{d_n} for a given Q_d can be computed as: $A_{d\_n} \approx J^{-1}(Q_d - Q_n) + A_n$. It should be noted that (3.12) is derived from velocity-level mapping and transferred into displacement-level relationship, such that only quasi-static behavior of robot is considered and the effect of inertial is neglected.

Furthermore, the Jacobian matrix varies at different locations and J is not a constant matrix. The the term J can be updated to J_n to represent the value, and A_{d_n} can be obtained via:

$$A_{d\_n} = J_n^{-1}(Q_d - Q_n) + A_n. \tag{3.13}$$

The challenge for this solution is to precisely find J_n at different locations, though external payloads have not been considered and J_n is likely to be not full rank, making it not unable to find its inverse. To address this issue, a mapping function $g_n(\cdot)$ was designed with the aim of covering the whole task space just with this model, since Artificial Neural Networks have the powerful ability of generality. Beside, the effect of external forces should be considered, and $g_n(\cdot)$ taking sensor reading S_n into account can be expressed as:

$$A_{d\_n} = g_n(Q_d, Q_n, A_n, S_n), \tag{3.14}$$

where $\|Q_d - Q_n\| = d$, such that $g_n(\cdot)$ is only feasible in a small task space. A learning approach was implemented to find the required actuator inputs based on the known information, and $g_n(\cdot)$ can be replaced by a well trained NN framework to cover whole task space. Notably, in work [128], the mapping relationship is assumed to be locally linear, which was proven to be robust to against disturbances. Therefore, the local mapping which also factors the loading effect can be updated to:

$$A_{d\_n} \leftarrow g(Q_d, Q_n, A_n, S_n). \tag{3.15}$$

Since this local mapping is only feasible in a small region, the robot system should generate a temporal position Q_{t_n} if Q_d is located far away from Q_n, via:

$$Q_{t\_n} = Q_n + d\frac{\overrightarrow{Q_nQ_d}}{\left|\overrightarrow{Q_nQ_d}\right|}, \tag{3.16}$$

and the end-effector will gradually move to the desired position. The step distance d can be adaptively updated based on the external payloads and to minimize the error between Q_{t_n} and Q_n. In general, a larger d should be used when external

payloads exist, while a smaller d can be adopted when the end-effector is close to the destination. The robot can stop moving if $\|Q_d - Q_n\| \leq E$, in which E is the acceptable error between current position and destination.

3.4.2 Adaptive Step Distance Mechanism (ASDM)

The step distance d can be replaced to d_n, which can be adjusted according to the error between the temporal destination Q_{t_n-1} planned in instance $(n-1)$ and the actual current position Q_n in epoch n. The error e_n is:

$$e_n = \left\| Q_{t\_n-1} - Q_n \right\|. \tag{3.17}$$

The error was considered to update the d_n adaptively, and the equation is:

$$d_n = d_{n-1} + \text{sgn}(\overrightarrow{Q_{n-1}Q_n} \cdot \overrightarrow{Q_{n-1}Q_{t\_n-1}}) \cdot K \cdot e_n, \tag{3.18}$$

where $\text{sgn}(\cdot)$ is sign function and K is a gain constant regulating the influence from position error e_n. To avoid the instability of the local controller, we limit $2mm \leq d_n \leq 15mm$.

3.4.3 Architecture of Locally Learned Controller

A Multiple Layer Perceptron (MLP) was used to build the mapping $g(\cdot)$. The input layer has 18 nodes $(A_n^{1\times6}, Q_n^{1\times3}, Q_{t\_n}^{1\times3}, S_n^{1\times6})$ and the output layer has 6 nodes for $A_{d\_n}^{1\times6}$. Two hidden layers are attached after the input layer with size of 7 and 5 respectively. The activation function of hidden layer is also sigmoid. Rectified Linear Unit (ReLU) is selected as the activation function of the output layer because the output pressure of pneumatic regulators is always non-negative, and ReLU is:

$$\text{ReLU}(x) = \max(0, x). \tag{3.19}$$

Thus, the loss function of this framework is derived as:

$$L(A, \tilde{A}) = \frac{1}{6M} \sum_{M} \sum_{i=1}^{6} \left\| A(i) - \tilde{A}(i) \right\|, \tag{3.20}$$

where M is the number of training data and i is the index of pneumatic regulators. The operation process of the robot system, fusing SR module and controller, is outlined in Algorithm 1.

Algorithm 1: Operation process of the robot system.

Input: Q_d, K, E, $n = 1$, d_1
Sample sensor readings: S_1
Calculate: Q_1=*SFE-PD*(6)
while $\|Q_d - Q_n\| > E$ **do**
  Set temporary destination Q_{t_n} using (3.16)
  Compute: $A_{d\_n} \leftarrow g(Q_{t\_n}, Q_n, A_n, S_n)$
  Actuate pneumatic regulators using A_{d_n}
  Sample sensor readings: S_{n+1}
  for $i = 1$ *to* 6 **do**
    predict key points: $\tilde{P}_i \leftarrow$ *SFE-PD*(i)
  end
  Fit the backbone and visualize it
  Calculate: $e_n = \left\| Q_{t\_n} - \tilde{P}_6 \right\|$
  Update d_{n+1} using (3.18)
  $n \leftarrow n + 1$
  Compute current position of end effector: $Q_n = \tilde{P}_6$
end

3.5 Simulation

Before testing the proposed algorithm, simulation was conducted. To examine the performance of the proposed Shape Reconstruction method, it was first compared with the shape generated by finite element method (FEM). The control scheme was also compared with the performance based on piecewise constant curvature model.

3.5.1 SR Simulation Using FEM

The error function used to evaluate the position deviation on the shape between the fitted backbone and the backbone from FEM can be defined as:

$$Err = \frac{1}{60} \sum_{k=1}^{60} \left\| P_{true\_k} - P_{fitted\_k} \right\|, \tag{3.21}$$

Table 3.1: Material Properties of the Manipulator.

Part	Elasticity Modulus	Poisson's Ratio	Density(g/cm^3)
Soft Manipulator	15 Psi	0.48	1.07
Ring and Fixator	3 GPa	0.35	1.29

Table 3.2: Mean Error of Each Fitted Backbone with Different Error of Key Points (unit:mm).

Actuated Chambers	$\xi = 0$	$\xi = 2$	$\xi = 3$	$\xi = 4$
1,4	2.83	3.08	3.29	3.46
1,5	3.16	3.88	3.97	3.61
2,4	2.91	3.31	3.58	3.68
2,5	3.18	3.23	3.35	3.59
3,5	2.55	2.69	2.92	3.34
3,6	2.69	2.73	3.17	3.41
1,2,4,5(Tors.)	2.42	2.76	3.21	3.53
2,3,4,6(Tors.)	2.53	2.87	3.32	3.59

where 60 points on the backbone were used to compare the shape and their values can be obtained from the FEM simulation, denoted as the true (theoretical) backbone P_{true_k}, and through the fitting algorithm, denoted as P_{fitted_k} accordingly. The material properties used in the simulation are listed in Table 3.1. Other parameters and settings are learned from literature [129]. Ogden material model was selected to model the stress-strain behavior of the soft body, and the body was meshed using tetrahedral elements, as depicted in Fig. 3.8 (a). A total of 20254 linear elements and 38212 nodes were generated. The centreline along the backbone was extracted to evaluate the positions of the true backbone (including 60 points), as well as the seven key points (gapped with 50mm) used in the fitting algorithms. Six chambers were used to actuate the two segments, where number 1-3 were supplied to the proximal chambers, and number 4-6 were supplied to the distal chambers. Four forces ($1N$) that were evenly distributed along the $300mm$ long backbone ($60mm$ apart), and they were 90° shift to spirally act on the manipulator, mimicking the external payloads (Fig. 3.8 (a)). Eight different actuation configurations covering the entire task space were examined, where each actuated chamber is pressurized with 1 bar at a time. To mimic error in estimating the

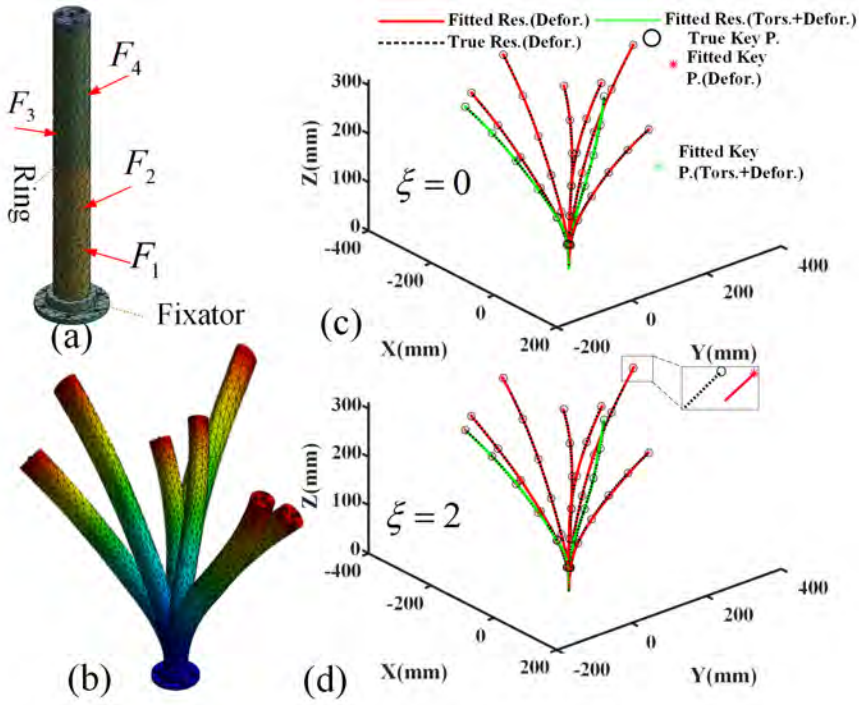

Fig. 3.8. Illustration of FEA results. (a) Meshed plot of continuum robot, with four external forces. (b) Deformation of the robot under six scenarios. (c)-(d) Comparison of fitted backbone and true backbone.

six key points through NNs, a random error ξ, in a range between 0 to $4mm$, was deliberately added to the six key points (except the origin), and new key points used in the fitting algorithm become $\tilde{P}_i = P_i + U(-\xi, \xi)$, where $U(\cdot)$ is Uniform Distribution. The results of the bending status are shown in Fig. 3.8 (c)-(d). The acting position of F_1 is changed to the edge of the manipulator, such that torsion and deformation occur simultaneously. It can be observed that the shape from the fitting algorithm is matched with the FEM simulation. The fitting error under different actuation configurations are listed in Table 3.2. It can be seen that when the error of the key points increases (i.e. a larger ξ), the fitting curve starts to deviate from the FEM simulation results and a larger Err was observed, as summarized in Table 3.2. Based on the results, the maximum error of the estimated key points should be limited within $3mm$, otherwise the estimated shape from the proposed algorithm will not be accurate enough.

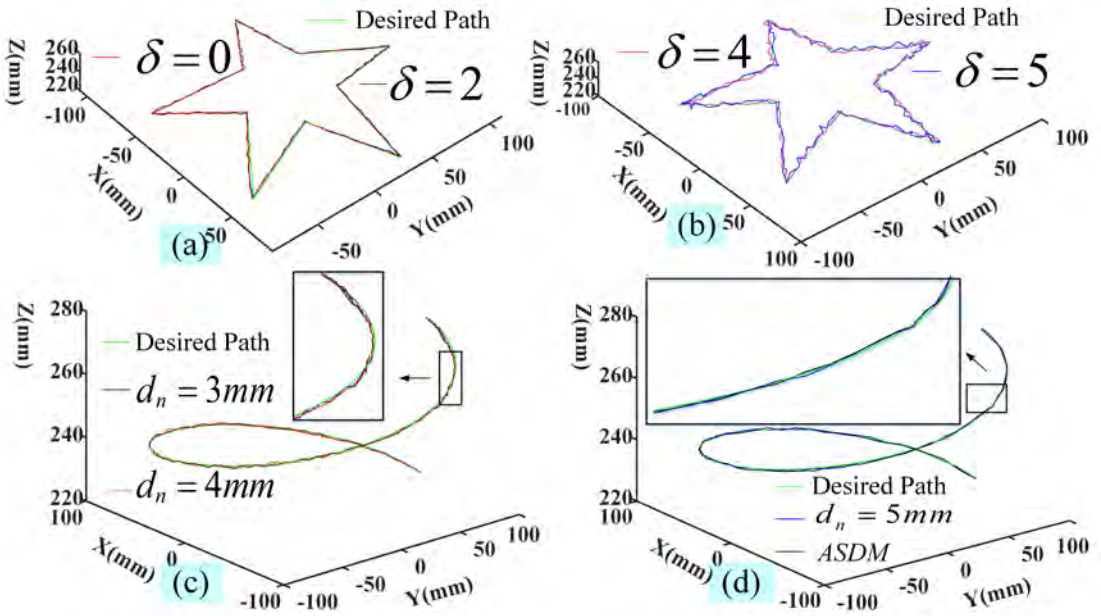

Fig. 3.9. Simulation results for the control scheme. (a)-(b) the path following tests on a star-shaped path, where noise is variable. (c)-(d) tests on a spiral path, where noise is constant and different step distance is used.

3.5.2 Path Following Simulation

To test the proposed control scheme in a simulation manner, a computer model for a two-segment continuum robot based on PCC assumption was set up for collecting training data and validating the performance of the trained model. During data collection, the length of each chamber was commanded to vary within $[140mm, 160mm]$. It should be noted that all the six chambers can only elongate by $2mm$ or $-2mm$ randomly in an exploration, to ensure that adjacent position data are located nearly. As a result, 4000 sets of training data were obtained in load-free manner. Since sensor readings are not available in the simulation, the input layer of MLP was reduced to 12 nodes ($A_n \in R^{6\times1}$, and $Q_n, Q_{dn} \in R^{3\times1}$). Other settings about training controller is the same as that defined in section-3.4. Two experiments related to testing the disturbance handle ability and the performance of $ASDM$ were conducted, where E is $2mm$ and K is 0.12 (through empirical setting). First, a star-shaped path following task was prepared, including continuous discrete points on the path, and end effector was commanded to arrive them one by one. The step distance d_n was set as $5mm$, and different dis-

turbance was considered for comparison. The effect from external payload was simplified as error leading to the position offset on the end-effector, which means $Q_n \leftarrow Q_n + N(0, \delta)$ ($N(0, \delta)$ is Gaussian white noise with mean of zero and variance of δ). The results are shown in Fig. 3.9 (a)-(b). When $\delta = 0$, the true path was almost consistent with the desired path, and when a larger δ was considered, the actual path gradually deviated the desired path, but the end effector could still reached the destinations and complete the path.

Second, the feasibility of the proposed *ASDM* was examined, where the noise δ was set to 5, and the step distance d_n was updated adaptively. In this test, a spiral path was prepared. We initially set $d_n = 4mm$ to follow the desired path. As shown in Fig. 3.9 (c), the end effector fluctuated near Q_{d_n}, and it took 182 steps to finally arrive the destination. Several phenomenon can be observed from the simulation. First, when a smaller step distance ($d_n = 3mm$) was selected, the effect from the external payload on the end-effector becomes more obvious, leading to a larger error. When the step distance increases to $5mm$, and it only took 125 steps and the actual path is closer to the desired path, as shown in Fig. 3.9 (d). When the *ASDM* was adopted, the robot only needed 116 steps to complete the path. The fluctuation on the end-effector was very minimal, showing the robustness of the proposed adaptive controller to handle external disturbances.

3.6 Experimental Results

While the results from simulation confirm the feasibility of the proposed methodology, the algorithms were implemented onto the robot system to examine experimentally. Since both the SR module and control scheme are built using data-driven approach, training data was sampled first, and the actual performance of the two modules are respectively evaluated. In testing, the RGB-D camera only collected the true position of backbone and key points for comparison, providing no information for the robot system.

3.6.1 Model Preparation

The robot was commanded to randomly explore within the task space by supplying different pressures to the six chambers. The maximum pressure was limited to 0.8 bar to avoid over-pressure. At each instance, any two of the six chambers were randomly adjusted to increase or decrease the pressure by 0.05 bar so as to ensure a small, incremental change in the shape between the previous and the new state. After 1 second, the position of the backbone was obtained through the RGB-D camera, which was assumed as the ground truth, and the sensor readings were simultaneously recorded too. 6000 groups of data were collected, including the position of the backbone, the position of key points, sensor readings and actuation configurations. 4000 groups of them were collected from the free state (no load), and the remaining 2000 were from the load state. A weight with 75 grams was attached to the tip of robot, resulting a $0.75N$ downward pulling force at the end-effector. After data collection, each data was normalized within $[-1, 1]$, and the output of each NN was converted back to its original scale after inference to equalize the range of each variable. In training, each NN was commanded to be trained at most 1000 iterations or RMSE is smaller than 0.001, where the former 5500 sets were used for training and the rest was set for validation. As a result, the RMSE of *SFE-PD* and MLP were respectively 0.00093 and 0.00089, indicating the models were well trained.

3.6.2 Characterization of SR Module

Fig. 3.10 (a) shows the true bending state and the fitted backbone of this robot, where the six pneumatic pressure regulators were set to: 0, 0.5, 0.6, 0.8, 0.7, 0 (unit: bar). The coordinates of the corresponding key points that were sampled by RGB-D camera and predicted through *SFE-PD*, are listed in Table 3.3, which confirms that the error from each key point is smaller than $3mm$, namely $\xi = \left\| \tilde{P}_i - P_i \right\| < 3\text{mm}$. The fitted backbone was almost consistent with the true backbone (obtained by RGB-D camera). The fitting task needs only 0.28s in

Table 3.3: Comparison on key points between the truth and the predicted value (unit: mm).

Key Point	True Position	Predicted Position	Error
P_0	(0,0,0)	Needn't Prediction	
P_1	(-0.1,0.5,49.6)	(-0.1,0.4,48.3)	1.31
P_2	(4.2,4.9,90.1)	(3.9,4.35,91.2)	1.3
P_3	(3.8,9.6,133.2)	(4.1,10.3,135.2)	2.14
P_4	(-22.6,19.9,172.9)	(-21.7,21.1,172.1)	1.7
P_5	(-35.9,35.2,210.8)	(-36.2,34.1,211.7)	1.45
P_6	(-58.7,64.7,248.5)	(-59.2,65.3,250.2)	1.51

MATLAB 2019b Optimization Toolbox, which can almost ensure the SR module working in real time. The mean error calculated by (3.21) was $5.85mm$. Another 11 actuation inputs were set to get more shape states covering the whole task space for comprehensive testing. Fig. 3.10 (b) shows the fitted results and the true backbone, where the fitting errors were consistent with the previous testing. This further confirms the accuracy and feasibility of the proposed shape reconstruction method. The fitting results in load scenarios are also our focus, so we also compared the error in load and load-free conditions, where actuation inputs in one comparison were same but loads differed each other. For the load experiments, weight with 50g, 75g, 119g, and 150g were hung at the tip, where same actuation inputs were applied in an independent scenario to compare the position errors. Fig. 3.10 (c) shows the snapshots and the fitted backbone for four different actuation inputs, where the weight is 119g. The mean position error between the fitted backbone and the true shape(set four different actuation inputs and each of them consists of four external payloads), were computed and summarized in Table 3.4. From the results, the errors from the load scenarios were generally higher than that in load-free scenarios, indicating the external load can lead to larger errors in the prediction. However, the increase in the error was small, showing the proposed method is able to predict the key points for both load and load-free scenarios.

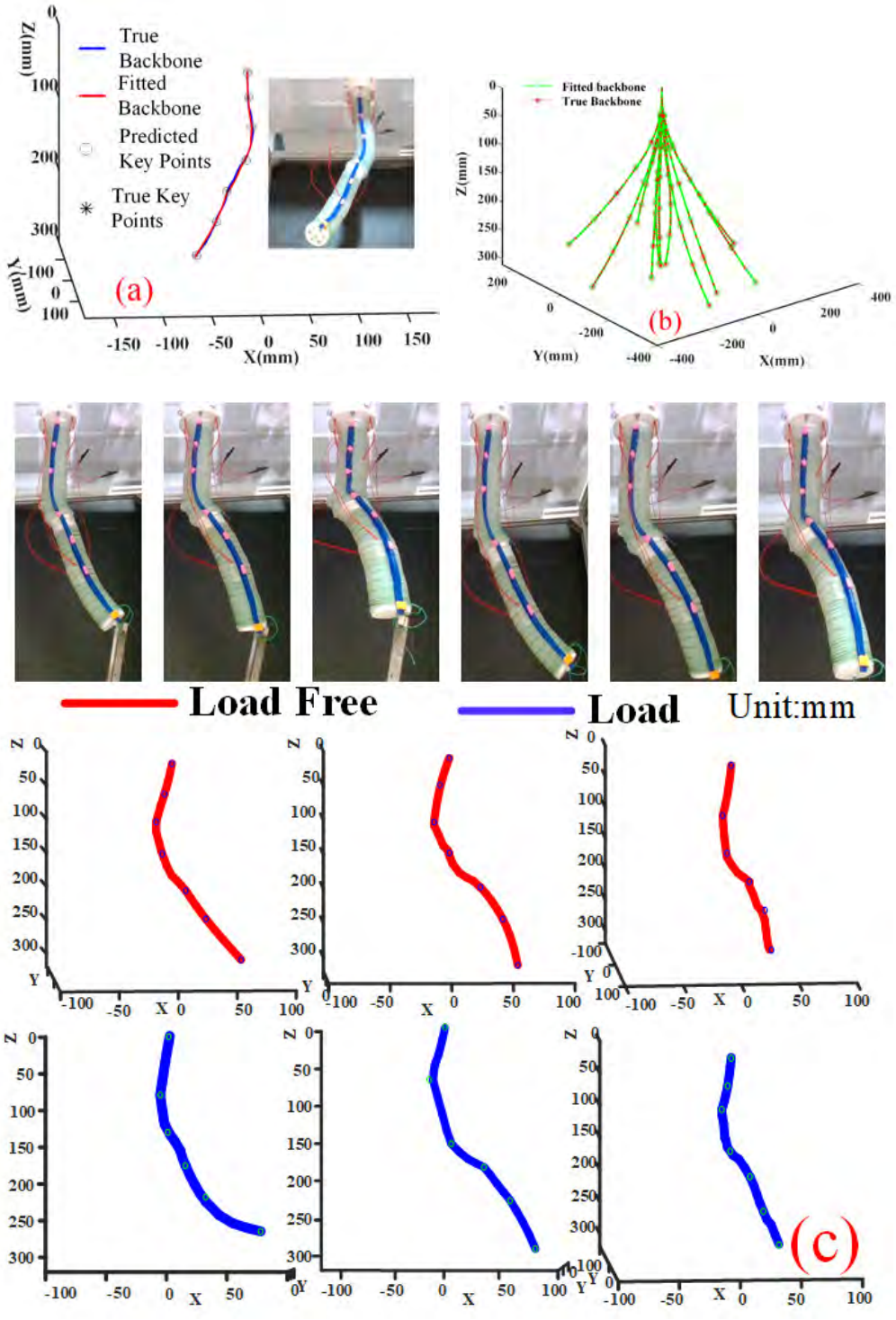

Fig. 3.10. (a) Illustration backbone fitting with one actuation configuration. (b) Shape reconstruction in the entire work space. (c) Fitted backbone in load and load-free conditions using the same actuation configurations.

Table 3.4: Fitting results between load free and load conditions (maximum error/mean error, unit:mm).

weight	1	2	3	4
free load	6.87/5.63	6.67/5.78	6.92/6.01	6.58/5.57
50g	6.78/5.64	6.71/5.81	6.94/5.97	6.73/5.62
75g	7.06/6.13	6.94/6.03	7.11/6.21	6.93/6.34
119g	7.12/6.24	7.26/6.31	7.34/6.41	7.05/6.28
150g	7.32/6.56	7.38/6.49	8.03/6.94	7.87/6.45

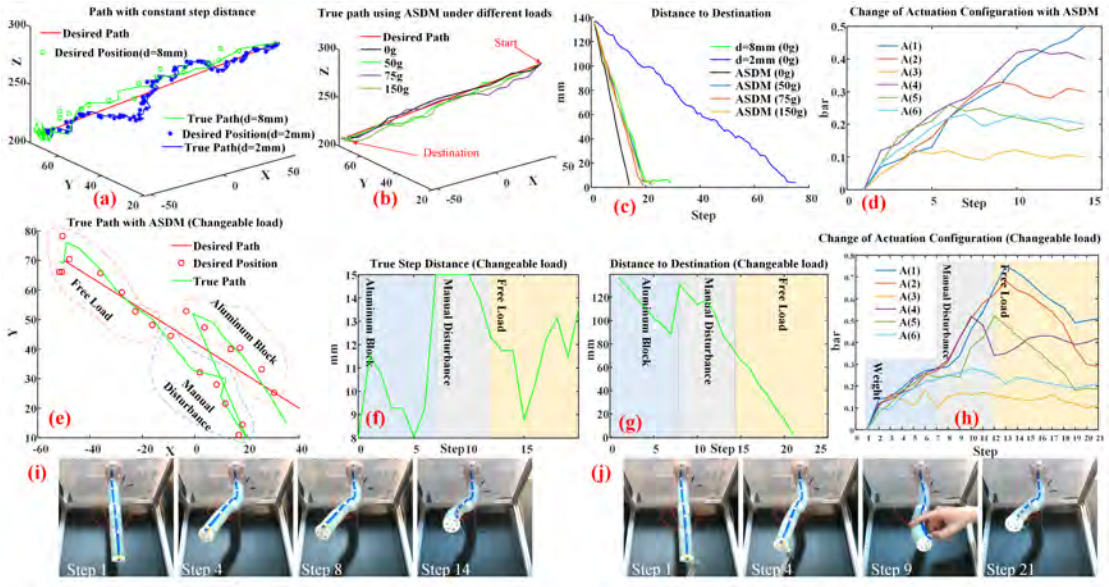

Fig. 3.11. Results of point-to-point movement task. (a)-(d) load-free scenario. (e)-(h) robot is moving with uncertain external payload. (i)-(j) snapshots of load-free state and uncertain disturbance state.

3.6.3 Point-to-Point Movement Task

The SR module can effectively provide accurate information on the position of the robot system, particularly the end-effector. In this experiment, the end effector was set to move from point (40,20,300) to point (-50,70,210) (unit: mm). E is set to 4mm, and K is also set to 0.12 empirically.

1) *Performance of Addressing Different Disturbances*

To investigate the performance of *ASDM* and the performance of the controller, four conditions were considered to achieve this point-to-point movement task, namely: I) $d_n = 8$, II) $d_n = 2$, III) $ASDM(d_1 = 8)$, IV) *ASDM* with different loads (statically hanging a tip load with 50g, 75g and 100g). Fig. 3.11 (a) and (b) shows the true path of I)- II) and III)-IV), respectively. Fig. 3.11 (c) shows the actual distance to destination for the four scenarios. When $d_n = 8$, the end-effector can reach to the desired point after 24 steps but it starts to fluctuate when approaching the destination (in the last 4 steps). In contrast, when $d_n = 2$, the end-effector can steadily reach the desired point but it took 75 steps. When *ASDM* was applied, the end-effector moved directly to the destination in 14 steps, and Fig. 3.11 (d) illustrates the corresponding change of actuation configuration of III). Fig. 3.11 (i) shows the snapshots of the III) scenario. Therefore, the results from the former three conditions prove the feasibility of *ASDM*. In condition IV), when tip load was not beyond 50g, robot followed the desired path well, and when the load increased, the true path deviated the desired more at initial steps, but it gradually moved towards destination, which demonstrates the controller can address external payloads.

2) *Performance of Addressing Changeable Payloads*

An additional experiment was conducted to test hybrid payloads. Initially, a swaying aluminium block (119g), was attached to the end-effector and caused position deviation from the desired path, but the error was generally reduced. At the 7th step, the aluminium block was replaced by a manual disturbance acting at the mid-point of the manipulator, which pulled the end effector to a new position

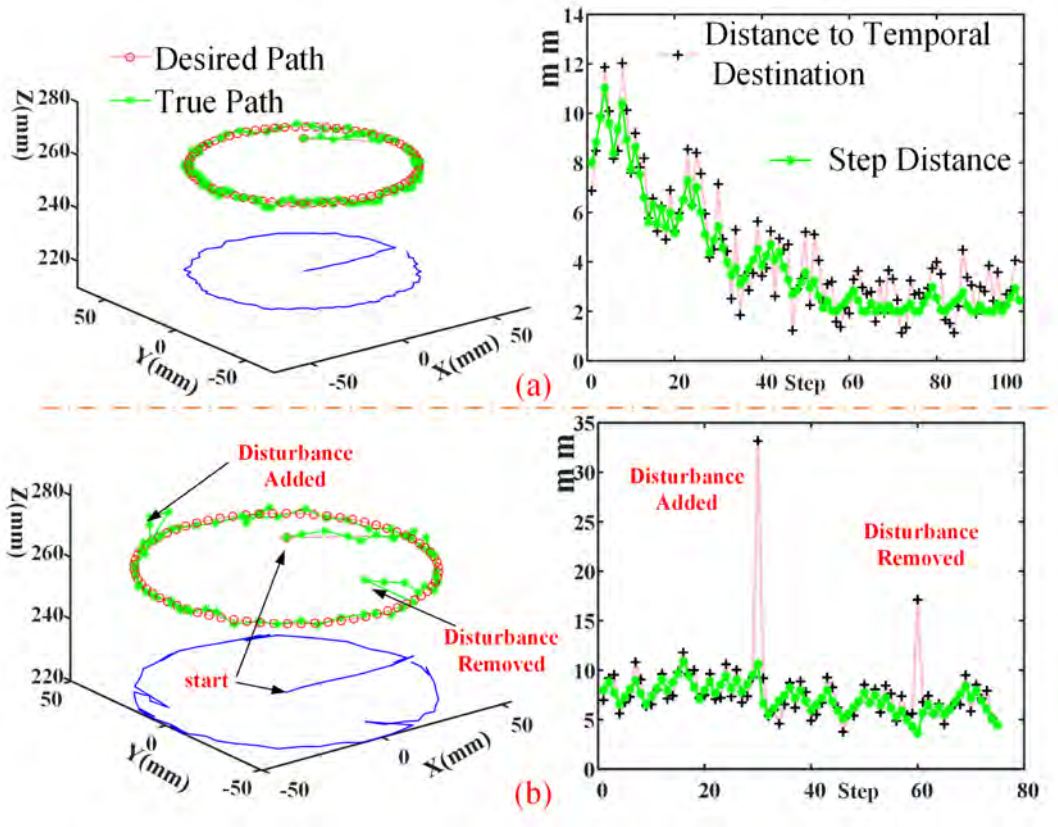

Fig. 3.12. Results of path following task, including true path corresponding step distance, and distance to temporal destination. (a) Load-free state. (b) Disturbance-added state.

$(19.8, 10.2, 303.6)$. At this moment, robot system sensed the disturbance then increased the step distance to $15mm$ (Fig. 3.11 (g) and (h). From step 7 to step 12), the robot tried to reject the external disturbance by adjusting the actuation configuration. At step 12, the manual disturbance was removed, and the robot gradually corrected the error and followed the planned path to reach the desired position. Fig. 3.11 (e) shows the true path from top view. The actuator inputs are comparable to the load-free scenario once the load was removed at step 12 (Fig. 3.11 (d) and (h)). This shows that our controller can also work when faced with changeable external payloads.

3.6.4 Path Following Task

Path following tasks were also examined with the proposed controller, and the path is composed of continuous path points. A circular path with a diameter of

$100mm$, was first examined. The initial step distance was set to $8mm$, as shown in Fig. 3.12 (a). Experimental results confirm that the end-effector can follow closely to the desired path, and the step distance changes adaptively. Second, external disturbance was added during the operation along the same path, and the results are shown in Fig. 3.12 (b). At the 29th step, an aluminium block (with 263g) was added at the end-effector, making its position deviate sharply from the desired path, but robot system gradually adjusted the step gap distance to follow the target points. At the 60th step, the aluminium block was removed, leading to a large position error again (See Fig. 3.12 (b)). The robot can still handle it and return to the desired path after 4 steps. Therefore, the proposed adaptive step distance mechanism plays a critical role in overcoming the influence from external payloads.

3.6.5 Experimental Results and Discussion

Time efficiency is a critical concern in motion. The time costs are about 0.013527s and 0.007275s respectively for one *SFE-PD* and the MLP-based controller (Intel i7 processor with NAVIDIA GeForce MX250), such that the time cost of all the NNs computation is 0.0884s. It averagely needs 0.28s to fit robot's backbone. The total time cost is 0.37s for one epoch. Furthermore, the shape estimation and control methods can be extended to robots with different dimensions and configurations. since the training data is unique to a particular robot configuration, new training datasets should be collected accordingly. Different scenarios, including free-load, point-load and distributed load, can all be included in collecting the data for training.

The maximum shape sensing error in our work is around $8mm$ with OD $35mm$ and length $310mm$. The error is highly involved in the length and OD. In comparison, most existing works obtained the key points directly using multiple sensors, such as RMSE=$13mm$ using vision system (Length: $287mm$, OD: $24mm$) in [130]. In [131], the error is $2.27mm$ using FBG with length around $40mm$. The error of

the key points is additionally considered in this work. As for the controller, it can adapt to different uncertain loads: point load, distributed load and mixing load. The control error is less than $4mm$ for this longer-and-bigger-diameter manipulator, which is comparable with other slender ones ($2mm$ in [132], 2.89% of length $160mm$ [133], and 2.23% of length $880mm$ [34]), so we believe this control is of high precision.

3.7 Chapter Summary

This chapter presents two important modules that are relevant towards precise control of a continuum robot subject to external payloads, namely the real-time shape reconstruction and the local inverse kinematics model. Based on the actuator inputs, *SFE-PD* NNs were first employed to estimate the different key points along the backbone and the shape was estimated through a fitting algorithm. Then, strain gauge signals were incorporated to into *SFE-PD* NNs model so as to compute the required actuator inputs to bring the end-effector to the desired position. An adaptive step distance scheme was used in the controller so that it can minimize the effect from external payloads. Simulation and experimental results both confirm that the SR module can effectively estimate the shape of the robot, while the local IK module can guide the end-effector to different positions, in both load and load-free scenarios.

The proposed shape reconstruction approach considered that the actual shape may not be a desired two-dimensional arch, especially when it is experiencing lateral external forces. While for long-scale continuum robots, the shape tends to be like a 3D curve. Additionally, the SR module was not only used for visualization, but also for practical control. It provides feedback for controller inputs.

Chapter 4

Uncertain External Force Estimation with Proprioceptive Mechanism

4.1 Motivation

Although the rapid technical innovation has promoted the development of continuum robotics in new material, robust control schemes and others, continuum robot also comes with challenges. Specifically, it is difficult to pinpoint the location and estimate the magnitude of an external force (EF) acting on a continuum robot in a constrained environment. The lack of information about the uncertain external force (UEF) can cause different degrees of changes on the shape of a soft manipulator, posing difficulty to design a proper control scheme for the robot. The UEFs are likely to present at any position of the robot body. The shape configuration is comprehensively determined by actuators and the forces. It requires delicate design of controller to minimize the influence of UEF and to maintain its previous shape configuration. Conventionally, controllers were built with complex algorithms to achieve this task, which generally causes burdensome computation. To this end, controllers should adjust actuators in a relatively blind manner. Therefore, it would be easier in designing controller and the control precision would be higher for the same computation complexity degree if the information of UEF is known by system. The information includes the acting positions and the magnitude.

Finding the location of the force can help users (e.g. surgeons) to better interact with the ambient environment, and adjust the actuation inputs accordingly to compensate the load effect. Thereby, sensors are indispensable. Externally located camera [134] is a good option to directly monitor the robot as well as the surrounding obstacles, but occlusion could be a problem in some scenarios. Therefore, research towards proprioceptive sensing has been developed. Examples of existing works include employing Fiber Bragg Grating (FBG) [135], Electromagnetic (EM) [84], Hall effect [48], stretchable optical waveguides [136], and color-related sensors [75] to achieve shape sensing and force sensing for soft robots, where the signal outputs correspond to the change in the robot shape. Similarly, there are some limitations in these sensing mechanisms. For example, FBG is not cost-friendly and has limited bending flexibility. EM and Hall-effect sensors are sensitive to the surrounding magnetic field presented in the environment. Optical waveguides and color sensors need complicated fabrication procedures for sensor integration and are not feasible for small-sized robots. Recently, intrinsic properties of the robot have also been used for self-sensing. The shape of a dielectric actuated elastomer [61] is related to its capacitance values, and measuring the voltage and the current value can help to derive external force from the change in the shape accordingly. The signals provided to the pneumatic chamber is another useful information, acoustic or pressure signal can be collected to estimate the robot shape [29, 137]. While the overall shape is known, the effect from the external force is hard to be evaluated separately from the actuation inputs. In recent decades, the development of flexible electronics paves a way of compact and soft internal sensors for soft robots. Flexible and conductive materials, like eGaIn (eutectic gallium indium, a liquid alloy) [138, 139] and ionic solution [140], can be integrated into soft non-conductive silicone to form compliant skin sensors, which are employed to sense the stress in MIS [141], strain [142], and shape [41] for robots.

In addition to sensors, establishing a proper model of the continuum robot is

also essential for control and force estimation. Piecewise constant curvature approximation [143] regards the shape of a single continuum robot as an arch, which is determined by the length of each actuation chamber, but the direction angle and the bending angle of the PCC model are jointly affected by actuators and the external forces. The other stream of modelling is to assume a flexible manipulator as an Euler-Bernoulli beam [144] or a Kirchhoff elastic rod [145]. Therefore, the kinematics can be obtained by solving the displacement of robot's backbone with all the acting forces, but an UEF can act at any position and any direction. In the velocity domain, Jacobian matrix maps between the velocities of actuators and the end effector [146], so that in a short interval, the position change of the tip can be solved using the change of actuation configuration. Analytical models are problematic in an unstructured environment due to the uncertainty of the UEF. Thus, models considering the environmental information are likely to achieve higher precision so that machine learning [147] and fuzzy control models [91] were investigated. Building machine learning models is time-consuming and the environmental information in model training is often static, which is not consistent with dynamic UEF, and fuzzy control methods aim to bring the robot tip to a desired position which may not be attainable in some applications. Thereby, accurately estimating the UEF faced by soft robots not only benefits handlers but also contributes to building better control schemes. For instance, in [61], a feedback control scheme was proposed based on the estimated force. The shape of an elastomer was modelled by the actuation force and the external force, so that the system can intelligently avoid obstacles and adjust the controller outputs. In [148], contact detection was realized along a pneumatic-driven flexible manipulator. Similar to kinematics, estimating the UEF can be an inverse process when the manipulator is assumed as a Cosserat Rod [149], where the actuation configuration and the robot shape were both known. Nevertheless, existing works only considered the force applied at the tip, or sense the deformation type of the robot caused by an EF [150]. The essential difficulty of estimating the UEF has

twofold: 1) UEF can fall into any position along the manipulator, and 2) the direction of the UEF at an action point has three components (x, y, z), thus, its magnitude varies irregularly. To find the location of the force acting arbitrarily on the body, Qiao *et al.* [151] and Venkiteswaran *et al.* [152] combined FBG signals with Cosserat model and Pseudo Rigid Body model, respectively, to solve the position information. However, these approaches are computationally intensive. Alternatively, an array of force sensors can be wrapped along the surface of the continuum robot. This method, however, requires many sensors in order to cover the entire surface. The prevalence of Deep Learning provides a novel method [79]; for example, in [73, 153], a *Deep-Table* frame and RNN model were respectively applied to estimate loads on a robot arm and to estimate hard inclusions of soft tissue. Most of existing works just focused on some specific small areas of the elastomer in estimating the UEF, or only the posture of the soft robot [154], and the motion of the robot is only two-dimension [155].

In contrast, this chapter aims to find the external force acting on the circumferential body of a soft manipulator, including the acting position and the magnitude. That is a relatively larger area and the information of the estimated EF is more complete. The contribution includes:

1) A liquid metal made soft sensor was integrated into a soft manipulator and the signal was extracted to act as bending sensor.

2) The surface of the robot was considered as a 2D map with multiple grids, and a probability approach was used to find the likelihood of the column position.

3) The row position of the 2D map and the corresponding magnitude were estimated by virtual work principle and regularization algorithm.

4.2 System Setup and Configuration

In order to validate our methodology experimentally, a continuum robot system with one segment was first built. It includes the fabrication of a soft manipulator and the method to embed an internal sensor. The manipulator was also driven by

pressurized air.

Silicone molding technology was employed to fabricate the soft manipulator, and the fabrication procedures are illustrated in Fig. 4.1 (a). Silicone rubber (E605, Hong Yejie, Shenzhen, China) was poured into a 3D-printed mold (Fig. 4.1 (a)-(I)) to form the inner component of the manipulator, which was then wrapped by a Nylon thread to limit the radial expansion once the chambers are pressurized. Two helical grooves were designed in the mold, preventing the wrapped threads from slipping during the operation (Fig. 4.1 (a)-(II)). Next, the inner component was secured by two disks at the two ends, and three insulated thin silicone tubes (OD:1mm, ID:0.5mm), which serve as the channels for eGaIn, were connected to the two disks (Fig. 4.1 (a)-(III)). Then, the entire component was placed into another mold to form the outer layer (Fig. 4.1 (a)-(IV)). After demolding, an outer layer surface consisting of twenty concave faces (4 columns and 5 rows) along the manipulator were obtained. Then, eGaIn was injected into the three thin tubes (Fig. 4.1 (a)-(V)), where the elongation of the tube will simultaneously decrease its cross-sectional area, such that the electronic-resistance change of eGaIn sensors ($R = \rho\frac{l}{S}$) can reflect the deformation of the manipulator. The three sensors are connected in series and a constant current power source of 1A is then supplied, as Fig. 4.1 (c) shows. The voltage difference across each sensor is measured via an oscilloscope (Tektronik TBS 1064), which converts the resistance change into voltage signal. Finally, three supporting steel bars (marked in blue in Fig. 4.1 (a)) that are located 120° apart were removed, providing the space as the chambers for actuation. Two rings were then glued at the two ends, allowing a marker to be placed at the top for tip position evaluation and mounting at the bottom (Fig. 4.1 (a)-(V)). The region that an UEF is likely to present along the circumferential body can be indexed by the column and the row numbers radially. A schematic view of the circumferential surface is shown in Fig. 4.1 (d)-(right), and the problem lies in accurately finding the two positions to pinpoint the external force and then to estimate its magnitude, with an assumption that the UEF is always pointing

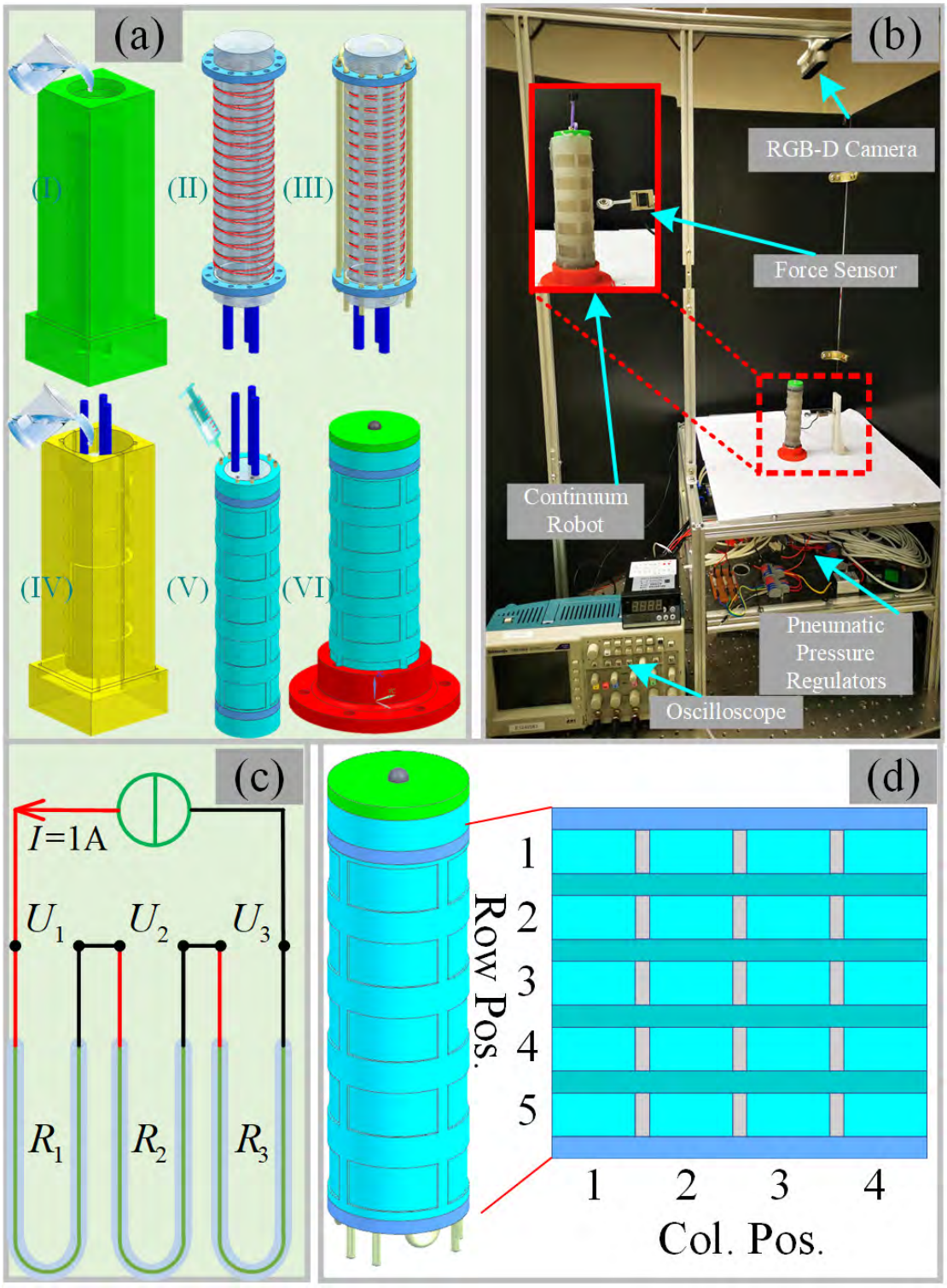

Fig. 4.1. (a) Fabrication of the manipulator. (b) System setup. (c) Circuit of electronic resistance measurement. (d) Schematic view of the circumferential view of the soft manipulator.

towards the backbone of the manipulator.

To actuate this soft manipulator, the three chambers were connected to three pneumatic pressure regulators (ITV-0030, SMC), and the pressurized air can be controlled at an accuracy of 0.01 bar. The manipulator was mounted vertically in an aluminium frame, and a calibrated RGB-D camera (Realsense D415, Intel) was set up at the top of the frame to sample the true position at the tip, as illustrated in Fig. 4.1 (b). A single-axis force sensor (ZNLBS-VII, Zhongnuochuanli, Bengbu, Anhui, China, range: $[-5, 5]N$) was placed next to the manipulator, providing the true external force magnitude for validation. A control interface was developed using MATLAB 2019b.

4.3 UEF Estimation

The tip position is the combined result from the actuation inputs and the external force, as shown in Fig. 4.3 (a), where the shape of the manipulator at step k can be deemed as an arch defined by three parameters: the direction angle ψ_k, the bending angle θ_k and the bending radius R_k. All of them can be solved via

$$\psi_k = \text{atan2}(y_k, x_x), \theta_k = 2\text{acos}(\frac{z_k}{\sqrt{x_k^2+y_k^2+z_k^2}}), R_k = l/\theta_k \ , \tag{4.1}$$

if the tip position $P_k(x_k, y_k, z_k)$ is obtained. Since the three eGaIn sensors are mounted adjacent to the three chambers respectively, the sensor readings directly correlate with the chamber length, so that the real-time tip position both in load-free and load conditions can be computed based on the sensor readings S_k. Namely, the true tip position P_k can be mapped between S_k.

In load-free condition, the tip position can be regarded as solely depending on actuation inputs A_k, which means that the tip position $P_k|_{free}$ can be solved just using A_k. In contrast, as Fig. 4.3 (b) shows, an external force $F_{e,k}$ causes the true tip position P_k to deviate from the theoretical load-free value $P_k|_{free}$. When the external load is present, the position deviation $\Delta P_k = P_k - P_k|_{free}$ in the tip position is large due to $F_{e,k}$. Therefore, by knowing the current actuation inputs A_k, the deviation can imply whether or not $F_{e,k}$ is present.

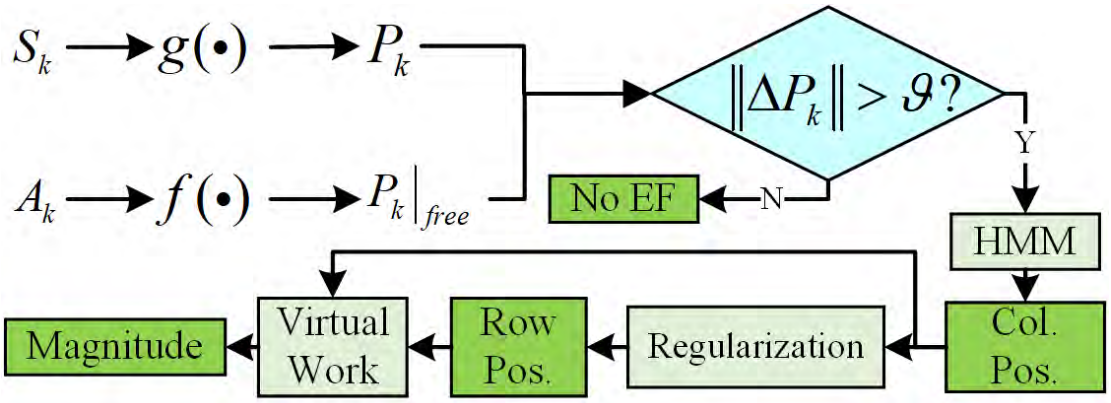

Fig. 4.2. Overall frame of the UEF estimation process.

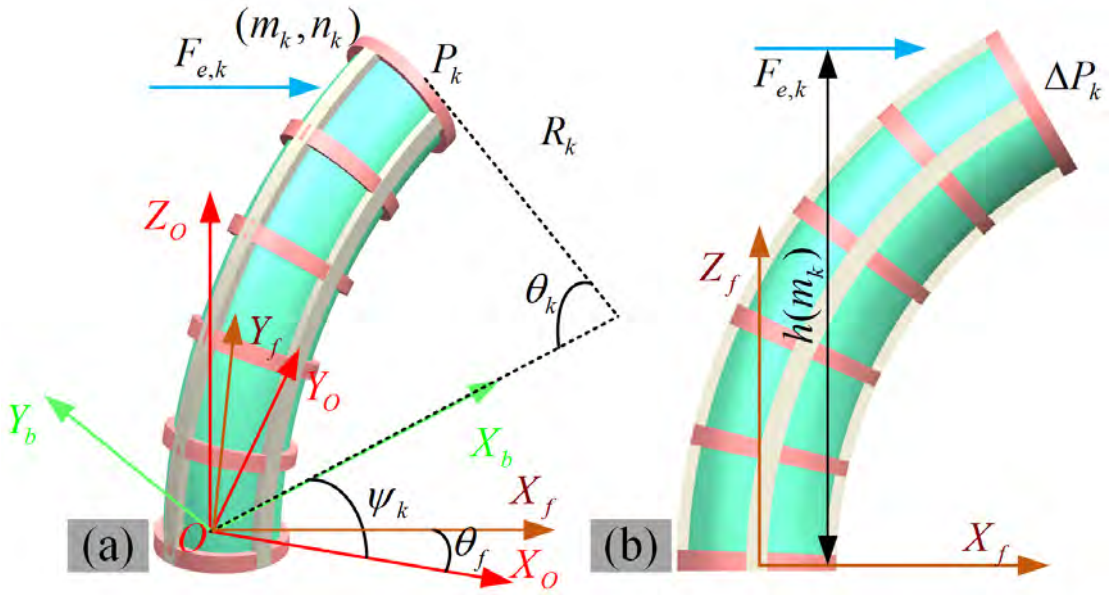

Fig. 4.3. Illustration of deformed flexible arm. (a) Coordinate frames. (b) Tip position in X_fOZ_f only due to an external force.

The evaluation method consists of three parts. First, the models to find $P_k|_{free}$ and P_k are constructed using Neural Network. Then, the column position of an UEF is estimated with HMM. Finally, the row position and the magnitude are calculated using the principle of virtual work. The overall framework is illustrated in Fig. 4.2.

4.3.1 Tip Position Prediction

Sensor readings are highly and directly related to the shape and the tip position, such that a mapping $g(\cdot)$ between P_k and S_k: $P_k(x_k, y_k, z_k) = g(S_k)$ can be built to form a proprioceptive sensing mechanism, both in load and load-free condi-

tions. Fabrication imperfection and uncertainty of the EF increase the difficulty to find an analytical mapping, so using data-driven method to build Neural Network model provides a feasible alternative. Similarly, $P_k|_{free}$ is also solved by considering the actuation inputs, which is $P_k|_{free} = f(A_k)$. Since the input data and the position data do not vary significantly over time, an embedded dimension d was considered to estimate the position using last d records of data, and the two mappings are updated as:

$$\begin{cases} P_k|_{free} = f(A_{k-d:k}) \\ P_k(x_k, y_k, z_k) = g(S_{k-d:k}) \end{cases} . \tag{4.2}$$

Two Multilayer Perceptron (MLP) Neural Networks were respectively constructed to find $f(\cdot)$ and $g(\cdot)$. We set the embedded dimension $d = 5$. The output layer and input layer of the two models has 3 and 15 nodes, respectively, and the activation functions in hidden layer and output layer are 'Sigmoid' ($y = \frac{1}{1+e^{-x}}$) and 'ReLu' ($y = max(0, x)$), respectively. A threshold ϑ is set to account for model error. Through comparing between ΔP_k and ϑ, UEF is detected as:

$$\begin{cases} UEF & \|\Delta P_k\| \geq \vartheta \\ Load\ Free & else \end{cases} . \tag{4.3}$$

4.3.2 Column Position Estimation towards UEF via HMM

After identifying the presence of an UEF, its position can be estimated based on the tip position deviation ΔP_k. As Fig. 4.3 (b) and Fig. 4.1 (d) illustrate, there are 20 regions where an UEF is likely to present, one of which is denoted by (m, n) ($m \in [1, 5], n \in [1, 4]$ are row position and column position, respectively). We firstly solve n_k because it is involved in the deviation direction of the tip position, and the row position m_k as well as the magnitude affects deviation degree (i.e. bending angle). In the robot system, only $A_k, \Delta P_k$, and S_k are known, which refers to observation data, and the column position n_k is hidden. Because of the uncertainty of the EF and slow motion of the robot, the state is only mapped with the current observation data. This satisfies the property of HMM that the observation outcome in current step does not affect the outcome in the previous

step, providing us a technique to estimate the hidden state n_k. The observation sequence $O = (o_1, \cdots, o_k)$ and a well learned HMM λ are employed to find the column position:

$$\hat{n}_k = \underset{1 \le i \le 5}{\arg\max} \Pr(n_k = i | \lambda, O), \tag{4.4}$$

where $\hat{n}_k = 5$ means no UEF, and the observation data o_k depends on the actuation inputs and the position deviation: $o_k^{1\times6} = \{A_k^{1\times3}, \Delta P_k^{1\times3}\}$. To reduce the unit discrepancy, the actuation inputs were normalized with $[0, 1]$ and further expressed as:

$$\begin{aligned} o_k(l)_{1\le l\le3} &= \begin{cases} -1 & A_k(l) \in [0.0, 0.33) \\ 0 & A_k(l) \in [0.34, 0.66) \\ 1 & A_k(l) \in [0.67, 1] \end{cases} \\ o_k(l)_{4\le l\le6} &= \begin{cases} 0 & \|\Delta P_k(l-3)\| \le \xi \\ \mathrm{sgn}(\Delta P_k(l-3)) & else \end{cases} \end{aligned}, \tag{4.5}$$

where $\xi = 3$ mm is a threshold considering the measurement error. The hidden state of our HMM is the column position n_k and the state transition probability between two continuous steps i and j is: $a_{ij} = \Pr(n_{k+1} = j | n_k = i)$. In addition, the emission probability is defined as: $b_j(o_k) = \Pr(o_k | n_k = j)$. As a result, there are possibly in total $N = 3^6$ different observation data, which is difficult to manifest their corresponding emission probability. This issue was previously tackled by multivariate Gaussion distribution [156], requiring a large amount of data to find the mean value and variance. Therefore, K-means algorithm is employed to reduce the dimension of the observation data, and the observation data is classified into one hundred categories (input one observation data with 6 dimensions to get one dimension). The observation data o_k is updated to v_k: ${v_k}^{1\times1} \leftarrow Kmeans({o_k}^{1\times6})$, and the observation sequence O is: $\{v_1, \cdots, v_k\}$.

Initially, the state transition probability is assumed as an uniform distribution, so that the initial probability for each hidden state is $\pi_i = \frac{1}{5}$. Now, this HMM is defined as: $\lambda = \{\pi, a_{ij}, b_j(v_k)\}$. With Bayesian's rule, (4.4) is updated to:

$$\hat{n}_k = \underset{1 \le i \le 5}{\arg\max} \frac{\Pr(n_k = i, O | \lambda)}{\Pr(O | \lambda)}. \tag{4.6}$$

In order to calculate $\Pr(O | \lambda)$, forward and backward probability are defined as:

$$\begin{aligned} \alpha_k(i) &= \Pr(v_1, \cdots v_k, n_k = i | \lambda) \\ \beta_k(i) &= \Pr(v_k, \cdots, v_T | , n_k = i, \lambda) \end{aligned}. \tag{4.7}$$

so $\Pr(O|\,\lambda)$ can be further calculated by:

$$\Pr(O|\,\lambda) = \sum_{i=1}^{5}\sum_{j=1}^{5} \alpha_k(i) a_{ij} b_j(v_{t+1}) \beta_{t+1}(j). \tag{4.8}$$

Let $\gamma_k(i)$ denotes the probability of hidden state i with knowing λ and O at step k, and $\xi_k(i,j)$ represents the probability of hidden state j at step $(k+1)$ if the hidden state is i at step k, both of which are then denoted as:

$$\begin{aligned} \gamma_k(i) &= \Pr(n_k = i|\,O,\lambda) = \frac{\alpha_k(i)\beta_k(j)}{\sum_{j=1}^{5}\alpha_k(i)\beta_k(j)} \\ \xi_k(i,j) &= \Pr(n_k = i, n_{k+1} = j|\,O,\lambda) \\ &= \frac{\alpha_k(i)a_{ij}b_j(o_{k+1})\beta_{k+1}(j)}{\sum_{i=1}^{5}\sum_{j=1}^{5}\alpha_k(i)a_{ij}b_j(o_{t+1})\beta_{t+1}(j)} \end{aligned} . \tag{4.9}$$

To obtain a well-learned HMM model, T sets of data including the observation data and the column position are collected, and the Baum-Welch algorithm is employed. Finally, the parameters of λ are learned via:

$$a_{ij}^{n+1} = \frac{\sum_{k=1}^{T-1}\xi_k(i,j)}{\sum_{k=1}^{T-1}\gamma_k(i,j)}, b_j(k)^{n+1} = \frac{\sum_{k=1,o_k=v_k}^{T}\gamma_k(j)}{\sum_{k=1}^{T}\gamma_k(j)}. \tag{4.10}$$

The initial probability is $\pi_i^{n+1} = \gamma_1(j)$. After iterations, we can get:

$$\lambda^{(n+1)} = \{\pi^{(n+1)}, a_{ij}^{(n+1)}, b_j^{(n+1)}(n_k)\}, \tag{4.11}$$

so the estimated column position at step k is:

$$\hat{n}_k = \arg\max_{1\le i\le 5}[\gamma_k(i)]. \tag{4.12}$$

4.3.3 Row Position and Magnitude Estimation

After estimating the column position of a single EF ($\hat{n}_k \neq 5$), the algorithm still needs to find the row position m_k, which is related to the moment that the robot is experiencing. The robot can reach a static equilibrium with a tip position after all the acting forces are in balance, and the equilibrium can be established by virtual work principle as:

$$\delta W = \delta W_g + \delta W_{el} + \delta W_{ac} + \delta W_e = 0, \tag{4.13}$$

where δW_g, δW_{el}, δW_{ac} and δW_e respectively denote the virtual work of gravity, elastic force from the robot itself, the actuators, and the external force. The centroid C_k locates at the center of the robot backbone, as calculated by:

$$C_k = \frac{l}{\theta_k}\left[\ (1-\cos\tfrac{\theta_k}{2})\cos\psi_k, (1-\cos\tfrac{\theta_k}{2})\sin\psi_k, \sin\tfrac{\theta_k}{2}\ \right]^T, \tag{4.14}$$

so $\delta W_g = G \cdot \delta C_k(3)$. The length of each chamber is solved using

$$\begin{array}{l} l_{k,1} = l(1-(\theta_k/l)r\cos(\psi_k)) \\ l_{k,2} = l(1-(\theta_k/l)r\cos(\psi_k+\frac{2}{3}\pi)) \\ l_{k,3} = l(1-(\theta_k/l)r\cos(\psi_k+\frac{4}{3}\pi)) \end{array}, \tag{4.15}$$

and the elongation of each chamber is: $\Delta l_{k,i} = l_{k,i} - l$. Therefore, δW_{el} can be calculated by: $\delta W_{el} = \sum_{i=1}^{3} \frac{1}{3} EI \Delta l_{k,i}^2$, where E is the Young's Modulus and I is the inertial moment. Similarly, the virtual work of the actuators is the accumulation of the three chambers: $\delta W_{ac} = \sum_{i=1}^{3} A_k(i)\pi {r_c}^2 \Delta l_{k,i}$ (r_c is the radius of the chamber). All virtual work can be expressed as functions in term of bending angle θ_k. The external force can be present in any position of the 20 areas, so $\delta W_e = F_e \delta_e$, where δ_e is involved in $\delta\theta_k$ and the row position $\hat{m}_k$. Although all of them can be solved, (4.13) includes both the magnitude and the row position of an external force. It would be difficult to evaluate them simultaneously. Considering that the tip position deviation is purely caused by the external force, we can use ΔP_k to establish another mapping: $\Delta P_k \leftarrow (F_{e,k}, m_k)$.

The flexible manipulator is assumed as a system and the tip position P_k reflects its system response influenced by the external force and the actuation inputs, which is expressed as:

$$P_k = H(A_k)A_k + H_e(m_k)F_{e,k} + Q, \tag{4.16}$$

where $H(A_k) \in R^{3\times 3}$ is a system matrix relating between the tip position (system response) and the actuator inputs (i.e. $f(\cdot)$), and $H_e(m_k)$ is a matrix involved in the position of the external force $F_{e,k}$. The tip position change caused by an UEF at a certain row position, namely $H_e(m_k)F_{e,k}$, is calculated by

$$\begin{array}{l} H_e(m_k)F_{e,k} = rotz(\theta_f)\begin{bmatrix} \frac{F_{e,k}h(m_k)^2(3l-h(m_k))}{6EI} \\ 0 \\ \frac{2EIl}{F_{e,k}h(m_k)^2}\sin(\frac{F_{e,k}h(m_k)^2}{2EI}) \end{bmatrix}, \\ \theta_f = \frac{2\hat{n}_k-1}{4}\pi(\hat{n}_k \neq 5) \end{array} \tag{4.17}$$

where $rotz(\theta_f)$ denotes a rotation matrix around Z axis to θ_f, as shown in Fig. 4.3, and θ_f is involved in the estimated column position. Since we have found the column position in the previous section, only m_k and $F_{e,k}$ are unknown in this equation. Q is the Gaussian white noise indicating the systematic error. $H(A_k)A_k$ denotes the pure systematic response from the actuators, so (4.16) is updated as:

$$\Delta P_k = H_e(m_k)F_{e,k} + Q. \tag{4.18}$$

ΔP_k is the pure systematic response due to $F_{e,k}$. Therefore, the row position of $F_{e,k}$ can be solved by:

$$\hat{m}_k = \arg\min_{m_k} \|\Delta P_k - H_e(m_k)F_{e,k}\|_2^2 . \tag{4.19}$$

However, finding the optimal solution is not easy with many local minima. Since the equation may not yield to the global minima due to the noise and local minima, a regularization factor is also added to the equation to ensure convergence:

$$\arg\min_{m_k}(\sqrt{\|\Delta P_k - H_e(m_k)F_{e,k}\|_2^2} + \chi\sqrt{\|F_{e,k}\|_2^2}), \tag{4.20}$$

where χ is a regularization parameter. After finding the row position m_k, the magnitude of the external force can be accordingly solved via (4.18). However, the value of χ is really important for the results, and setting a proper χ requires delicate calculation. We employ gradient descent algorithm to set different values of χ to address the issue. In virtual work principle, the ideal value of δW is close to zero, but an improper χ may lead to a large error in $\delta W(\chi)$. As a result, an iteration process was employed to update χ such that $\delta W(\chi)$ can converge to an value within an user-defined threshold ς: $\widehat{\chi} = \chi - \eta\delta W(\chi)$, where η is the learning rate. When the algorithm finds the most possible position of the external force with different χ, the magnitude can also be calculated through (4.18).

4.4 Experimental Validation

Experiments were conducted to test the performance of the sensors and each module of the algorithm.

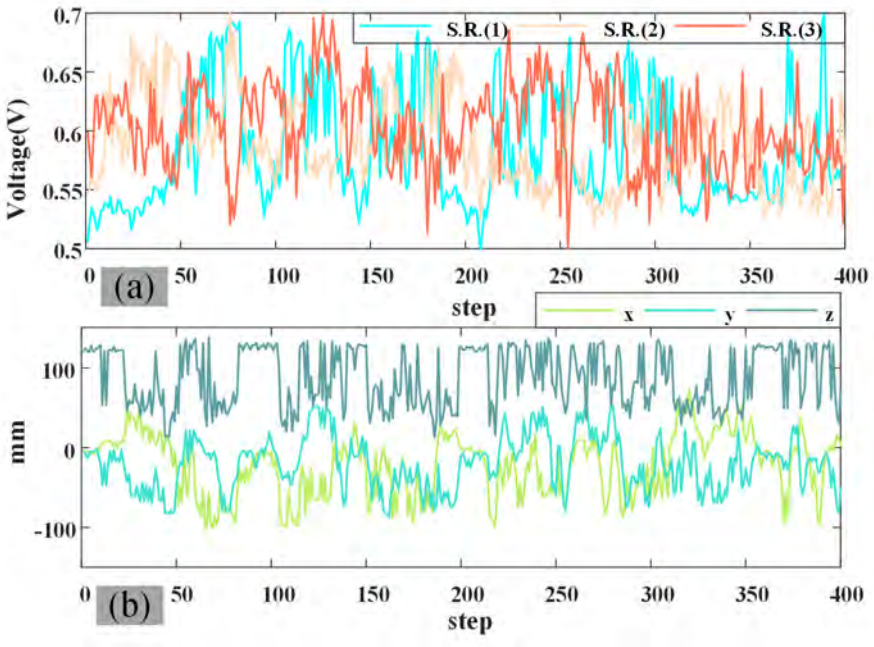

Fig. 4.4. Fundamental test about the experimental setup. The soft manipulator was commanded to explore the task space randomly. The sensor readings and the tip position were simultaneously collected. (a) Sensor readings. (b) (x, y, z) of the tip position in task space.

4.4.1 Sensor Performance

Robot was commanded to explore its task space by randomly setting the air pressure of each chamber for 2000 times in load-free condition, where the pressure was increased or decreased 0.05 bar, or kept unchanged between steps, and the tip varied continuously. After the robot became stable after each step, the sensor readings were collected ten times to store their mean value. Fig. 4.4 shows 400 sets of data, indicating the sensors are capable of outputting different values based on the shape of the robot. The data was also used to train the two tip position sensing models. The sensors are further examined about robustness and temperature-resistance ability.

1) Robustness

First, only one chamber was actuated in load-free state for ten times using the same actuation inputs: varied from 0 to 0.6 bar with an increment of 0.05 bar (13 actuation inputs in total, in room temperature $25°C$), and the eGaIn sensor beside the chamber directly detected the length change. The whole data collection was

conducted five times, and Fig. 4.5 (a) shows the variation of the sensor reading, from which the maximum variance with 0.016 V appears at 0.4 bar. This indicates the robustness of the sensor and can clearly map with the shape change of the robot.

2) Performance in different temperatures

The value of electric resistance corresponds with the ambient temperature accordingly, so the performance of the sensors in higher temperature environment was tested. The manipulator was heat in an oven with $45°C$ for one hour, and remount back to the platform for another testing. Using the same actuation inputs, we obtained similar sensor readings data, as shown in Fig. 4.5 (a). The data is almost similar to that obtained in $25°C$, showing the eGaIn can work robustly in common temperature range.

3) Comparison with strain gauge

To further validate the performance of the eGaIn sensor, a commercial strain gauge (BF-350-6AA) was used for comparison. As Fig. 4.5 (b) shows, an a cantilever-like silicon elastomer was fabricated and the eGaIn was integrated on the top to measure the bending strain. Since the bending would exceed the operating range of the strain gauge, a miniature flexible protective housing (made of TPU) was used to provide a scaling effect on the bending strain as experienced by the strain gauge. The housing was adhered to the elastomer and the strain gauge was mounted on the top surface of the housing, allowing the strain gauge to experience a scaled tensile or compressive strain as the eGaIn to avoid damage. The pressure for actuating the elastomer was increased from 0 to 0.21 bar at an increment of 0.03 bar, and the sensor readings at each deformation were collected 10 times. Fig. 4.5 (c) shows the comparison between the two sensors. Both sensor readings demonstrate that as the bending increases, the voltage output increases as well, indicating an increase in the sensor's resistance value. From the results, the variance of the strain gauge is slightly larger than the eGaIn sensor, indicating that strain gauge is subject to more fluctuation due to the environment.

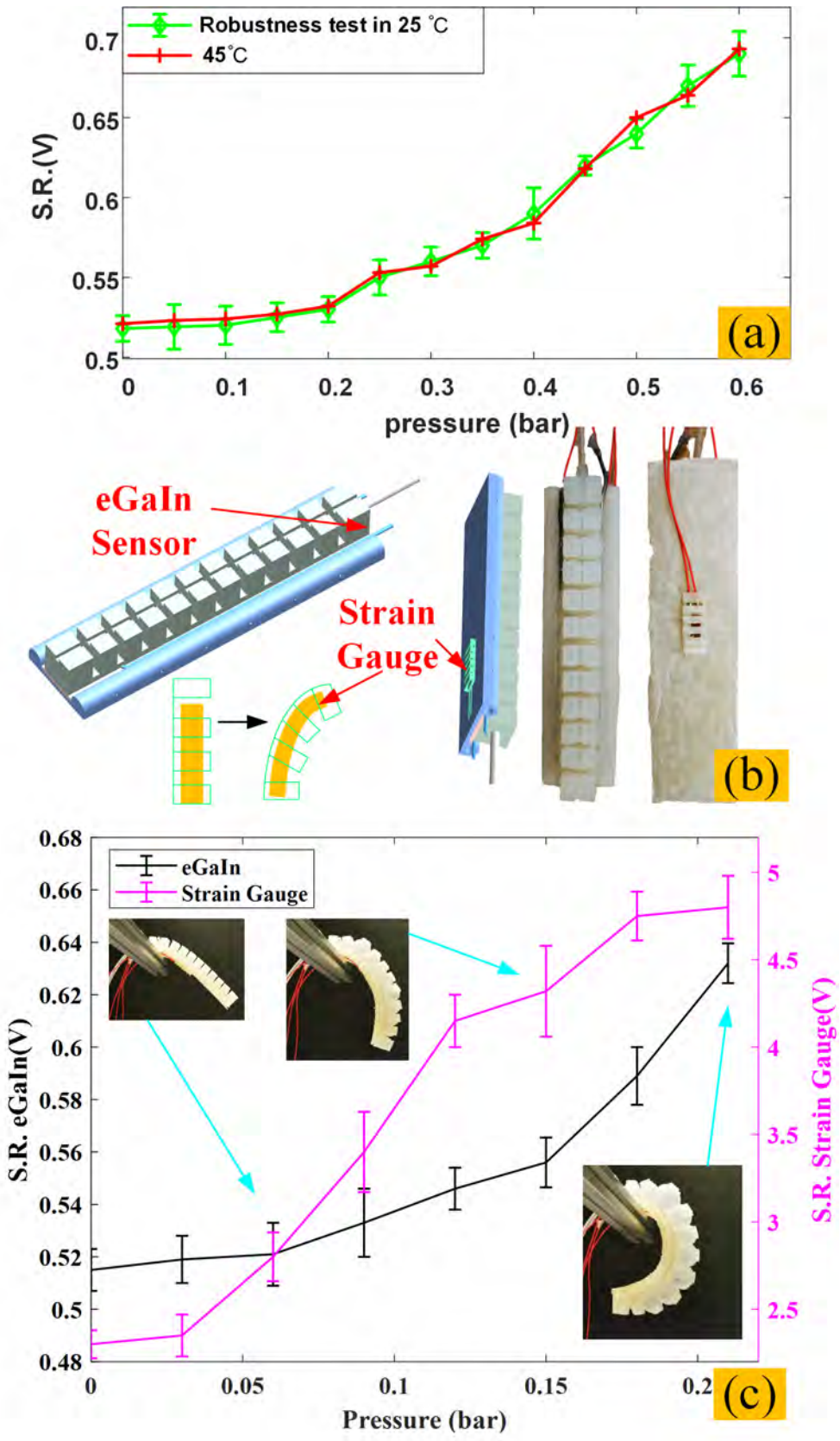

Fig. 4.5. (a) Performance of robustness and in different temperature. (b) Experimental setup for comparing the sensor and commercial strain gauge. (c) Results between the eGaIn sensor and the strain gauge.

Table 4.1: Data and results for the tip position sensing models ('Y': use the data, and 'N': not use.)

	Training data		
	load free 2000 sets	20g weight at tip 1000 sets	20g weight at mid. 1000 sets
$f(\cdot)$	Y	N	N
$g(\cdot)$	Y	Y	Y
	Testing data (max. err./ mean err. unit: mm)		
	load free 100 sets	dual 20g weight (tip. and mid.) 100 sets	30g weight at tip 100 sets
$f(\cdot)$	Y (3.98/3.19)	N	N
$g(\cdot)$	Y (3.87/3.26)	Y (3.94/3.31)	Y (4.13/3.45)

4.4.2 Results of Tip Position Proprioceptive Mechanism

The position deviation ΔP_k is one important input data for HMM, so its accuracy is highly involved in the UEF estimation result. To train $f(\cdot)$, the data collected in Section-4.4.1 (load-free condition) was used. To mimic the robot operation under a load (i.e. with EF), a weight with $20g$ was hung at the robot tip and at the middle part, and random actuation inputs were commanded to robot to reach another 1000 new positions, respectively. The true tip position was collected using the RGB-D camera. The data for training and testing the two models is listed in TABLE 4.1. In training, the maximum iteration in each model was set to 1000, and the learning rate was 0.1.

In terms of validation, one hundred new data of random actuation inputs were commanded to the robot in load-free condition, covering almost the entire task space of the tip. The ground truth was also collected by the RGB-D camera for comparison. Fig. 4.6 (a) shows the comparison between the actual tip position and the values predicted by $f(\cdot)$ in load-free condition. The maximum error between the predicted and the actual values in all the 100 steps is 3.98mm, while the mean position error is 3.19mm.

To test the performance of $g(\cdot)$, in addition to the new 100 data for $f(\cdot)$, 100 sets of data with two $20g$ loads at the tip and in the middle, and 100 sets of data with a $30g$ weight at the tip were considered, as listed in TABLE 4.1-Testing

Table 4.2: Predicted tip position under the same actuation inputs (up: $P_k|_{free}$, mid: P_k, bottom: ΔP_k, unit: mm).

Act. Inputs (bar)	load free	dual 20g weights	30g weight at tip.
(0.1,0.2,0.5)	(19.7,-2.9,150.7) (20.8,-3.4,151.6) 1.5	(19.7,-2.9,150.7) (40.4,92.2,83.5) 118.3	(19.7,-2.9,150.7) (34.5,-84.1,100.2) 96.8
(0.4,0.4,0)	(-45.4,29.9,88.5) (-46.6,30.2,89.2) 1.4	(-45.4,29.9,88.5) (-74.1,-35.5,132.6) 83.9	(-45.4,29.9,88.5) (-64.7,16.5,147.8) 63.8
(0.6,0.2,0.3)	(-101.8,42.8,102.7) (-102.3,43.6,104.8) 2.4	(-101.8,42.8,102.7) (-108.4,-58.7,56.6) 111.6	(-101.8,42.75,102.7) (-122.2,21.1,67.2) 46.3

data. The multi-load case was not included in the training data, and the results demonstrate the predicted tip position is generally accurate compared with the ground truth. The position value on each axis for the 100 data (two $20g$ weights) is plotted in Fig. 4.2. As Fig. 4.2 (a) shows, $f(\cdot)$ can properly predict the tip in load-free scenario, and no significant error was observed as compared with the measurement from RGB-D. Similarly, even with the unseen multiple loads, $g(\cdot)$ can also properly predict the tip, as shown in Fig. 4.2 (b). To ensure that ΔP_k can effectively detect the presence of UEF in all three scenarios: no load, load at the tip, and multiple loads, three random actuation inputs were selected and the predicted from $f(\cdot)$ and $g(\cdot)$ under the three scenarios are summarized in TABLE 4.2. Results confirm that ΔP_k is small when there is no load and is large in the presence of loads. Based on the results, the threshold ϑ used to determine the force for ΔP_k was set to $5mm$.

4.4.3 Testing on Column Position Estimation

The above experiments validated the performance of the sensors and the mechanism to sense the presence of an UEF. Once the force is detected, HMM can be employed to find the column position accordingly. To examine the model, 500 sets of data were first prepared for training and another 100 sets were prepared for validation. The robot was randomly moved to a new location, and a metal bar

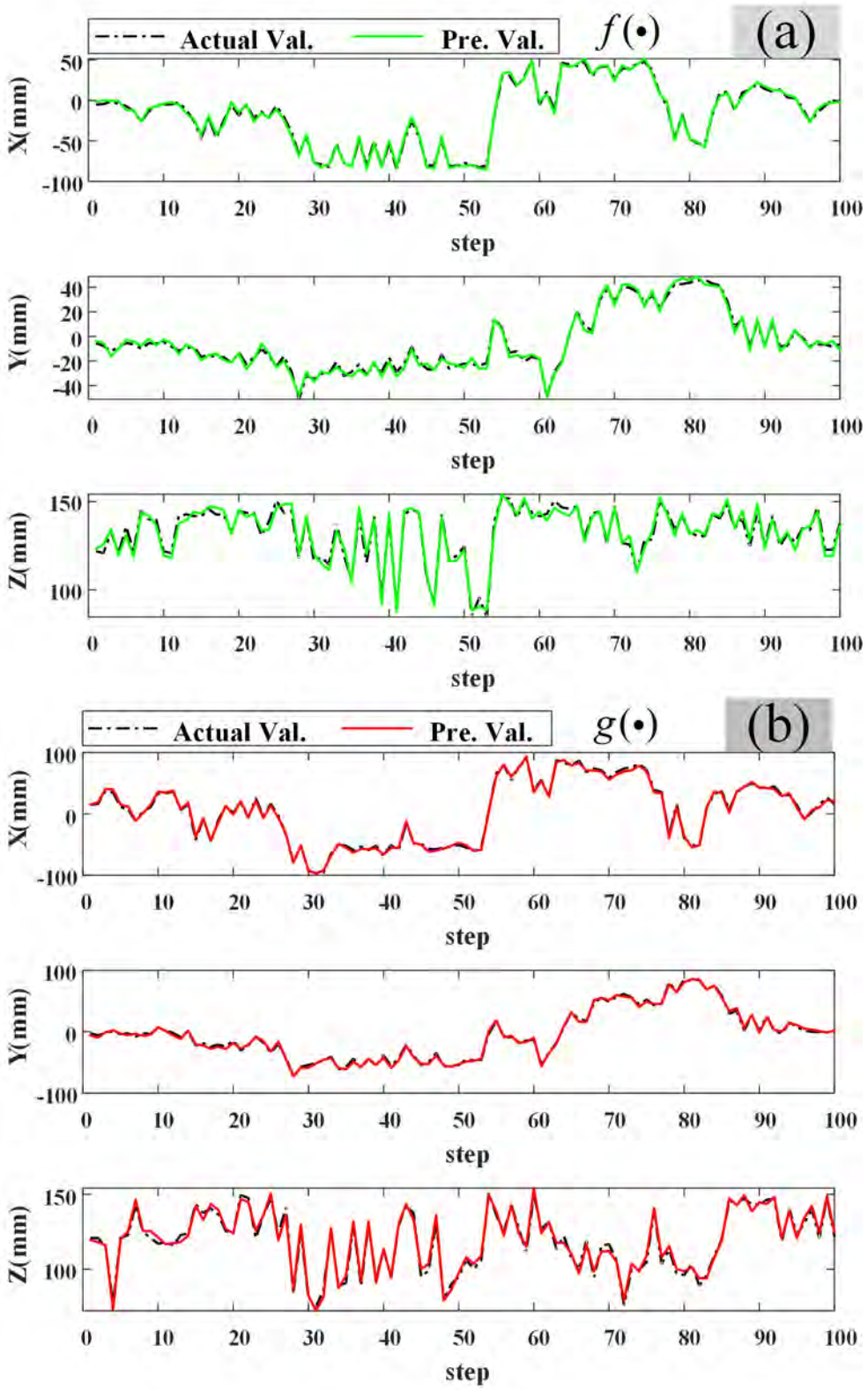

Fig. 4.6. Validation towards $f(\cdot)$ and $g(\cdot)$. (a) load-free testing. (b) load ($20g$ weight was added to mimic static external force) condition testing.

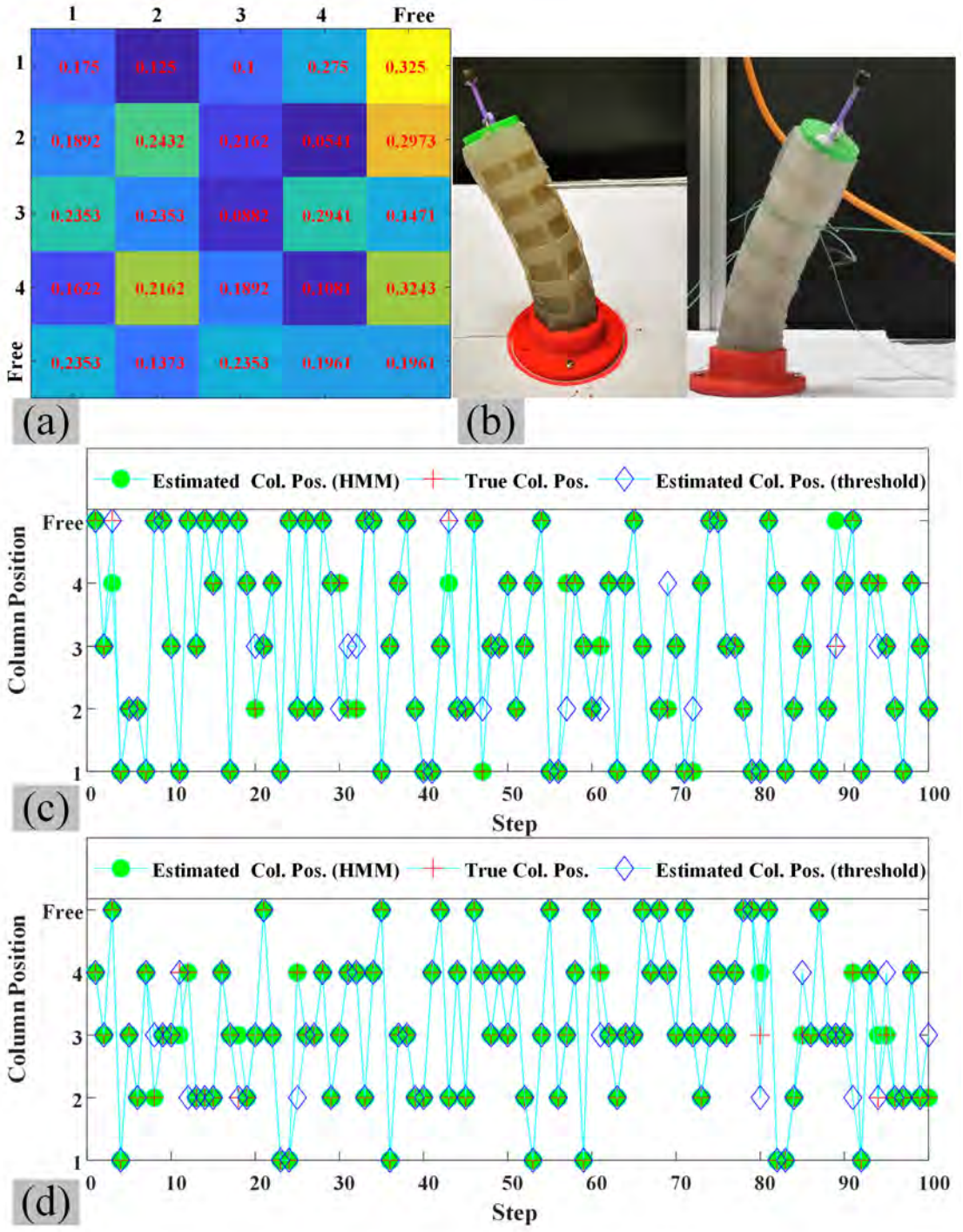

Fig. 4.7. (a) State transition probability. (b) Snapshots robot experiencing different EF. (c) and (d) Column position estimation results when robot was excited by a bar (pushing force) and thread (tension), respectively.

was used to poke on the surface and exerted a force onto the robot. The location where the bar poked at (i.e. the column and row positions) was randomly selected. At some steps, no force was exerted onto the robot to also include the no-load case to the data. The learned state transition probability matrix is illustrated in Fig. 4.7 (a). Validation using the 100 sets of data is summarized in Fig. 4.7 (c). It can be observed that HMM can predict the column position properly and only three of the estimated results (the 4th, 42th and 88th) did not match, reaching an accuracy of 97% . To better show the accuracy of the model, a simpler prediction method, inspired by [157], to predict the force direction, which is based on the change in tip position (x, y) due to the force, was considered for comparison, and the algorithm is listed as:

$$\hat{n}_k = \begin{cases} 1 & \Delta P_k(1) < 0, \Delta P_k(2) < 0 \\ 2 & \Delta P_k(1) > 0, \Delta P_k(2) < 0 \\ 3 & \Delta P_k(1) > 0, \Delta P_k(2) > 0 \\ 4 & \Delta P_k(1) < 0, \Delta P_k(2) > 0 \\ free & \|\Delta P_k\| < \vartheta \end{cases} . \tag{4.21}$$

The results of this method is also shown in Fig. 4.7 (c)(threshold). While the column position can still be predicted, but the accuracy is only 90%. In addition, this simpler prediction method can only work with 4 quadrants, and the HMM method is needed for higher column resolution.

In addition to pushing force, tension was also considered to test the trained HMM. Four threads were secured to the surface of robot to generate pulling force at the four columns, as shown in Fig. 4.7 (b)-(Right). 100 sets of random actuation inputs and random pulling were prepared and the results are shown in Fig. 4.7 (d). Both HMM and the simpler prediction methods can still predict the column position, the accuracy using HMM (96%) remains higher than the simple method (91%).

4.4.4 Estimating the Row Position and UEF Magnitude

TABLE 4.3 lists the material properties of the robot that are required for estimating the row position and the magnitude. Since the algorithm uses an iterative

Table 4.3: Material properties

Property		Value	Property		Value
E	Young's Modulus	2.7 MPa	r_c	Chamber Radius	2 mm
ρ	Density	1.07 (g/cm^3)	l	Backbone Length	120 mm
r	Distribution Radius	13 mm	G	Gravity	0.86 N

approach to find the optimal values and the model was built assuming the robot is in balance, the system starts to estimate the row position and magnitude 1s after setting an actuation input (robot is stable). The parameter χ is set to 1 and the maximum iteration epoch is 10. In addition, the mean value and the variance of the Gaussian white noise in (4.18) were set to 0 and 5, respectively. In testing, the two hundred sets of actuation inputs were commanded to robot and the bar always excited the robot ensuring $\|\Delta P_k\| \geq \vartheta$ (EF always acts). The final estimated row positions and the true ones are illustrated in Fig. 4.8 (a), proving that only 3 (67th, 148th, and 172th) estimated positions failed to meet with the true results, reaching an accuracy of 98.5%.

In terms of validating the magnitude estimation method, the force sensor was mounted at different positions, as Fig. 4.8 (c) shows, which means the position and magnitude of the external force were both known, and then robot was commanded to touch the force sensor, whose output was regarded as the ground truth for validation. The force sensor was fixed beside the four columns of the manipulator, and different actuation inputs were set to command the manipulator to contact the force sensor while the row position was also changed at each column position by manually adjusting the height of the force sensor. In this way, sixteen regions on the manipulator surface were tested by the force sensor, and three actuation inputs were considered for each region to set different magnitudes. The row position calculation was based on the results from the column position estimation, which means θ_f can be obtained for further calculation. The estimated results are illustrated in Fig. 4.8 (b). During all the 48 steps, only two (23th and 41th) estimated positions were deviated from the true value, which mainly results from the inaccurate row position. As for the magnitude, a maximum force

of $2N$ was applied for testing, and the maximum error happened on the inaccurate step is $0.71N$ which is caused by the inaccurate estimation of the row position. Other than that, the mean error of the estimated magnitude in other 46 steps is $0.23N$, showing this estimation method combining virtual work principle and regularization algorithm is effective.

The time consumption in estimating the presence of an EF (Machine Learning), finding the column position (HMM), and solving the row position and the magnitude (virtual work principle) are 0.078s, 0.008s, and 0.85s, respectively. The third item is more time-consuming due to the iteration process and the process started after the robot was stable, which would take a longer time. The first and the second items took less time and they can be evaluated in real-time. In addition, the probability model requires fewer data in training.

4.5 Chapter Summary

Finding the external force acting on a soft robot is important in the field. While majority of work focused on the effect at the end-effector, this paper presents a new method to estimate an unknown force acting on the body of a continuum robot. The robot was fabricated with integrated eGaIn sensors to provide useful information related to the shape of the robot. This proprioceptive sensing mechanism can eliminate the use of common external measurement devices, allowing the robot to operate in a confined and occluded environment. A model-free approach based on Artificial Neural Network was employed to predict the tip position based on the sensor information, and compared with the tip position under a load-free scenario so that the presence of an external force can then be determined. To find the exact location of the force, the circumferential body of the robot was represented by a 2D map, and the indices of the map were evaluated accordingly. HMM was employed to find the column position, and the principle of virtual work with a regularization term was used to find the row position and the magnitude. Experimental results confirmed that the model-free approach can predict the tip position

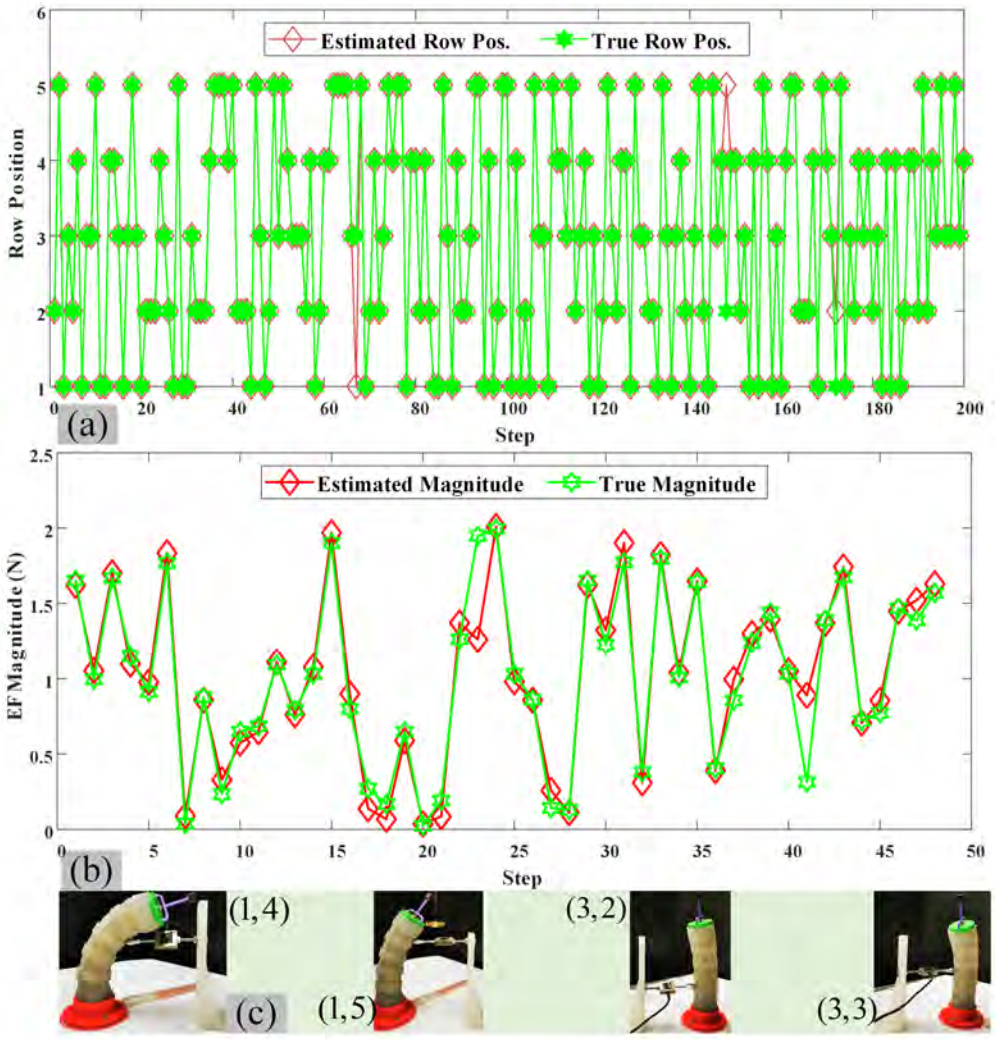

Fig. 4.8. (a) Row position estimation results. (b) True magnitude and the estimated value. (c) Snapshots of robot disturbed by the force sensor at different area (column position, row position).

with an error of about $4mm$. Different scenarios, including different weights of load, multiple loads, and load-free were examined to ensure the robustness of the prediction method. Random force was exerted onto the robot and this algorithm can achieve an accuracy of 97% and 98.5% in finding the column and row positions, respectively. The error in finding the force magnitude is $0.23N$. This proprioceptive sensing and evaluation algorithms enable the robot to easily sense the force information, allowing better interaction with the surrounding environment.

Chapter 5

Dual-Segment Manipulator with Continuous Rotational Motion along the Backbone

5.1 Motivation

Since the concept of continuum robot was first matured in 1990s [7], it has received much interest from researchers and engineers. A continuum robot generally consists of an elastic body actuated by tendon-sheath mechanisms [36, 39], pressurized fluids [25, 54], dielectric elastomer actuators (DEA) [60, 61] or magnetic power [158]. These actuators generate tension or compression force along the axial direction of the chambers distributed radially along the soft manipulator, where the change in length consequently leads to overall deformation of the robot. With the body made of an elastic material, continuum robots exhibit excellent dexterity in task space, high compliance to deal with obstacles, and complicated deformation motion with infinite degree of freedom (DoF). Therefore, they are suitable to work in unstructured environments, such as working in Minimal Invasive Surgery (MIS) with safe touch capability [159, 160], research and rescue in narrow space, and maintenance [161].

The merit of high compliance and safe interaction with human from continuum robots also pose difficulty in designing a robust and accurate controller. The soft body made of low-stiffness materials (e.g. Young's Modulus$< 10^9$pa [162]), can be easily influenced by the external environment. Many existing works simplified

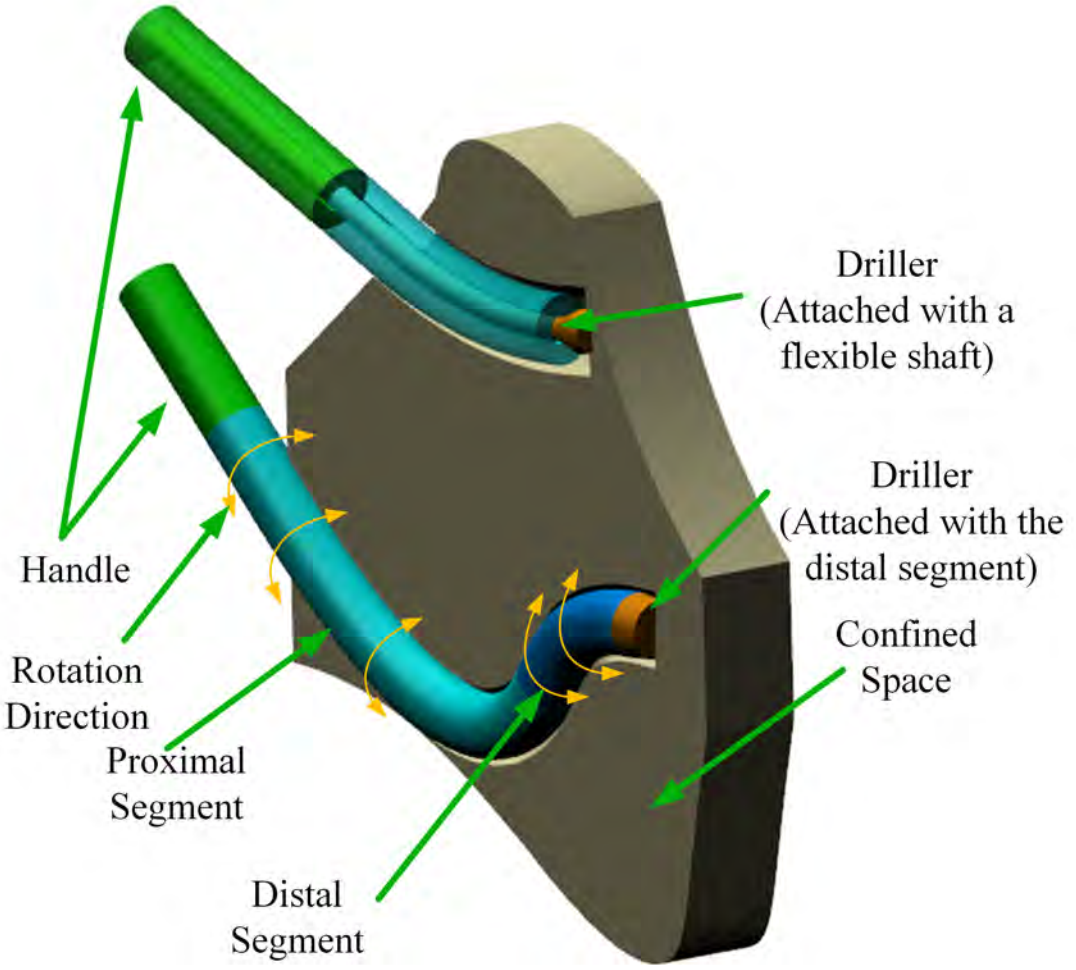

Fig. 5.1. Rotation motion of soft continuum robots in confined environments. (Upper) Existing deformed rotation employs a flexible shaft configured centrally, and the outer soft layer only works for bending. (Bottom) The proposed dual-segment deformed rotation can both bend and rotate along its backbone.

the problem and developed controllers based on kinematic models to bring the robot to a desired pose under quasi-static assumption, which is a tradeoff between motion accuracy and effectiveness.

Additionally, as the soft manipulators are able to deform dexterously, in some scenarios, such as decompressing femoral head osteonecrosis [163], treating pelvic osteolysis [160], visual occlusion avoidance [164], prostate biopsy [165] and drilling holes in a sinuous tunnel (Fig. 5.1), continuum robots are anticipated to offer rotation motion to clear obstacles as well. Simply mounting a motor at the base is not applicable because the rotation motion may not be properly transmitted to the end effector without proper control algorithm. In detail, when the two axes (mo-

tor's shaft and the deformed backbone of the continuum robot) are not collinear, the fixed-axis rotation at the base would lead to a large motion to the robot body as well as the end-effector. The entire robot shape will rotate around the motor's shaft if the shape configuration keeps constant, without rotation along the robot backbone. A compliant shaft can be considered to mount inside the hollow soft manipulator and motor rotates it at the base, as shown in Fig. 5.1 (upper), but the deformation of the metal compliant shaft may cause resistance to the bending of the soft continuum robot. Additionally, the frictional interaction between the compliant shaft and the manipulator would cause vibration and abrase the soft material. Therefore, it requires delicate design and controller for multi-segment manipulators to realize continuous rotation along the deformed backbone (CRADB). To the best of our knowledge, there is no similar research for a multi-segment continuum robot with positioning and CRADB implementation simultaneously.

5.2 System Description

5.2.1 Working Principle of CRADB

Fig. 5.2 illustrates the working principle. Take a single-segment manipulator vertically mounted on a rotatable platform as an example, and its deformation depends on the pneumatic pressure inside the three chambers (Fig. 5.2 (a)). The shape of it can be assumed as an arch (Fig. 5.2 (b)), described by shape configuration parameters: direction angle φ_k, bending angle θ_k and bending radius r_k. Ideally, if the actuators inputs A_k are properly set, the tip of the flexible manipulator can be moved to follow a circular path (see Fig. 5.2 (c)), where the bending angle is unchanged ($\theta_{k+1} = \theta_k$). The direction angle varies as: $\omega_{k+1} = \varphi_{k+1} - \varphi_k$, and k denotes control instance. Simultaneously, the base rotates towards the opposite direction by ω_{k+1} (i.e. $-\omega_{k+1}$), to compensate the direction angle variation, and then the direction angle of the manipulator can restore back to the previous value φ_k (Fig. 5.2 (d)). The whole shape of the manipulator can be kept, but it has been

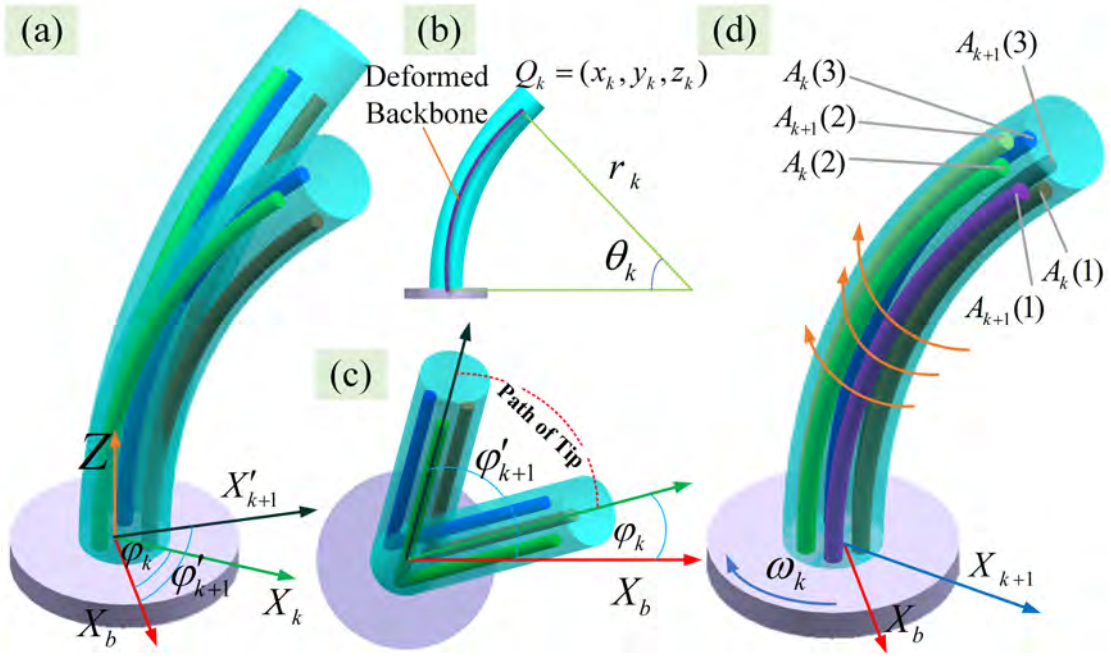

Fig. 5.2. Working principle of CRABD motion. (a) Shape/tip varies actuated only by air pressures. (b) Robot shape is parameterized by φ_k, θ_k, and r_k. (c) Top view for a circular path achieved by pressurized air. (d) CRADB is achieved by air pressures and the rotatable base simultaneously.

rotated along the deformed backbone. Therefore, CRADB is the resultant motion from pneumatic regulators inputs and the motorized rotatable base. To illustrate the working principle more clearly, the kinematic model relating the length change of the ith chamber to the resultant shape configuration parameters is:

$$l_i = \frac{l}{\theta}(1 - r_c \cos(\varphi + \frac{2\pi}{3}(i-1))), \tag{5.1}$$

where r_c is the distance between chamber's center to the backbone and l denotes the length of backbone. Fig. 5.3 (a) and (b) show robot shape and the chamber length for a circular-path movement, respectively. Simulation towards CRADB is provided in the supplementary video.

5.2.2 Design and Fabrication

Fabrication focuses on the two motions: actuation for deforming the robot and rotation of the base. The design scheme is illustrated in Fig. 5.4. The deformation of the manipulator is achieved by inflating pressurized gas into the chambers and the base is rotated by a stepper motor. As Fig. 5.4 (a) shows, the rotation of

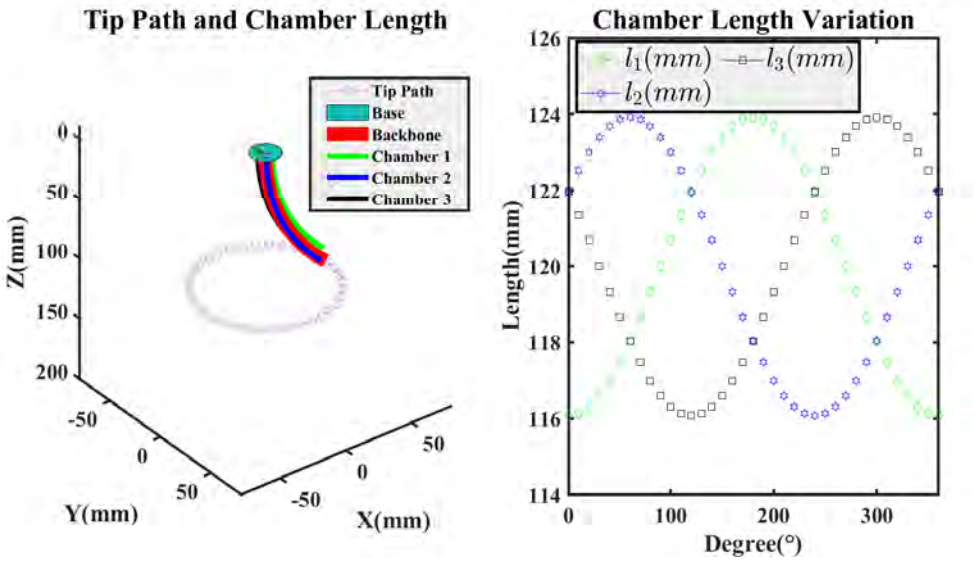

Fig. 5.3. (a) Tip path and robot shape. (b) Chamber length variation.

base will tangle the tubes around the motor shaft, which constrains the rotation within $[-180°, 180°]$. To address this issue, a slip ring is imported to improve the design scheme (Fig. 5.4 (b)), where the transmission of gas goes through the rotor and stator, so that gas tubes will not twine during the base rotation. Fig. 5.4 (c) shows the sectional view of a three-channel slip ring whose central hollow hole can be used to connect stepper motor's shaft and slip ring's rotor. The manipulator's base is mounted at the rotor, and the stator is fixed on the frame. In Fig. 5.4 (d), CAD model of the entire system further shows the design scheme. The reason why we select pneumatic-driven mechanism is that gas tube can be changed into any shape and can be easily transmitted, and sophisticated slip ring can decouple the transmission without air leakage concern.

To fabricate the compliant manipulator, mold cast technology was employed. A 3D-printed mold was prepared first and silicone rubber (E605, Hongye, Shenzhen, China) was then poured into it to obtain a flexible manipulator (see Fig. 5.5 (a)) after casting. After demolding, one thread was twined around the manipulator's surface groove to limit radial expansion when being pressurized (Fig. 5.5 (b)). To limit the total length of the manipulator, another thread connects between the cap ring and the base. Similarly, another slender segment (red in Fig. 5.5 (d)) was fabricated and connected in series with the proximal segment (blue in Fig. 5.5

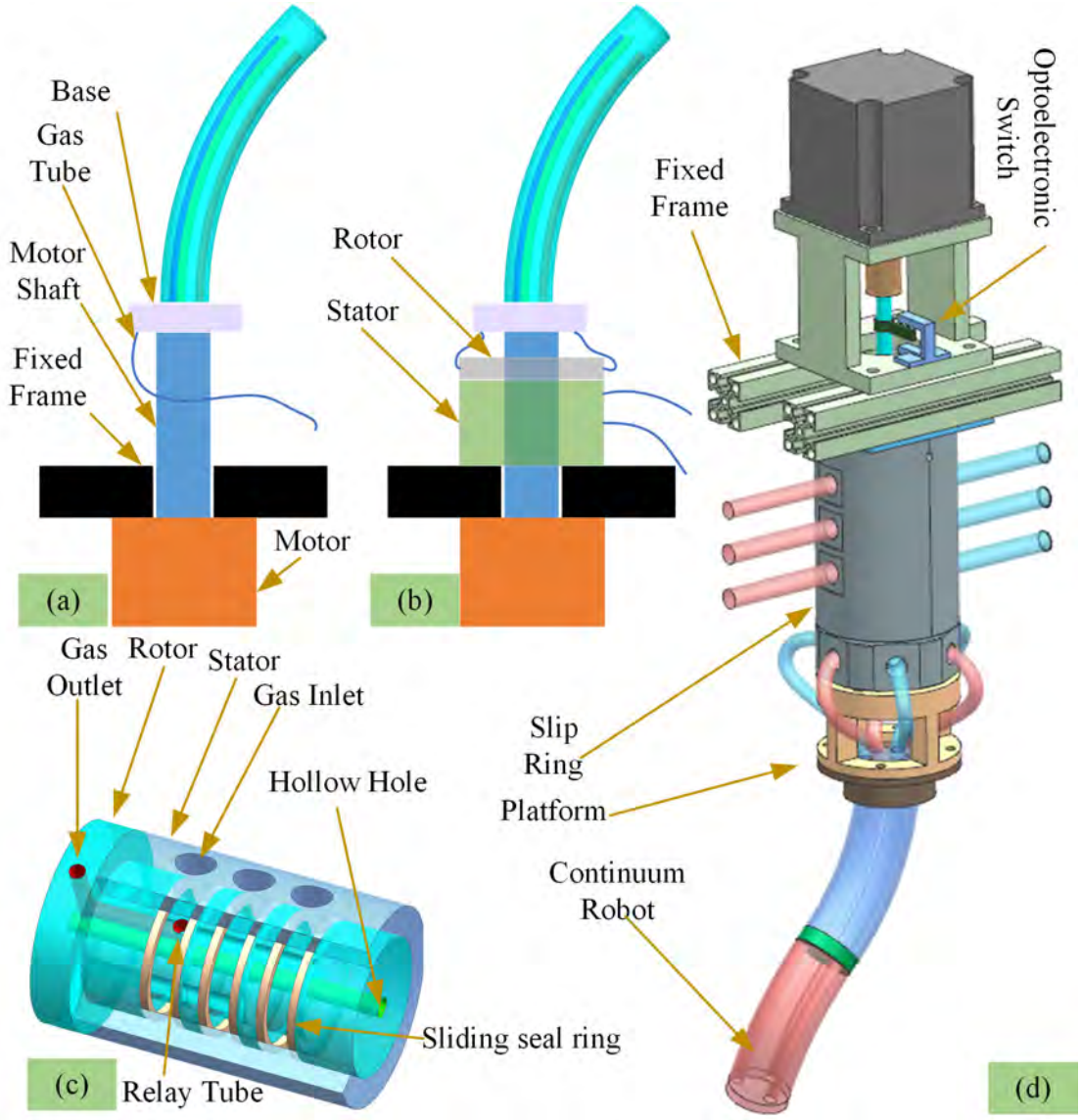

Fig. 5.4. Inspiration and design scheme. (a) Tubes are tangled around motor shaft during rotation. (b) Design with a slip ring to decouple air transmission. (c) Sectional view of a three-channel slip ring. (d) CAD model of the design.

(d)). Next, air tubes for actuation were sequentially connected among pneumatic regulators, the slip ring and the robot.

The entire experimental setup is shown in Fig. 5.5 (e) and (f). Pneumatic regulators (SMC, ITV0030-BL) were employed to precisely control the pneumatic pressure of each chamber at an accuracy of 0.01 bar, and a stepper motor (57BYG250B) mounted at the aluminium frame rotates the base. In order to sense the shape and tip position configurations, a well calibrated RGB-D camera (Intel Realsense, D415) was considered, and two colorful markers are attached at

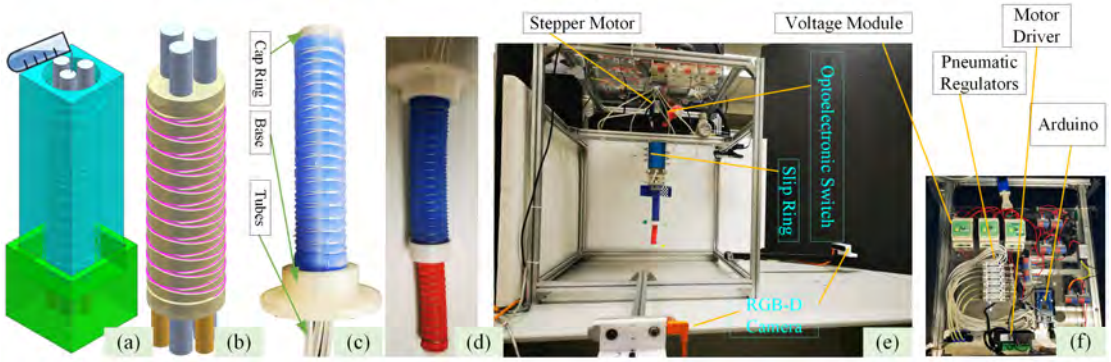

Fig. 5.5. System setup. (a) 3D printed mold. (b) Soft manipulator with twined thread. (c)-(d) Snapshot of a single and the dual-segment continuum robot. (e) Overall system. (f) Main hardware configuration.

the end of each segment to label the tip position. Two checkerboards were employed to initially calibrate the two cameras to evaluate their respective position with respect to the robot base. An optoelectronic switch (Omoron, EE-SX672P), whose signal is transmitted to Arduino Mega 2560, provides a reference origin of the motor.

5.3 Controller Design

As can be seen in Fig. 5.2, the motor and air pressures jointly determine the direction angle of the proximal segment, and the motor performs well in terms of rotation accuracy and velocity. Therefore, an optimization-inspired method was proposed for tip configuration control. Next, the algorithm to synchronize the two motions is presented to achieve CRADB motion.

5.3.1 Shape Configuration

As shown in Fig. 5.6 (a), the shape of the entire manipulator can be assumed as two arches connected in series. Since the length of each segment is constant, only four variables $[\varphi_1, \theta_1, \varphi_2, \theta_2]$ can parameterize the shape configuration, w.r.t frame $\{1\}$. With the stepper motor, the actual direction angle of the proximal segment becomes: $\Psi_1 = \varphi_1 + \theta_M$ (θ_M is the angular displacement of the motor), and frame $\{0\}$ is fixed. The true position of the proximal tip $Q = (x_2, y_2, z_2)$ and the distal tip $P = (x_4, y_4, z_4)$, w.r.t frame $\{0\}$, can be directly obtained via the

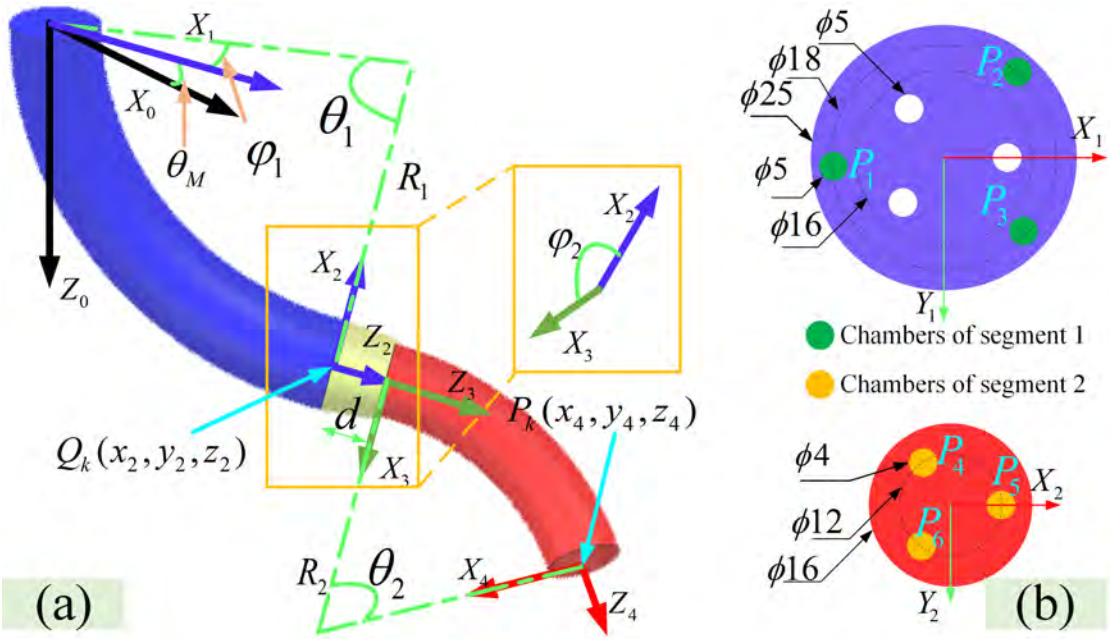

Fig. 5.6. (a) Illustration of deformation and coordinate frames. (b) Dimension of the dual-segment manipulator, and the length of the two segments are $100mm$ and $80mm$, respectively.

vision system, with which the shape parameters are:

$$\Psi_1 = \text{atan2}(y_2, x_2), \theta_1 = 2\text{acos}(\frac{z}{\sqrt{x_2^2 + y_2^2 + z_2^2}}), R_1 = l_1/\theta_1, \tag{5.2}$$

where l_1 is the length of proximal backbone. The shape configuration of the distal segment can also be solved similarly and is omitted for brevity. As a result, the tip pose is then obtained using five variables $[\theta_M, \varphi_1, \theta_1, \varphi_2, \theta_2]$, through Homogeneous transformation: ${}^0_4T(\theta_M, \varphi_1, \theta_1, d, \varphi_2, \theta_2) = {}^0_1T\,{}^1_2T\,{}^2_3T\,{}^3_4T$ ($d = 10mm$ is the connector thickness shown in Fig. 5.6 (a)). Therefore, a given desired tip configuration maps with a shape configuration. Due to the hyper redundancy, there may exist multiple shape configurations for a desired tip configuration, inspiring us to employ optimization algorithm to find the optimal solution, which is detailed in Section-5.3.2. Then, Jacobian-based control scheme maps with the optimal shape configuration with proper actuators inputs, which will be elaborated in Section-5.3.3.

5.3.2 Finding the Optimal Shape Configuration

Let $\psi = (\theta_M, \varphi_1, \theta_1, \varphi_2, \theta_2)$ denote the shape configuration. For a desired tip configuration T_d, the optimization problem becomes: finding the optimal ψ_s under

the current shape configuration ψ_c to make $T_d = T_s$ (T_s is the tip configuration calculated using the optimal ψ_s), which also means minimizing the error between T_d and T_s via finding the optimal ψ_s. Herein, we consider Genetic Algorithm (GA) to solve the optimal ψ_s.

1) *Loss Function*

Loss function is defined as the Euclidean distance between T_d and T_s, each of which consists of a rotation matrix (R_d/R_s) and a translation vector (P_d/P_s). The orientation and position are comprehensively considered in solving the optimal parameters via multiplying a weighting in loss function:

$$L = \omega \left\| R_d - R_s \right\| + (1 - \omega) \left\| P_d - P_s \right\|, \tag{5.3}$$

where ω and $(1 - \omega)$ are respectively weightings for orientation and position. It should be noted that the position vectors are normalized within [0,1] to eliminate the influence of different units. To enable fast point-to-point movement, we can set a larger weighting in the error between the current motor displacement θ_{Mc} and the solved value θ_{Ms}, so that the loss function is updated to:

$$L = \omega \left\| R_d - R_c \right\| + (1 - \omega) \left\| P_d - P_c \right\| + \frac{\omega_M}{\left\| \theta_{Mc} - \theta_{Ms} \right\|}. \tag{5.4}$$

Notably, when setting $\omega_M = 0$, the algorithm works for a conventional dual-segment continuum robot without the rotatable base.

2) *System Constraints*

To avoid buckling, the bending angle and the direction angle of each segment are limited by:

$$\begin{array}{l} 0 \le \theta_{Ms} \le 2\pi; 0 \le \varphi_{1d} \le 2\pi; 0 \le \varphi_{2d} \le 2\pi \\ \theta_{1,\min} \le \theta_{1d} \le \theta_{1,\max}; \theta_{2,\min} \le \theta_{2d} \le \theta_{2,\max} \end{array}. \tag{5.5}$$

3) *Genetic Algorithm for Solving ψ_s*

Genetic Algorithm (GA) is considered to solve the optimal shape configuration ψ_s. In designing the algorithm, each individual in population has one chromosome with five genes. The chromosome represents the five variables that we need to solve, and each gene is coded using binary numbers for further crossover and

mutation process. The optimal chromosome is chosen for random evolution, where the fitness value is evaluated by loss function L. The optimization process was implemented in Matlab 2019b Optimization Toolbox. Specifically, the number of the individual is set to 80, and the initial population is generated randomly. The probability of crossover and mutation are set to 0.8 and 0.05 respectively, where only one binary number of a gene is reversed in each mutation. 'Stochastic Tournament' method is employed in selecting individuals for crossover in next generation.

5.3.3 Jacobian Estimation

After finding the optimal shape configuration ψ_s, system then should set proper pneumatic pressure for each chamber to reach T_s. The chamber length is not directly involved in the air pressure, and more importantly, other factors like uncertain external disturbances and fabrication imperfections, all pose difficulty in finding direct air pressures.

In robotics, Jacobian matrix J maps between the velocity of actuators and tip pose, which can also be converted into the mapping between actuators and shape configuration: $\Delta\psi = J\Delta A$. Within a short interval, this equation can be converted as a local mapping in control instance k: $\psi_{k+1} - \psi_k = J_k(A_{k+1} - A_k)$, so for an optimal ψ_{k+1} calculated from T_d, the theoretical actuation inputs A_{k+1} is:

$$A_{k+1} = J_k^{\dagger}(\psi_{k+1} - \psi_k) + A_k, \tag{5.6}$$

where $J_k^{\dagger} = (J_k^T J_k)^{-1} J_k^T$ denotes the pseudo inverse of J_k. To promote effectiveness, $J_k^{\dagger}$ only maps between pneumatic regulators and $[\varphi_1, \theta_1, \varphi_2, \theta_2]$. Namely, we find Jacobian matrix J_k to control the shape configuration: $[\varphi_1, \theta_1, \varphi_2, \theta_2]$ w.r.t frame $\{1\}$ shown in Fig. 5.6 (a), because the control towards stepper motor is sophisticated and accurate. However, $J_k^{\dagger}$ is still not reliable enough due to uncertain disturbances, such that online estimated Jacobian matrix would be an alternative.

Air pressure and shape configuration do not vary significantly within a short

interval, so that J_k can be assumed as partially dependent on previous M control instances. Inspired by [166], we proposed a method to online update J_k by minimizing the sum of previous M steps' mapping:

$$J_k = \arg\min_{J_k} \sum_{i=k-1}^{k-M} \|W_i(\psi_{k+1} - \psi_i) - W_i J_k(A_k - A_i)\|, \tag{5.7}$$

where $W_i = \frac{1}{1+\exp(E_i)}$ denotes the weight of the ith previous step, and $E_i = \|\psi_i - \psi_{i-1,p}\|$ is Euclidean distance between the planned and the actual shape configuration. This indicates the inaccuracy of the ith step, so a lower weighting is considered.

In addition, the task space can be divided into N sub-spaces, and the Jacobian matrix in a sub-space can be pre-calculated to provide a reference J_s for the online estimation algorithm, so (5.7) become:

$$\begin{aligned} J_k = \arg\min_{J_k} \sum_{i=k-1}^{k-M} (&\|W_i(\psi_{k+1} - \psi_i) - W_i J_k(A_k - A_i)\| \\ &+ w_s \|J_k - J_s\|), \end{aligned} \tag{5.8}$$

where $w_s = 0.1$ is the weighting of the reference Jacobian matrix in the sth sub-space.

5.3.4 Controller for CRADB

As analyzed in Section-5.2.1, when executing CRADB task, controller sets proper air pressure to maintain the bending angle while controlling the direction angle varies continuously. Controlling the angular displacement of the stepper motor's shaft is relatively easier, which was commanded to follow the direction angle of the proximal segment oppositely. It is theoretically feasible to employ (5.8) to control the air pressures, but CRADB motion requires time effectiveness in terms of calculation. Due to the softness of the manipulator, this work assumes the robot is load-free in executing CRADB motion.

Therefore, a simpler controller only towards the direction angle control is individually designed. As expressed in (1) of [167], the pressure of each chamber

follows a mapping between the bending angle and between the direction angle:

$$\begin{aligned} \varphi_1 &= f(p_1, p_2, p_3) = \text{atan2}(\sqrt{3}(p_2 - p_3), p_2 + p_3 - 2p_1) \\ \theta_1 &= g(p_1, p_2, p_3) = \kappa\sqrt{p_1^2 + p_2^2 + p_3^2 - p_1p_2 - p_1p_3 - p_2p_3}, \end{aligned} \tag{5.9}$$

where κ denotes the stiffness of the soft manipulator that is experimentally obtained, and p_i is the air pressure in the ith chamber. For the desired direction angle φ_{1d} and the bending angle θ_{1d}, systems can find the optimal actuation inputs (p_1, p_2, p_3) via:

$$\begin{aligned} (p_1, p_2, p_3) &= \arg\min_{p_1,p_2,p_3} \|f(p_1, p_2, p_3) - \varphi_{1d}\| \\ \text{w.r.t} : &\begin{cases} 0 \le p_i \le p_{\max}(i = 1, 2, 3) \\ g(p_1, p_2, p_3) = \theta_{1d} \end{cases} . \end{aligned} \tag{5.10}$$

The two constraints were respectively designed to avoid over-pressurization and to maintain the bending angle.

Since the $atan2(\cdot)$ function is non-linear, the optimization would be challenging. Taylor expansion is employed to simplify $f(p_1, p_2, p_3)$:

$$\varphi_1 = \varphi_{1c} + \frac{\partial f}{\partial p_1}(p_1 - p_{1c}) + \frac{\partial f}{\partial p_2}(p_2 - p_{2c}) + \frac{\partial f}{\partial p_3}(p_3 - p_{3c}), \tag{5.11}$$

where φ_{1c} denotes the current direction angle, and p_{ic} is the current pressure in the ith chamber. This simplification holds because in operation the direction angle varies gradually for achieving a circular movement. For the distal segment, the tip of the proximal segment acts as its base and the distal segment rotates towards the opposite direction to maintain the shape configuration. (5.10) is also feasible for calculating the air pressure in the distal segment, namely $\varphi_{2d} = -\varphi_{1d}$ and $g(p_4, p_5, p_6) = \theta_{2d}$. The calculation was exceeded in Matlab 2019b Constrained Optimization *fmincon*. It results the whole soft manipulator to rotate around the deformed backbone while holding the shape unchanged.

5.4 Experimental Validation

Experiments were conducted to validate this work, including the fundamental functions of the design, movement of the tip and more importantly the performance of CRADB.

5.4.1 Experiment Setup

Through calibration, the measurement precision of the vision system is around $1.5mm$, which was assumed as ground truth in implementation. To find the real-time actual position of the tips (Q and P), RGB and HSV characteristics of the sampled pictures were considered to extract the pixel position of the markers, and the calibration model further solved the tip's position. The rotation of the base and movement of the two segments are displayed in the supplementary video, showing that the base's rotation does not influence the transmission of the pressurized air. Robot was randomly commanded with a ± 0.05 bar pressure changed randomly in each chamber, to explore its task space and to solve the local Jacobian matrix. As a result, 1000 sets of data was collected and 8 sub-spaces were divided based on the shape configuration of the entire manipulator to find local Jacobian matrix J_s.

5.4.2 GA to Search the Optimal SC

GA plays a critical role in finding the optimal shape configuration for a given tip configuration, so its accuracy is highly involved in the motion velocity and precision.

First, the weight ω is set to 0.5, averagely considering orientation and position accuracy. The current shape configuration is $\psi_c = [0, \frac{\pi}{6}, \frac{\pi}{3}, \frac{\pi}{5}, \frac{\pi}{4}]$ and the desired tip configuration is set to $T_d = transl(82, 35, 160) \cdot trotz(\pi/6) \cdot trotx(\pi/4)$. The finally solved $\psi_s = [0.523, 0.001, 0.5636, 1.0472, 0.3143]$ (unit: rad), such that the Loss function is only 0.157 with the position error of 1.7084 mm. The imported weight in (5.4) contributes to smaller value in direction angle φ_1 and bigger value in θ_M. Besides, as depicted in Fig. 5.7 (a), GA reached convergence at the 40th generation after 0.08s, which is regarded as time effective. Moreover, a circular path was considered to implement the algorithm, where the diameter of the path was $180mm$ and totally 12 path points with 30° radially apart were tested. The desired tip configuration varied at each path point to further test the

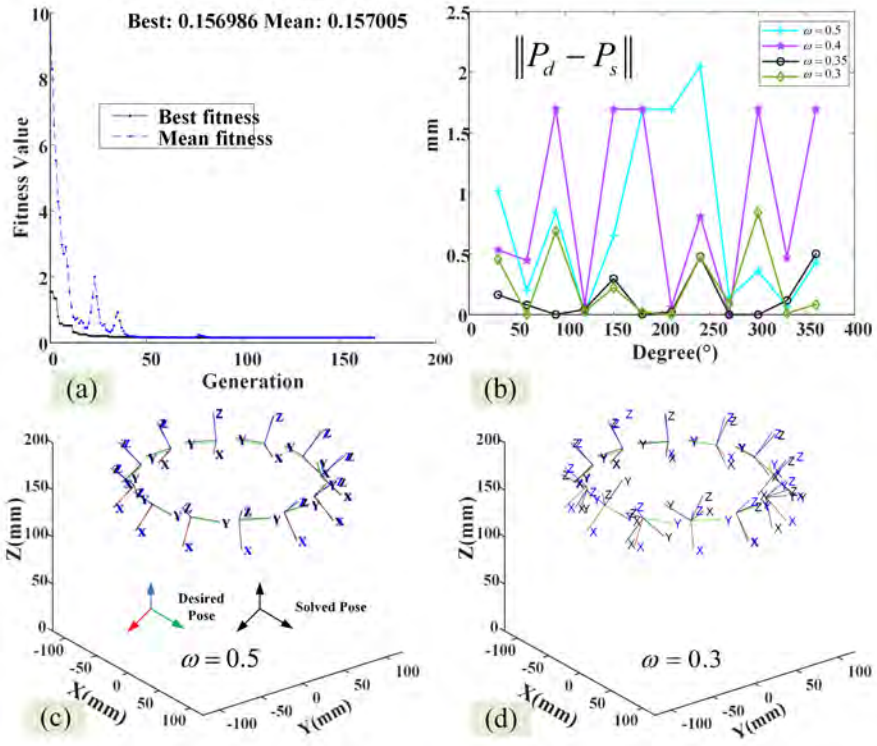

Fig. 5.7. (a) Searching process of GA. (b) position error between the solved and the given. (c) and (d) comparison between the solved pose and the given with $\omega = 0.5$ and 0.3, respectively.

performance, and the results are displayed in Fig. 5.7 (c). The solved tip pose was almost consistent with the desired, and the maximum position error was only $2.15mm$ shown in Fig. 5.7 (b). In addition, the weight ω between the position and orientation was adjusted from 0.5 to 0.3 to investigate the final position error, which means we care more about the position compared to orientation. As shown in Fig. 5.7 (b), smaller ω benefits higher position accuracy, but the orientation accuracy is low. When $\omega = 0.3$, the maximum position error $\|P_d - P_s\| = 0.62mm$ but the orientation R_s deviates obviously between the desired R_d, as Fig. 5.7 (d) shows. Therefore, we select $\omega = 0.5$ as the optimal weight. The time cost for each optimization was about $0.18s$, which we believe is sufficient for online implementation.

5.4.3 Point-to-Point Movement

The pressures inside the six chambers were set to $[0.8, 0, 0, 0.35, 0.35, 0]$ (unit:bar) and the position of the tip was regarded as the starting point for point-to-point movement test. The destination was set to $[-63, 62, 165](x, y, z)$ and the desired orientation represented by Euler angle was $[7°, 17°, -50°]$. For this desired tip configuration, GA solved the optimal shape configuration $\psi_s = [122.96°, 8.57°, 56°, 232°, 73.5°]$, and the initial tip configuration $\psi_c = [0°, 8.6°, 52.4°, 289.9°, 38.7°]$. Then robot system adjusted the pressures to reach the solved ψ_s. The weight ω_M was also set to 0.1, and M is 10. Robot was commanded to move to ψ_c with 10 steps, to solve the corresponding Jacobian matrix.

In the first testing, the stepper motor was kept idle to test the accuracy of the Jacobian estimation method and to investigate the motion time cost. The robot took 10 steps to finish the point-to-point movement task. The path points of the two tips (Q and P) are illustrated in Fig. 5.8 (a). As Fig. 5.8 (e) and (f) show (cyan curves), the direction angle and the bending angle gradually reached to the optimal values.

Secondly, both the stepper motor and pneumatic regulators was used to execute the same task. Since the motor can provide fast response, the rapid start/stop could cause a large vibration to the robot. In this work, proper transition time from acceleration/deceleration stage to the constant speed was provided and the speed was set to a small value to minimize the vibration. The maximum velocity of the motor is $60rpm$. The motor rotated by 122.96°, and simultaneously pneumatic regulators started to approach the destination. The direction angle of the proximal segment just needed to change 8.57° in the subsequent motion process. In Fig. 5.8 (e) (purple curves), the direction angle Ψ_1 directly increased from 0 to 122.96°, and the bending angles gradually reached the desired values actuated by air pressure.

To test the performance of disturbance adaption, random manual disturbance was added just after motor rotation (the 2nd step, see Fig. 5.8 (d)), making the robot deviate from its planned path point. Then, the Jacobian matrix updated

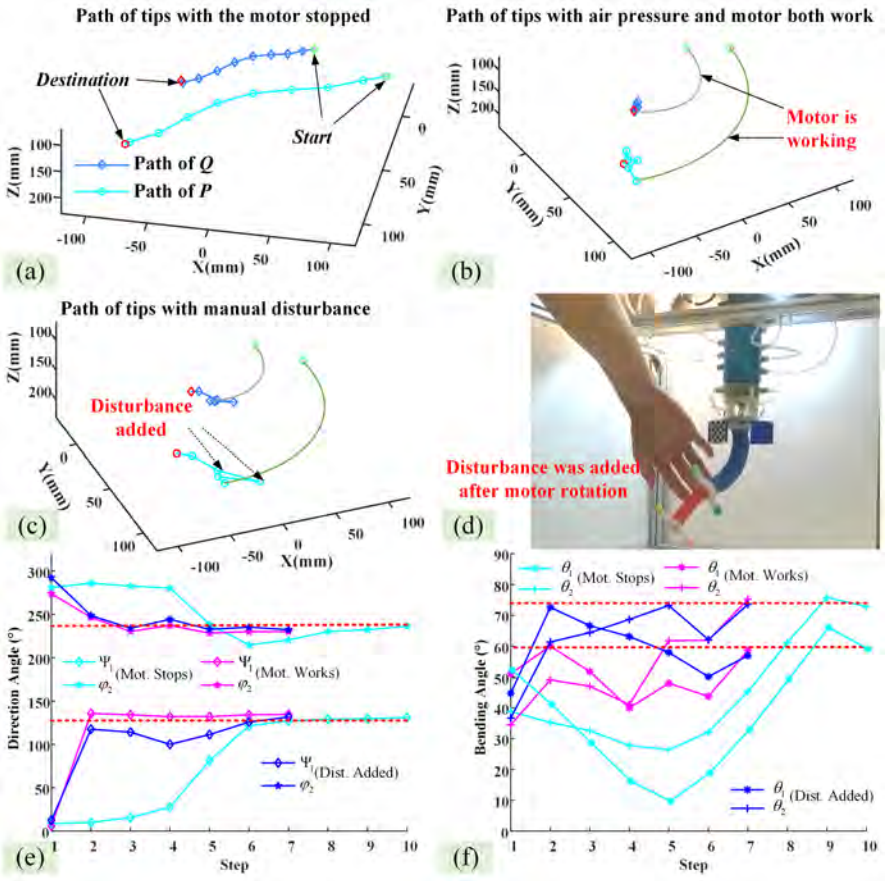

Fig. 5.8. (a) Tips path in motor-idle mode. (b) Tips path with motors and pneumatic regulators both worked. (c) Tips path with disturbance. (d) snapshot of manual disturbance. (e) Variation of direction angle. (f) Variation of bending angle.

accordingly under the disturbance, bringing the tip to the destination. At the 4th step, the disturbance was removed. The Jacobian updated accordingly as well and brought the tip back to the desired value smoothly with air pressure. It can be seen from Fig. 5.8 (e) and (f) (blue curves), Ψ_1 did not change significantly even when the disturbance was introduced and then removed. The change in the bending angle due to the disturbance is more obvious. After the disturbance, they reached the desired values, similar to that in load-free condition. It totally took 7 steps to reach the destination, showing that the Jacobian matrix works effectively.

In the above experiments, $M = 10$ was a constant and the maximum position error between the planned position and the actual is $6.73mm$. To investigate the influence of M, different values were set. By setting 5 different values of M for

Table 5.1: Position error between the planned position and the actual with different values of M.

M	**8**	**10**	**14**	**16**	**20**
Max. Err.(mm)	8.29	6.73	7.36	9.35	12.35
Mean Err.(mm)	6.87	5.31	6.52	7.46	10.65

the same path in load-free condition, the positional error shows the performance. The result is listed in TABLE-5.1. The optimal value is $M = 10$, and the time cost of the calculation is around $0.34s$ for each step. Larger M considered too much information from the previous steps, which does not satisfy the principle of Jacobian matrix that maps actuators and tip position within a local area, while smaller value can not fully make use of the local information. Therefore, in the following experiments, M was set to 10.

5.4.4 Path-Following Testing

Apart from the point-to-point movement tests, path-following tasks were also prepared on the basis of the optimal parameters, where both the pneumatic regulators and the motor worked. The motor maximum velocity was set to $48rev/min$, and the direction angle φ_1 was set to zero, which aims to enhance the overall motion velocity. Namely the direction angle of the proximal segment Ψ_1 was only achieved by the stepper motor, and air pressure in the proximal segment only worked for the bending angle θ_1.

First, a 3D square-shaped path was designed with discrete path points, and the tip orientation was set to $trotz(atan2(y, x)) \cdot trotx(\pi/4)$, where x, y denotes the coordinate of the path points. Because of the inertial effect, vision system collected the two tip positions $2s$ after setting actuation inputs. Fig. 5.9 (a) shows the comparison between the actual path points and the desired points, demonstrating that the tip generally followed the desired path. As shown in Fig. 5.9 (b), the shape configuration parameters were also generally consistent with the values calculated by GA algorithm. There was little deviation in Ψ_1 since the motion accuracy of the stepper motor is much higher than that of air

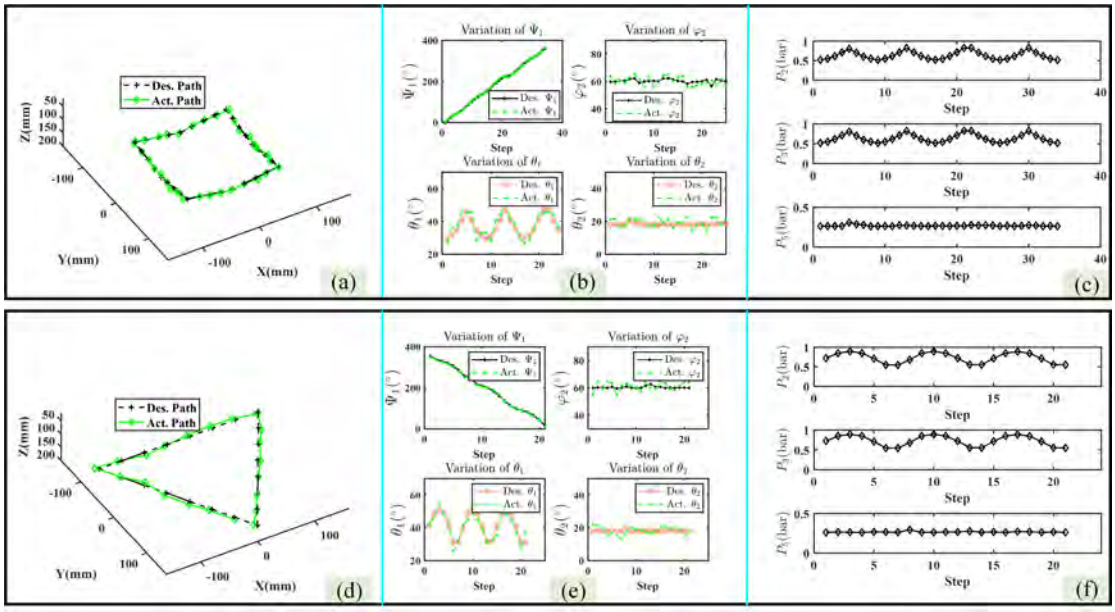

Fig. 5.9. (a),(d) Path-following results. (b),(e) Variation of shape configuration parameters. (c),(f) Actuation configurations.

pressure. The bending angle of the distal segment deviated relatively significant from the optimal value, due to the moment of gravity. This mainly leads to the positional error in the tip. Fig. 5.9 (c) shows the variation of air pressure in the actuated chambers. Only the 2nd, 3rd and 5th chambers were actuated because the proximal segment only needs to bend ($\varphi_1 = 0$) and the direction angle of the distal segment should approach to 60° to maintain the given orientation. Next, another planar triangular path was designed to do similar test. As Fig. 5.9 (d) shows, the actual path deviated more from the desired one, because the robot cannot ensure both orientation and position simultaneously. Corresponding shape configuration parameters are shown in Fig. 5.9 (e), and the positional deviation falls into the bending angle θ_1 and θ_2. Fig. 5.9 (f) shows the air pressures variation.

For the first path, the whole process only took $32s$ in comparison with $98s$ used in the mode of without the stepper motor. The decrease in the operating time shows that the added DoF enhances the motion velocity of continuum robot effectively. The two experiments further demonstrate the the success of the imported revolve joint and the feasibility of the Jacobian matrix estimation method.

5.4.5 CRADB Testing

1) *One-Segment Testing*

The three chambers in the distal segment were inflated and kept at an accuracy of 0.2 bar, to provide the basic rigidity for the same. Different pneumatic pressure values were set at the proximal segment to test the performance of circular path movement of using one segment.

The air pressure at the proximal segment were set to $[0.8, 0, 0]$ bar initially, after which the shape configuration was accordingly solved to ensure the tip Q can follow a circular path. Using (5.10), the corresponding air pressure was obtained for each path point at the circular path with a radius gap of 10°, which took in total $2s$ for the all 36 path points. The pressure values were then gradually commanded to the robot to follow the circular path, and the results is shown in Fig. 5.10 (a). The 12th path point exhibited low accuracy due to fabrication imperfection.

Then, the stepper motor started to rotate clockwise ($\dot{\theta}_M = 48rpm$) and the direction angle φ_1 changed counterclockwise simultaneously, with a gap of 10°. The marker's position shows the rotation performance. Better circular degree represents more accurate motion, showing the feasibility of the controller. The true position of two markers at the two segments during all the 36 steps are shown in Fig. 5.10 (b). They generally followed a circular path around the true tip, and the maximum error is around $15mm$ due to inertial effect and soft material. With the characteristics of soft continuum robot, the result shows the success of the proposed CRADB motion.

2) *Two-Segment Testing*

The success of the single-segment rotation provides the foundation for implementation on two-segment setup. Similarly, the distal segment was also commanded to follow a circular path while the proximal segment was deformed. The actual path of the distal tip is shown in Fig. 5.10 (c), where the gravity of the distal segment led to vibration in the entire manipulator. Consequently, the actual

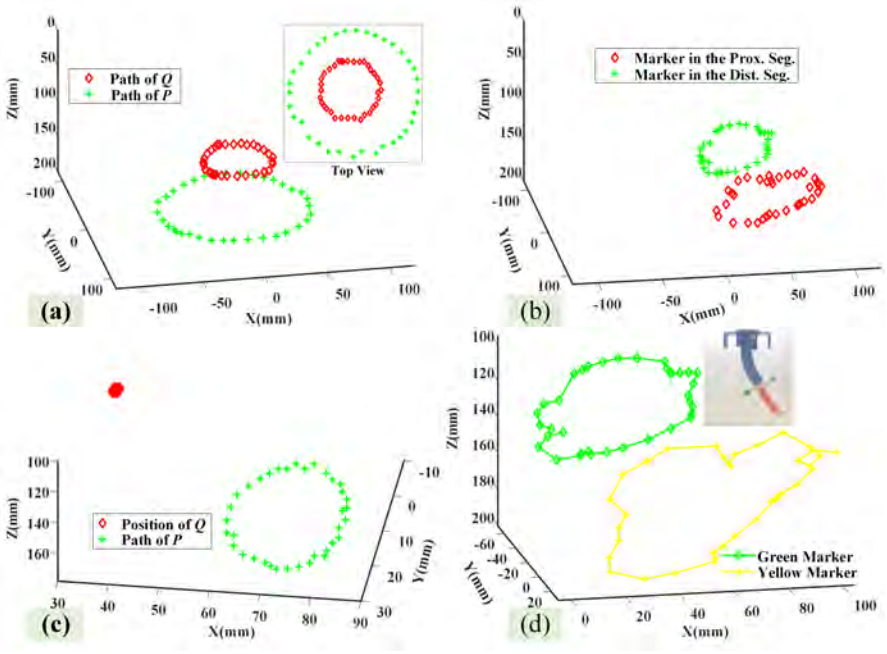

Fig. 5.10. (a) Circular path movement of tip Q (Q and P respectively indicate the tip in the proximal and the distal segment.) (b) CRADB of the proximal segment. (c) Circular path movement of tip P. (d) CRADB of the whole manipulator.

path deviated downwards from the desired circular path, in which the maximum position error is around $7mm$.

Next, the two segments and the stepper motor both started to work simultaneously, and the pneumatic pressure in the distal segment varied as planned. The two markers beside the two tips were also considered to manifest the CRADB behavior, and the results are shown in Fig. 5.10 (d). During this process, the inertial of the two segments jointly influence the rotation precision so that the position error of the two makers are $18mm$ and $29mm$. The compliance of the manipulator would cause almost no harm to the ambient environment, such as working in MIS. Therefore, we believe that the accuracy is acceptable for this novel design, and in future closed-loop control or robot with stiffer material will be employed.

5.4.6 Applications

The proposed robot was tested to show its capability for various potential applications.

1) *Tea Water Suction*

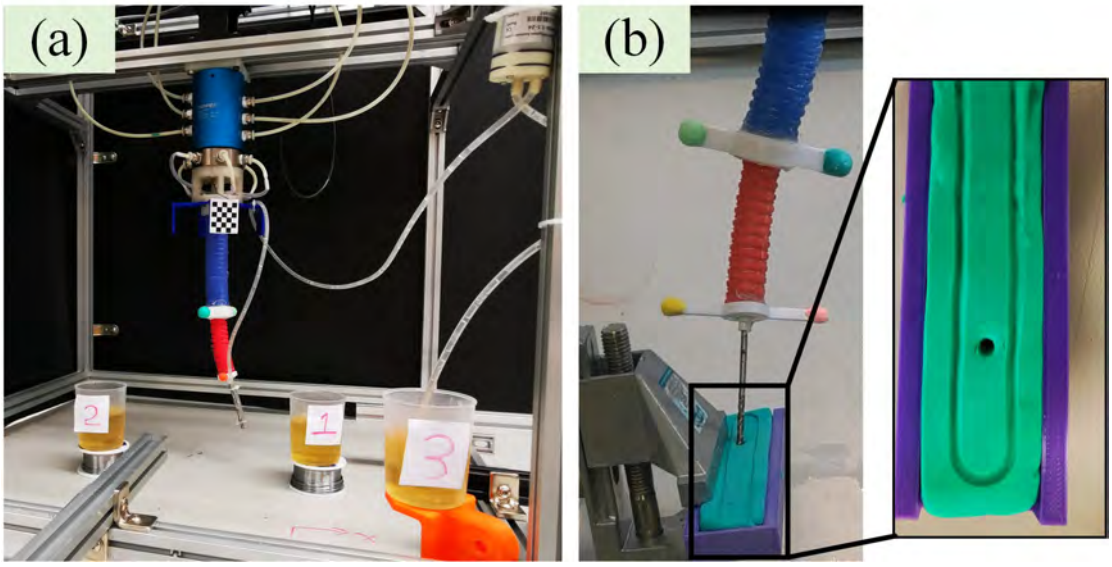

Fig. 5.11. (a) Tea water suction. (b) Drilling.

In this demonstration, a soft tube was fixed at the robot tip and a suction pump was attached at the tube's another end to provide negative pressure. As Fig. 5.11 (a) shows, the tip of the manipulator was commanded to reach the two small cups, and the pump started to collect the fluid accordingly. When approaching cup 1, pneumatic actuators were only commanded as bending angles were needed to be varied. After finishing the suctioning task in cup 1, both pneumatic inputs and the stepper motor were used to help positioning the tip to cup 2, and slowly moved downwards to suck the water. With proper motion control towards the stepper motor, no significant vibration was observed when the motor stopped. Therefore, the use of the stepper motor could benefit shape configuration variation. Supplementary video showcases the whole suctioning process.

2) *Drilling Task*

In the second demonstration, an drill bit ($\phi 4mm$) was mounted a the tip of the robot, and a flat surface made of plasticine was prepared to mimic the object to be drilled, as shown in Fig. 5.11 (b). After reaching the specified point on the surface, the pneumatic inputs and the stepper motor worked together to provide the rotational motion while maintaining the same shape configuration. The plastic fixture holding the plasticine set the distance to be drilled, and fluctuation at the

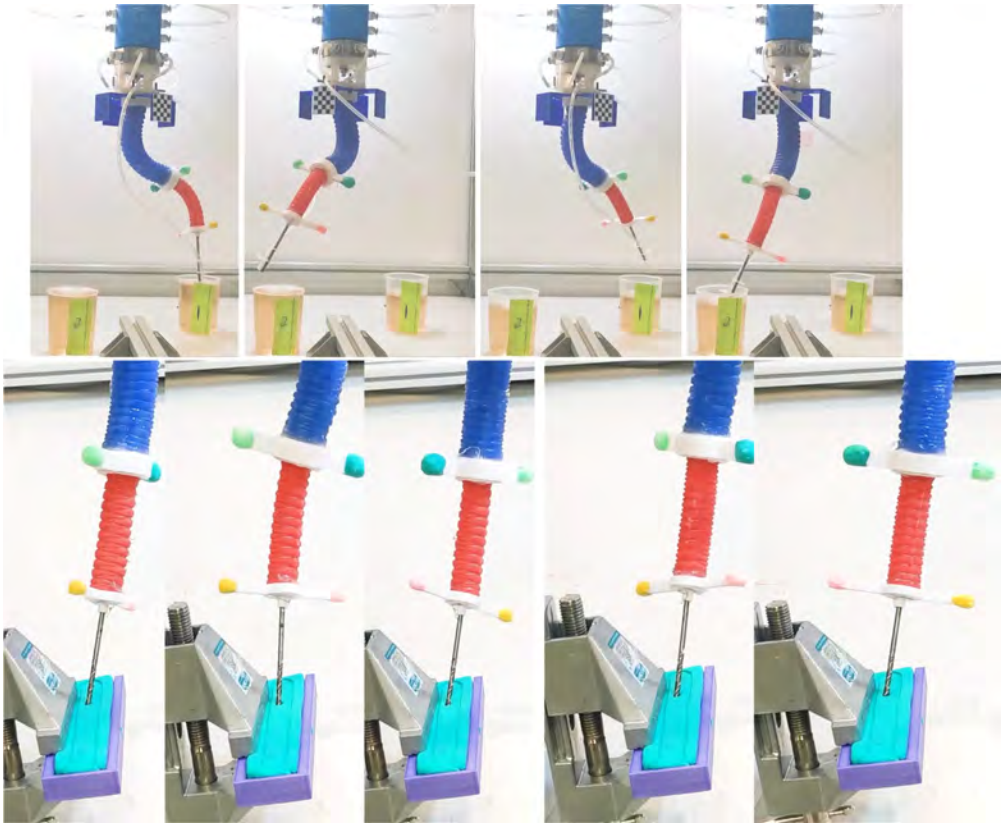

Fig. 5.12. (a) Snapshots of tea-water transmission. (b) Snapshots of drilling.

distal segment was observed when reaching the fixture. This demonstration shows that a small hole was successfully created on the plasticine. The roundness of the hole is $0.3mm$. Some snapshots of the robot are shown in Fig. 5.12.

5.5 Chapter Summary

This work proposed a new design of dual-segment continuum robot, with the capability to provide a rotational motion along the soft body. This additional motion can also help to improve the time effectiveness in reconfiguring the robot tip to reach a particular point. To assure the tip to remain at the same point, a novel control algorithm utilizing the pneumatic inputs and the stepper motor was developed so that the robot body can be rotated continuously, regardless the current shape of different segments. The added DoF does not expand the task space of the robot, but it promotes the response of the first segment. While the new actuator added the redundancy towards the controller, the proposed optimiza-

tion controller is capable of finding the proper shape configuration, and Jacobian method maps the shape configuration to an actuation inputs. Another contribution of this part is that I combined a slip ring in air transmission. Tube twining issue was well processed by this slip ring, so that the rotation of the base would not be limited. With this design, I considered the integration of base's rotation and manipulator's deformation to propose a CRADB motion, which is the first one in continuum robotics community.

Experiments were conducted to show the performance of the robot, and demonstrations were also performed to show potential applications. First, I considered PCC-based simulation to verify the proposed CRADB motion scheme. Then, the proposed controllers were individually tested on the prototype, including pure deformation motion and CRADB on each segment. Additionally, two potential useful applications were prepared to respectively demonstrate the two motions.

However, there are still some limitations in this part especially in terms of algorithm. Robot could only deformation or only rotation, and they cannot be integrated simultaneously. The controller about CRADB only works in load-free scenarios. External effect would make the rotation inaccurate.

Chapter 6

Conclusion and Future Work

6.1 Summary

In this dissertation, some key problems in continuum robotics were solved and the methodology for each of them were validated in the corresponding pneumatic-driven continuum robot.

My work starts from providing a novel solution for users who needs real-time visual feedback of the shape and controls the locomotion of the dual-segment soft manipulator. Both load-free and load conditions were considered. After given a desired position in the tip, system will gradually move towards the goal, with real-time 3D virtual shape provided. Therefore, the solution includes two key parts: shape estimation and control with external disturbances. Since the infeasibility of external sensors, commercial strain gauges were used as internal sensors to quantify the deformation of the manipulator. Delicate fabrication method exhibited appropriate integration between the robot body and the sensors. To map between the sensor readings and the 3D shape, some key points located on the backbone were predicted via data-driven mechanism, and spatial curve fitting algorithm connects them sequentially. The proposed data-driven method takes actuation inputs and sensor readings into account to find the key points because external forces also pose influence to the shape, and the basic functions for the curve fitting suits well with the actual backbone. The shape estimation provides a good tip position feedback for the controller, which was built based on Jacobian matrix that differs from area to area. ANN features comparable generality performance and was

employed to build a data-driven model covering the whole task space. In actual locomotion, an adaptive step distance mechanism (ASDM) was proposed to adapt the uncertainty of external disturbances and enhance locomotion accuracy. Simulation and experiments were conducted to fully validate the two modules. Finite element method (FEM) simulates the robot shape under diversified scenarios, with the inaccuracy of the key points. The control scheme was also initially validated on the basis of PCC model in simulation manner. Results demonstrated that the reconstructed shape matched well with the actual one, and the actual path was almost consistent with the desired with the ASDM. In experiments, point load, distributed load and torsion load were added at a random position of the robot, and the shape reconstruction succeeded estimating the actual shape. The controller was also successfully tested in diversified conditions with point-to-point movement and path-following tasks, proving the proposed method is conducive for users handling the robot needing visual feedback.

To find the uncertain external force acting on robot circumferential body which is a bigger area in comparison to some existing works focusing on the tip, proprioceptive mechanism was developed first. EGaIn alloy was injected inside the manipulator to measure the deformation, leading to overall sensing system. ANN model compares the current tip position with the theoretical value to identify the presence. Then, the surface area was divided by a 2D map (grid). Each grid was labelled by column position and row position. To find them and corresponding magnitude of the force, probability model and virtual work principle were sequentially used. Results confirmed that this method is able to reconstruct the external force with the assumption that only a single force acts. Results also demonstrate the feasibility of the sensing model, position estimation model and magnitude solving method. This approach provided useful information for users to know the ambient environment, such as static obstacles.

Aiming at another continuous rotation issue in continuum robotics, I designed a novel structure and algorithm to enable continuous rotation and omni defor-

mation simultaneously. Adding a new revolute DoF at the base enhanced the dexterity and response velocity during operation. To the best of my knowledge, slip ring was first imported to the design of multi-segment continuum robots, with which the air transmission was decoupled. The added DoF also contributes to higher degree of redundancy, so this work investigated GA optimization algorithm to find the optimal shape configuration. More importantly, the synchronization algorithm between the revolute motion and the pneumatic actuators were investigated to build rotation along the deformed backbone. Experiments showed that the locomotion time with the DoF was far less than the conventional design for a given point-to-point movement. Successful application on water suction and drilling also demonstrated the potential of this design. This provides a novel function of continuum robot based on its deformation, making it applicable in exploring constrained environment.

6.2 Future Work

In my future research, some points should be extended based on the previous achievements:

1) The task space of the soft manipulator is marginal. Although connecting more segments in series could expand it, the fabrication challenge also increases. The whole robot base will be mounted at a linear stage, thereby facilitating fast movement of the manipulator. Then, the whole manipulator can perform wider range of tasks, with deformation, translation, and rotation.

2) The control scheme of the continuous rotation currently is separated with the deformation. Investigating simultaneous movement is also my future work, making the robot can rotate wile shape configuration varies as desired.

3) During rotation, the desired shape was influenced by inertia. To pursue better rotation accuracy and real-time shape configuration, controller with the error of the rotation will be considered in future work. This mitigates fabrication imperfections, and improves the whole locomotion.

6.3 Selected Publications

[1]. **Zhao, Qingxiang**, et al. "Shape estimation and control of a soft continuum robot under external payloads." IEEE/ASME Transactions on Mechatronics (2021).

[2]. **Zhao, Qingxiang**, Jiewen Lai, and Henry Chu. "Reconstructing External Force on the Circumferential Body of Continuum Robot with Embedded Proprioceptive Sensors." IEEE Transactions on Industrial Electronics (2021).

[3]. **Zhao, Qingxiang**, et al. "Dual-Segment Continuum Robot With Continuous Rotational Motion Along the Deformable Backbone." IEEE/ASME Transactions on Mechatronics (2022).

[4]. Hu, Xiaobing, Xi Deng, and **Qingxiang Zhao***. "A gantry robot system for cutting single Y-shaped welding grooves on plane workpieces." Proceedings of the Institution of Mechanical Engineers, Part E: Journal of Process Mechanical Engineering 235.2 (2021): 321-331.

[5]. **Zhao, Qingxiang**, Zhiyi Jiang, and Henry K. Chu. "A Soft-Rigid Air-Propelled Pipe-Climbing Robot." 2021 IEEE International Conference on Robotics and Automation (ICRA). IEEE, 2021.

Bibliography

[1] M. E. Moran, "Evolution of robotic arms," *Journal of robotic surgery*, vol. 1, no. 2, pp. 103–111, 2007.

[2] M. E. Rosheim, *Robot evolution: the development of anthrobotics*. John Wiley & Sons, 1994.

[3] T. Owen, "Biologically inspired robots: Snake-like locomotors and manipulators by shigeo hirose oxford university press, oxford, 1993, 220pages, incl. index (£ 40)," *Robotica*, vol. 12, no. 3, pp. 282–282, 1994.

[4] G. Immega, K. Antonelli, and J. Ko, "Teleoperation of the ksi tentacle manipulator for hot cell decontamination," in *1995 IEEE International Conference on Systems, Man and Cybernetics. Intelligent Systems for the 21st Century*, vol. 3. IEEE, 1995, pp. 2133–2136.

[5] O. Larson and C. Davidson, "Flexible arm, particularly a robot arm," Jul. 19 1983, uS Patent 4,393,728.

[6] K. Suzumori, S. Iikura, and H. Tanaka, "Applying a flexible microactuator to robotic mechanisms," *IEEE Control systems magazine*, vol. 12, no. 1, pp. 21–27, 1992.

[7] G. Robinson and J. B. Davies, "Continuum robots - a state of the art," *Proceedings - IEEE International Conference on Robotics and Automation*, vol. 4, no. May, pp. 2849–2854, 1999.

[8] V. K. Chitrakaran, A. Behal, D. M. Dawson, and I. D. Walker, "Setpoint regulation of continuum robots using a fixed camera," *Robotica*, vol. 25, no. 5, pp. 581–586, 2007.

[9] M. Csencsits, B. A. Jones, W. McMahan, V. Iyengar, and I. D. Walker, "User interfaces for continuum robot arms," in *2005 IEEE/RSJ International Conference on Intelligent Robots and Systems*. IEEE, 2005, pp. 3123–3130.

[10] D. Braganza, M. L. McIntyre, D. M. Dawson, and I. D. Walker, "Whole arm grasping control for redundant robot manipulators," in *2006 American Control Conference*. IEEE, 2006, pp. 6–pp.

[11] V. C. Anderson and R. C. Horn, "Tensor arm manipulator," Feb. 24 1970, uS Patent 3,497,083.

[12] R. Cieślak and A. Morecki, "Elephant trunk type elastic manipulator-a tool for bulk and liquid materials transportation," *Robotica*, vol. 17, no. 1, pp. 11–16, 1999.

[13] H. Tsukagoshi, A. Kitagawa, and M. Segawa, "Active hose: An artificial elephant's nose with maneuverability for rescue operation," in *Proceedings 2001 ICRA. IEEE International Conference on Robotics and Automation (Cat. No. 01CH37164)*, vol. 3. IEEE, 2001, pp. 2454–2459.

[14] R. J. Webster III and B. A. Jones, "Design and kinematic modeling of constant curvature continuum robots: A review," *The International Journal of Robotics Research*, vol. 29, no. 13, pp. 1661–1683, 2010.

[15] Y. Nakamura, A. Matsui, T. Saito, and K. Yoshimoto, "Shape-memory-alloy active forceps for laparoscopic surgery," in *Proceedings of 1995 IEEE International Conference on Robotics and Automation*, vol. 3. IEEE, 1995, pp. 2320–2327.

[16] P. Sears and P. E. Dupont, "Inverse kinematics of concentric tube steerable needles," in *Proceedings 2007 IEEE International Conference on Robotics and Automation*. IEEE, 2007, pp. 1887–1892.

[17] K. Ikuta, M. Tsukamoto, and S. Hirose, "Shape memory alloy servo actuator system with electric resistance feedback and application for active endoscope," in *Proceedings. 1988 IEEE International Conference on Robotics and Automation*. Ieee, 1988, pp. 427–430.

[18] P. Dario, M. C. Carrozza, M. Marcacci, S. D'Attanasio, B. Magnami, O. Tonet, and G. Megali, "A novel mechatronic tool for computer-assisted arthroscopy," *IEEE transactions on information technology in biomedicine*, vol. 4, no. 1, pp. 15–29, 2000.

[19] S. Phee, W. Ng, I. Chen, F. Seow-Choen, and B. Davies, "Locomotion and steering aspects in automation of colonoscopy. i. a literature review," *IEEE Engineering in Medicine and Biology Magazine*, vol. 16, no. 6, pp. 85–96, 1997.

[20] K. Harada, Z. Bo, S. Enosawa, T. Chiba, and M. G. Fujie, "Bending laser manipulator for intrauterine surgery and viscoelastic model of fetal rat tissue," in *Proceedings 2007 IEEE International Conference on Robotics and Automation*. IEEE, 2007, pp. 611–616.

[21] R. J. Webster, A. M. Okamura, and N. J. Cowan, "Toward active cannulas: Miniature snake-like surgical robots," in *2006 IEEE/RSJ International Conference on Intelligent Robots and Systems*, 2006, pp. 2857–2863.

[22] T. K. Morimoto and A. M. Okamura, "Design of 3-D printed concentric tube robots," *IEEE Transactions on Robotics*, vol. 32, no. 6, pp. 1419–1430, 2016.

[23] R. J. Webster, J. M. Romano, and N. J. Cowan, "Mechanics of precurved-tube continuum robots," *IEEE Transactions on Robotics*, vol. 25, no. 1, pp. 67–78, 2008.

[24] J. Kim, S. Member, W.-y. Choi, and S. Member, "Continuously Variable Stiffness Mechanism Using Nonuniform Patterns on Coaxial Tubes for Continuum Microsurgical Robot," *IEEE Transactions on Robotics*, pp. 1–13, 2019.

[25] Y. Peng, Y. Liu, Y. Yang, N. Liu, Y. Sun, Y. Liu, H. Pu, S. Xie, and J. Luo, "Development of continuum manipulator actuated by thin mckibben pneumatic artificial muscle," *Mechatronics*, vol. 60, pp. 56–65, 2019.

[26] M. C. Yip and D. B. Camarillo, "Model-Less Hybrid Position/Force Control: A Minimalist Approach for Continuum Manipulators in Unknown, Constrained Environments," *IEEE Robotics and Automation Letters*, vol. 1, no. 2, pp. 844–851, 2016.

[27] Z. Du, W. Yang, and W. Dong, "Kinematics modeling of a notched continuum manipulator," *Journal of Mechanisms and Robotics*, vol. 7, no. 4, 2015.

[28] A. Gao, N. Liu, M. Shen, M. E.M.K. Abdelaziz, B. Temelkuran, and G.-Z. Yang, "Laser-Profiled Continuum Robot with Integrated Tension Sensing for Simultaneous Shape and Tip Force Estimation," *Soft Robotics*, vol. 00, no. 00, p. soro.2019.0051, 2020.

[29] J. Zhou, Y. Chen, X. Chen, Z. Wang, Y. Li, and Y. Liu, "A proprioceptive bellows (PB) actuator with position feedback and force estimation," *IEEE Robotics and Automation Letters*, vol. 5, no. 2, pp. 1867–1874, 2020.

[30] S. Li, D. M. Vogt, D. Rus, and R. J. Wood, "Fluid-driven origami-inspired artificial muscles," *Proceedings of the National Academy of Sciences of the United States of America*, vol. 114, no. 50, pp. 13 132–13 137, 2017.

[31] Y. Zhao, Y. Shan, J. Zhang, K. Guo, L. Qi, L. Han, and H. Yu, "A soft continuum robot, with a large variable-stiffness range, based on jamming," *Bioinspiration & biomimetics*, vol. 14, no. 6, p. 066007, 2019.

[32] A. B. Clark and N. Rojas, "Assessing the performance of variable stiffness continuum structures of large diameter," *IEEE Robotics and Automation Letters*, vol. 4, no. 3, pp. 2455–2462, 2019.

[33] J. Peters, E. Nolan, M. Wiese, M. Miodownik, S. Spurgeon, A. Arezzo, A. Raatz, and H. A. Wurdemann, "Actuation and stiffening in fluid-driven soft robots using low-melting-point material," in *2019 IEEE/RSJ International Conference on Intelligent Robots and Systems (IROS)*. IEEE, 2019, pp. 4692–4698.

[34] C. Yang, S. Geng, I. Walker, D. T. Branson, J. Liu, J. S. Dai, and R. Kang, "Geometric constraint-based modeling and analysis of a novel continuum robot with shape memory alloy initiated variable stiffness," *The International Journal of Robotics Research*, p. 0278364920913929, 2020.

[35] A. Shiva, A. Stilli, Y. Noh, A. Faragasso, I. D. Falco, G. Gerboni, M. Cianchetti, A. Menciassi, K. Althoefer, and H. A. Wurdemann, "Tendon-Based Stiffening for a Pneumatically Actuated Soft Manipulator," *IEEE Robotics and Automation Letters*, vol. 1, no. 2, pp. 632–637, 2016.

[36] M. Li, R. Kang, S. Geng, and E. Guglielmino, "Design and control of a tendon-driven continuum robot," *Transactions of the Institute of Measurement and Control*, vol. 40, no. 11, pp. 3263–3272, 2018.

[37] B. Deutschmann, M. Chalon, J. Reinecke, M. Maier, and C. Ott, "Six-DoF Pose Estimation for a Tendon-Driven Continuum Mechanism Without a Deformation Model," *IEEE Robotics and Automation Letters*, vol. 4, no. 4, pp. 3425–3432, 2019.

[38] T. Ren, Y. Li, M. Xu, Y. Li, C. Xiong, and Y. Chen, "A Novel Tendon-Driven Soft Actuator with Self-Pumping Property," *Soft Robotics*, vol. 00, no. 00, pp. 1–10, 2019.

[39] E. Amanov, T.-D. Nguyen, and J. Burgner-Kahrs, "Tendon-driven continuum robots with extensible sections—A model-based evaluation of path-following motions," *The International Journal of Robotics Research*, p. 027836491988604, 2019.

[40] S. Bhattacherjee, S. Chattopadhayay, V. Rao, S. Seth, S. Mukherjee, A. Sengupta, and S. Bhaumik, "Kinematics and Teleoperation of Tendon Driven Continuum Robot," *Procedia Computer Science*, vol. 133, pp. 879–886, 2018.

[41] J. Avery, M. Runciman, A. Darzi, and G. P. Mylonas, "Shape sensing of variable stiffness soft robots using electrical impedance tomography," in *2019 International Conference on Robotics and Automation (ICRA)*. IEEE, 2019, pp. 9066–9072.

[42] X. Cao, M. Zhang, Z. Zhang, Y. Xu, Y. Xiao, and T. Li, "Review of Soft Linear Actuator and the Design of a Dielectric Elastomer Linear Actuator," *Acta Mechanica Solida Sinica*, vol. 32, no. 5, pp. 566–579, 2019.

[43] D. Ji, T. H. Kang, S. Shim, S. Lee, and J. Hong, "Wire-driven flexible manipulator with constrained spherical joints for minimally invasive surgery," *International Journal of Computer Assisted Radiology and Surgery*, vol. 14, no. 8, pp. 1365–1377, 2019.

[44] J. Li, J. Wang, and Y. Fei, "Nonlinear modeling on a SMA actuated circular soft robot with closed-loop control system," *Nonlinear Dynamics*, vol. 96, no. 4, pp. 2627–2635, 2019.

[45] M. Ho, Y. Kim, S. S. Cheng, R. Gullapalli, and J. P. Desai, "Design, development, and evaluation of an MRI-guided SMA spring-actuated neurosurgical robot," *International Journal of Robotics Research*, vol. 34, no. 8, pp. 1147–1163, 2015.

[46] J. Pan, Z. Shi, and T. Wang, "Variable-model SMA-driven spherical robot," *Science China Technological Sciences*, vol. 62, no. 8, pp. 1401–1411, 2019.

[47] C. Cheng, J. Cheng, and W. Huang, "Design and Development of a Novel SMA Actuated Multi-DOF Soft Robot," *IEEE Access*, vol. 7, pp. 75 073–75 080, 2019.

[48] H. Yang, M. Xu, W. Li, and S. Zhang, "Design and Implementation of a Soft Robotic Arm Driven by SMA Coils," *IEEE Transactions on Industrial Electronics*, vol. 66, no. 8, pp. 6108–6116, 2019.

[49] Y. Kim, S. S. Cheng, and J. P. Desai, "Active Stiffness Tuning of a Spring-Based Continuum Robot for MRI-Guided Neurosurgery," *IEEE Transactions on Robotics*, vol. 34, no. 1, pp. 1–11, 2018.

[50] J. Peters, E. Nolan, M. Wiese, M. Miodownik, S. Spurgeon, A. Arezzo, A. Raatz, and H. A. Wurdemann, "Actuation and stiffening in fluid-driven soft robots using low-melting-point material," *IEEE International Conference on Intelligent Robots and Systems*, no. November, pp. 4692–4698, 2019.

[51] J. G. Lee and H. Rodrigue, "Origami-Based Vacuum Pneumatic Artificial Muscles with Large Contraction Ratios," *Soft Robotics*, vol. 6, no. 1, pp. 109–117, 2019.

[52] A. J. Veale, K. Staman, and H. van der Kooij, "Soft, Wearable, and Pleated Pneumatic Interference Actuator Provides Knee Extension Torque for Sit-to-Stand," *Soft Robotics*, vol. 00, no. 00, pp. 1–16, 2020.

[53] R. Kang, Y. Guo, L. Chen, D. T. Branson, and J. S. Dai, "Design of a Pneumatic Muscle Based Continuum Robot with Embedded Tendons," *IEEE/ASME Transactions on Mechatronics*, vol. 22, no. 2, pp. 751–761, 2017.

[54] M. E. Giannaccini, C. Xiang, A. Atyabi, T. Theodoridis, S. Nefti-Meziani, and S. Davis, "Novel Design of a Soft Lightweight Pneumatic Continuum Robot Arm with Decoupled Variable Stiffness and Positioning," *Soft Robotics*, vol. 5, no. 1, pp. 54–70, 2018.

[55] ——, "Novel Design of a Soft Lightweight Pneumatic Continuum Robot Arm with Decoupled Variable Stiffness and Positioning," *Soft Robotics*, vol. 5, no. 1, pp. 54–70, 2018.

[56] G. Agarwal, N. Besuchet, B. Audergon, and J. Paik, "Stretchable Materials for Robust Soft Actuators towards Assistive Wearable Devices," *Scientific Reports*, vol. 6, no. September, pp. 1–8, 2016.

[57] T. M. Bieze, F. Largilliere, A. Kruszewski, Z. Zhang, R. Merzouki, and C. Duriez, "Finite element method-based kinematics and closed-loop control of soft, continuum manipulators," *Soft Robotics*, vol. 5, no. 3, pp. 348–364, 2018.

[58] Y. Hao, T. Wang, Z. Xie, W. Sun, Z. Liu, X. Fang, M. Yang, and L. Wen, "A eutectic-alloy-infused soft actuator with sensing, tunable degrees of freedom, and stiffness properties," *Journal of Micromechanics and Microengineering*, vol. 28, no. 2, p. 024004, 2018.

[59] M. Duduta, E. Hajiesmaili, H. Zhao, R. J. Wood, and D. R. Clarke, "Realizing the potential of dielectric elastomer artificial muscles," *Proceedings of the National Academy of Sciences*, vol. 116, no. 7, pp. 2476–2481, 2019.

[60] H. Zhao, A. M. Hussain, M. Duduta, D. M. Vogt, R. J. Wood, and D. R. Clarke, "Compact Dielectric Elastomer Linear Actuators," *Advanced Functional Materials*, vol. 28, no. 42, pp. 1–12, 2018.

[61] G. Rizzello, P. Serafino, D. Naso, and S. Seelecke, "Towards Sensorless Soft Robotics: Self-Sensing Stiffness Control of Dielectric Elastomer Actuators," *IEEE Transactions on Robotics*, vol. 36, no. 1, pp. 174–188, 2020.

[62] F. Carpi, D. De Rossi, R. Kornbluh, R. E. Pelrine, and P. Sommer-Larsen, *Dielectric elastomers as electromechanical transducers: Fundamentals, materials, devices, models and applications of an emerging electroactive polymer technology*. Elsevier, 2011.

[63] A. Wingert, M. D. Lichter, S. Dubowsky, and M. Hafez, "Hyper-redundant robot manipulators actuated by optimized binary-dielectric polymers," in *Smart Structures and Materials 2002: Electroactive Polymer Actuators and Devices (EAPAD)*, vol. 4695. International Society for Optics and Photonics, 2002, pp. 415–423.

[64] J. Shintake, S. Rosset, B. Schubert, D. Floreano, and H. Shea, "Versatile soft grippers with intrinsic electroadhesion based on multifunctional polymer actuators," *Advanced materials*, vol. 28, no. 2, pp. 231–238, 2016.

[65] S. Dastoor and M. Cutkosky, "Design of dielectric electroactive polymers for a compact and scalable variable stiffness device," in *2012 IEEE International Conference on Robotics and Automation*. IEEE, 2012, pp. 3745–3750.

[66] G. Gu, J. Zou, R. Zhao, X. Zhao, and X. Zhu, "Soft wall-climbing robots," *Science Robotics*, vol. 2874, no. December, pp. 1–13, 2018.

[67] E. B. Joyee and Y. Pan, "A fully three-dimensional printed inchworm-inspired soft robot with magnetic actuation," *Soft robotics*, vol. 6, no. 3, pp. 333–345, 2019.

[68] S. L. Charreyron, Q. Boehler, A. N. Danun, A. Mesot, M. Becker, and B. J. Nelson, "A magnetically navigated microcannula for subretinal injections," *IEEE transactions on biomedical engineering*, vol. 68, no. 1, pp. 119–129, 2020.

[69] S. Jeon, A. K. Hoshiar, K. Kim, S. Lee, E. Kim, S. Lee, J. Y. Kim, B. J. Nelson, H. J. Cha, B. J. Yi, and H. Choi, "A Magnetically Controlled Soft Microrobot Steering a Guidewire in a Three-Dimensional Phantom Vascular Network," *Soft Robotics*, vol. 6, no. 1, pp. 54–68, 2019.

[70] F. Xu, H. Wang, Z. Liu, and W. Chen, "Adaptive Visual Servoing for an Underwater Soft Robot Considering Refraction Effects," *IEEE Transactions on Industrial Electronics*, vol. 67, no. 12, pp. 10 575–10 586, 2020.

[71] B. Yu, J. D. G. Fernández, and T. Tan, "Probabilistic Kinematic Model of a Robotic Catheter for 3D Position Control," *Soft Robotics*, vol. 6, no. 2, pp. 184–194, 2019.

[72] H. Tian, Z. Wang, Y. Chen, J. Shao, T. Gao, and S. Cai, "Polydopamine-Coated Main-Chain Liquid Crystal Elastomer as Optically Driven Artificial Muscle," *ACS Applied Materials and Interfaces*, vol. 10, no. 9, pp. 8307–8316, 2018.

[73] E. Bayraktar, C. B. Yigit, and P. Boyraz, "Object manipulation with a variable-stiffness robotic mechanism using deep neural networks for visual semantics and load estimation," *Neural Computing and Applications*, vol. 32, no. 13, pp. 9029–9045, 2020.

[74] B. Guo and J. Liu, "Real-time tracking with online constrained compressive learning," *IEICE Transactions on Information and Systems*, vol. E96-D, no. 4, pp. 988–992, 2013.

[75] R. B. Scharff, R. M. Doornbusch, E. L. Doubrovski, J. Wu, J. M. Geraedts, and C. C. Wang, "Color-based proprioception of soft actuators interacting with objects," *IEEE/ASME Transactions on Mechatronics*, vol. 24, no. 5, pp. 1964–1973, 2019.

[76] C. Majidi, R. Kramer, and R. Wood, "A non-differential elastomer curvature sensor for softer-than-skin electronics," *Smart materials and structures*, vol. 20, no. 10, p. 105017, 2011.

[77] Z. Xie, F. Yuan, Z. Liu, Z. Sun, E. M. Knubben, and L. Wen, "A Proprioceptive Soft Tentacle Gripper Based on Crosswise Stretchable Sensors," *IEEE/ASME Transactions on Mechatronics*, vol. 25, no. 4, pp. 1841–1850, 2020.

[78] C. Majidi, R. Kramer, and R. J. Wood, "A non-differential elastomer curvature sensor for softer-than-skin electronics," *Smart Materials and Structures*, vol. 20, no. 10, 2011.

[79] T. G. Thuruthel, B. Shih, C. Laschi, and M. T. Tolley, "Soft robot perception using embedded soft sensors and recurrent neural networks," *Science Robotics*, vol. 4, no. 26, 2019.

[80] V. K. Venkiteswaran, J. Sikorski, and S. Misra, "Shape and contact force estimation of continuum manipulators using pseudo rigid body models," *Mechanism and machine theory*, vol. 139, pp. 34–45, 2019.

[81] H. Yang, M. Xu, W. Li, and S. Zhang, "Design and implementation of a soft robotic arm driven by sma coils," *IEEE Transactions on Industrial Electronics*, vol. 66, no. 8, pp. 6108–6116, 2018.

[82] H. Guo, F. Ju, Y. Cao, F. Qi, D. Bai, Y. Wang, and B. Chen, "Continuum robot shape estimation using permanent magnets and magnetic sensors," *Sensors and Actuators A: Physical*, vol. 285, pp. 519–530, 2019.

[83] S. Hasanzadeh and F. Janabi-Sharifi, "Model-Based Force Estimation for Intracardiac Catheters," *IEEE/ASME Transactions on Mechatronics*, vol. 21, no. 1, pp. 154–162, 2016.

[84] S. Song, Z. Li, H. Yu, and H. Ren, "Shape reconstruction for wire-driven flexible robots based on Bézier curve and electromagnetic positioning," *Mechatronics*, vol. 29, pp. 28–35, 2015.

[85] L. T. Gan, L. H. Blumenschein, Z. Huang, A. M. Okamura, E. W. Hawkes, and J. A. Fan, "3D Electromagnetic Reconfiguration Enabled by Soft Continuum Robots," *IEEE Robotics and Automation Letters*, vol. 5, no. 2, pp. 1704–1711, 2020.

[86] X. Ma, P. Wang, M. Ye, P. W. Y. Chiu, and Z. Li, "Shared autonomy of a flexible manipulator in constrained endoluminal surgical tasks," *IEEE Robotics and Automation Letters*, vol. 4, no. 3, pp. 3106–3112, 2019.

[87] J. Lee, J. Wang, and W. Park, "Efficient mechanism design and systematic operation planning for tube-wire flexible needles," *Journal of Mechanisms and Robotics*, vol. 10, no. 6, 2018.

[88] N. Rahman, N. J. Deaton, J. Sheng, S. S. Cheng, and J. P. Desai, "Modular fbg bending sensor for continuum neurosurgical robot," *IEEE robotics and automation letters*, vol. 4, no. 2, pp. 1424–1430, 2019.

[89] C. Wang, C. G. Frazelle, J. R. Wagner, and I. Walker, "Dynamic Control of Multi-Section Three-Dimensional Continuum Manipulators Based on Virtual Discrete-Jointed Robot Models," *IEEE/ASME Transactions on Mechatronics*, vol. 26, no. 2, pp. 777–788, 2020.

[90] A. Parvaresh and S. A. A. Moosavian, "Modeling and model-free fuzzy control of a continuum robotic arm," in *2018 6th RSI International Conference on Robotics and Mechatronics (IcRoM)*. IEEE, 2018, pp. 501–506.

[91] P. Qi, C. Liu, A. Ataka, H.-K. Lam, and K. Althoefer, "Kinematic control of continuum manipulators using a fuzzy-model-based approach," *IEEE Transactions on Industrial Electronics*, vol. 63, no. 8, pp. 5022–5035, 2016.

[92] M. Giorelli, F. Renda, M. Calisti, A. Arienti, G. Ferri, and C. Laschi, "Neural network and jacobian method for solving the inverse statics of a cable-driven soft arm with nonconstant curvature," *IEEE Transactions on Robotics*, vol. 31, no. 4, pp. 823–834, 2015.

[93] M. C. Yip and D. B. Camarillo, "Model-less feedback control of continuum manipulators in constrained environments," *IEEE Transactions on Robotics*, vol. 30, no. 4, pp. 880–889, 2014.

[94] G. Fang, X. Wang, K. Wang, K.-H. Lee, J. D. Ho, H.-C. Fu, D. K. C. Fu, and K.-W. Kwok, "Vision-based online learning kinematic control for soft robots using local gaussian process regression," *IEEE Robotics and Automation Letters*, vol. 4, no. 2, pp. 1194–1201, 2019.

[95] K. Oliver-Butler, J. Till, and C. Rucker, "Continuum robot stiffness under external loads and prescribed tendon displacements," *IEEE Transactions on Robotics*, vol. 35, no. 2, pp. 403–419, 2019.

[96] M. E. Giannaccini, C. Xiang, A. Atyabi, T. Theodoridis, S. Nefti-Meziani, and S. Davis, "Novel design of a soft lightweight pneumatic continuum robot arm with decoupled variable stiffness and positioning," *Soft robotics*, vol. 5, no. 1, pp. 54–70, 2018.

[97] B. Zhao, L. Zeng, Z. Wu, and K. Xu, "A continuum manipulator for continuously variable stiffness and its stiffness control formulation," *Mechanism and Machine Theory*, vol. 149, p. 103746, 2020.

[98] T. G. Thuruthel, E. Falotico, F. Renda, and C. Laschi, "Model-based reinforcement learning for closed-loop dynamic control of soft robotic manipulators," *IEEE Transactions on Robotics*, vol. 35, no. 1, pp. 124–134, 2018.

[99] G. Li, D. Song, S. Xu, L. Sun, and J. Liu, "A hybrid model and model-free position control for a reconfigurable manipulator," *IEEE/ASME Transactions on Mechatronics*, vol. 24, no. 2, pp. 785–795, 2019.

[100] M. Li, R. Kang, D. T. Branson, and J. S. Dai, "Model-free control for continuum robots based on an adaptive kalman filter," *IEEE/ASME Transactions on Mechatronics*, vol. 23, no. 1, pp. 286–297, 2017.

[101] M. Dehghani and S. A. A. Moosavian, "Compact modeling of spatial continuum robotic arms towards real-time control," *Advanced Robotics*, vol. 28, no. 1, pp. 15–26, 2014.

[102] J. Barrientos-Diez, X. Dong, D. Axinte, and J. Kell, "Real-time kinematics of continuum robots: modelling and validation," *Robotics and Computer-Integrated Manufacturing*, vol. 67, p. 102019, 2021.

[103] N. Tan, X. Gu, and H. Ren, "Pose characterization and analysis of soft continuum robots with modeling uncertainties based on interval arithmetic," *IEEE Transactions on Automation Science and Engineering*, vol. 16, no. 2, pp. 570–584, 2018.

[104] X. Gao, X. Li, C. Zhao, L. Hao, and C. Xiang, "Variable stiffness structural design of a dual-segment continuum manipulator with independent stiffness and angular position," *Robotics and Computer-Integrated Manufacturing*, vol. 67, p. 102000, 2021.

[105] P. S. Gonthina, A. D. Kapadia, I. S. Godage, and I. D. Walker, "Modeling variable curvature parallel continuum robots using euler curves," *Proceedings - IEEE International Conference on Robotics and Automation*, vol. 2019-May, pp. 1679–1685, 2019.

[106] P. Abbasi, M. A. Nekoui, M. Zareinejad, P. Abbasi, and Z. Azhang, "Position and Force Control of a Soft Pneumatic Actuator," *Soft Robotics*, vol. 00, no. 00, pp. 1–14, 2020.

[107] D. C. Rucker and R. J. Webster, "Statics and dynamics of continuum robots with general tendon routing and external loading," *IEEE Transactions on Robotics*, vol. 27, no. 6, pp. 1033–1044, 2011.

[108] S. M. Mustaza, Y. Elsayed, C. Lekakou, C. Saaj, and J. Fras, "Dynamic modeling of fiber-reinforced soft manipulator: A visco-hyperelastic material-based continuum mechanics approach," *Soft Robotics*, vol. 6, no. 3, pp. 305–317, 2019.

[109] T. G. Thuruthel, E. Falotico, F. Renda, and C. Laschi, "Model-Based Reinforcement Learning for Closed-Loop Dynamic Control of Soft Robotic Manipulators," *IEEE Transactions on Robotics*, vol. 35, no. 1, pp. 127–134, 2019.

[110] S. Song, Z. Li, M. Q.-H. Meng, H. Yu, and H. Ren, "Real-time shape estimation for wire-driven flexible robots with multiple bending sections based on quadratic bézier curves," *IEEE Sensors Journal*, vol. 15, no. 11, pp. 6326–6334, 2015.

[111] S. Song, Z. Li, H. Yu, and H. Ren, "Shape reconstruction for wire-driven flexible robots based on bézier curve and electromagnetic positioning," *Mechatronics*, vol. 29, pp. 28–35, 2015.

[112] M. S. Sofla, M. J. Sadigh, and M. Zareinejad, "Shape estimation of a large workspace continuum manipulator with fusion of inertial sensors," *Mechatronics*, vol. 80, 12 2021.

[113] I. Singh, Y. Amara, A. Melingui, P. Mani Pathak, and R. Merzouki, "Modeling of continuum manipulators using pythagorean hodograph curves," *Soft robotics*, vol. 5, no. 4, pp. 425–442, 2018.

[114] B. Ouyang, Y. Liu, H.-Y. Tam, and D. Sun, "Design of an interactive control system for a multisection continuum robot," *IEEE/ASME Transactions on Mechatronics*, vol. 23, no. 5, pp. 2379–2389, 2018.

[115] T. Li, L. Qiu, and H. Ren, "Distributed curvature sensing and shape reconstruction for soft manipulators with irregular cross sections based on parallel dual-fbg arrays," *IEEE/ASME Transactions on Mechatronics*, vol. 25, no. 1, pp. 406–417, 2019.

[116] A. Gao, N. Liu, M. Shen, M. EMK Abdelaziz, B. Temelkuran, and G.-Z. Yang, "Laser-profiled continuum robot with integrated tension sensing for simultaneous shape and tip force estimation," *Soft Robotics*, 2020.

[117] H. Guo, F. Ju, and B. Chen, "Preliminary study on shape sensing for continuum robot affected by external load using piecewise fitting curves," in *2019 IEEE International Conference on Robotics and Biomimetics (ROBIO)*. IEEE, 2019, pp. 2414–2420.

[118] L. Scimeca, J. Hughes, P. Maiolino, and F. Iida, "Model-free soft-structure reconstruction for proprioception using tactile arrays," *IEEE Robotics and Automation Letters*, vol. 4, no. 3, pp. 2479–2484, 2019.

[119] R. Roy, L. Wang, and N. Simaan, "Modeling and estimation of friction, extension, and coupling effects in multisegment continuum robots," *IEEE/ASME Transactions on Mechatronics*, vol. 22, no. 2, pp. 909–920, 2016.

[120] J. Till, V. Aloi, and C. Rucker, "Real-time dynamics of soft and continuum robots based on cosserat rod models," *The International Journal of Robotics Research*, vol. 38, no. 6, pp. 723–746, 2019.

[121] D. C. Rucker and R. J. Webster III, "Statics and dynamics of continuum robots with general tendon routing and external loading," *IEEE Transactions on Robotics*, vol. 27, no. 6, pp. 1033–1044, 2011.

[122] R. Yasin and N. Simaan, "Joint-level force sensing for indirect hybrid force/position control of continuum robots with friction," *International Journal of Robotics Research*, vol. 40, pp. 764–781, 2021.

[123] K. P. Ashwin, S. K. Mahapatra, and A. Ghosal, "Profile and contact force estimation of cable-driven continuum robots in presence of obstacles," *Mechanism and Machine Theory*, vol. 164, p. 104404, 2021.

[124] Q. Qiao, G. Borghesan, J. D. Schutter, and E. B. Poorten, "Force from shape - estimating the location and magnitude of the external force on flexible instruments," *IEEE Transactions on Robotics*, vol. 37, pp. 1826–1833, 2021.

[125] J. Lai, K. Huang, B. Lu, Q. Zhao, and H. Chu, "Verticalized-tip trajectory tracking of a 3d-printable soft continuum robot: Enabling surgical blood suction automation," *IEEE/ASME Transactions on Mechatronics*, pp. 1–1, 2021.

[126] Y. Fei, J. Wang, and W. Pang, "A novel fabric-based versatile and stiffness-tunable soft gripper integrating soft pneumatic fingers and wrist," *Soft Robotics*, vol. 6, pp. 1–20, 2019.

[127] W. Hong, F. Feng, L. Xie, and G.-Z. Yang, "A two-segment continuum robot with piecewise stiffness for maxillary sinus surgery and its decoupling method," *IEEE/ASME Transactions on Mechatronics*, pp. 1–11, 3 2022.

[128] J. D. Ho, K.-H. Lee, W. L. Tang, K.-M. Hui, K. Althoefer, J. Lam, and K.-W. Kwok, "Localized online learning-based control of a soft redundant manipulator under variable loading," *Advanced Robotics*, vol. 32, no. 21, pp. 1168–1183, 2018.

[129] K. H. Lee, D. K. Fu, M. C. Leong, M. Chow, H. C. Fu, K. Althoefer, K. Y. Sze, C. K. Yeung, and K. W. Kwok, "Nonparametric Online Learning Control for Soft Continuum Robot: An Enabling Technique for Effective Endoscopic Navigation," *Soft Robotics*, vol. 4, no. 4, pp. 324–337, 2017.

[130] R. A. Manakov, D. Y. Kolpashchikov, V. V. Danilov, N. V. Laptev, I. Skirnevskiy, and O. M. Gerget, "Visual shape and position sensing algorithm for a continuum robot," in *IOP Conference Series: Materials Science and Engineering*, vol. 1019, no. 1. IOP Publishing, 2021, p. 012066.

[131] F. Monet, S. Sefati, P. Lorre, A. Poiffaut, S. Kadoury, M. Armand, I. Iordachita, and R. Kashyap, "High-resolution optical fiber shape sensing of continuum robots: A comparative study," in *2020 IEEE International Conference on Robotics and Automation (ICRA)*. IEEE, 2020, pp. 8877–8883.

[132] Z. Wang, T. Wang, B. Zhao, Y. He, Y. Hu, B. Li, P. Zhang, and M. Q.-H. Meng, "Hybrid adaptive control strategy for continuum surgical robot under external load," *IEEE Robotics and Automation Letters*, vol. 6, no. 2, pp. 1407–1414, 2021.

[133] X. Huang, J. Zou, and G. Gu, "Kinematic modeling and control of variable curvature soft continuum robots," *IEEE/ASME Transactions on Mechatronics*, 2021.

[134] F. Xu, H. Wang, Z. Liu, and W. Chen, "Adaptive visual servoing for an underwater soft robot considering refraction effects," *IEEE Transactions on Industrial Electronics*, 2019.

[135] R. Xu, A. Yurkewich, and R. V. Patel, "Curvature, Torsion, and Force Sensing in Continuum Robots Using Helically Wrapped FBG Sensors," *IEEE Robotics and Automation Letters*, vol. 1, no. 2, pp. 1052–1059, 2016.

[136] H. Zhao, K. O'Brien, S. Li, and R. F. Shepherd, "Optoelectronically innervated soft prosthetic hand via stretchable optical waveguides," *Science Robotics*, vol. 1, no. 1, pp. 1–10, 2016.

[137] S. Mikogai, B. D. Kazumi, and K. Takemura, "Contact Point Estimation along Air Tube Based on Acoustic Sensing of Pneumatic System Noise," *IEEE Robotics and Automation Letters*, vol. 5, no. 3, pp. 4618–4625, 2020.

[138] J. Tapia, E. Knoop, M. Mutný, M. A. Otaduy, and M. Bächer, "MakeSense: Automated Sensor Design for Proprioceptive Soft Robots," *Soft Robotics*, vol. 7, no. 3, pp. 332–345, 2020.

[139] A. Zatopa, S. Walker, and Y. Menguc, "Fully soft 3D-printed electroactive fluidic valve for soft hydraulic robots," *Soft Robotics*, vol. 5, no. 3, pp. 258–271, 2018.

[140] J.-B. Chossat, Y.-L. Park, R. J. Wood, and V. Duchaine, "A soft strain sensor based on ionic and metal liquids," *Ieee sensors journal*, vol. 13, no. 9, pp. 3405–3414, 2013.

[141] V. Arabagi, O. Felfoul, A. H. Gosline, R. J. Wood, and P. E. Dupont, "Biocompatible pressure sensing skins for minimally invasive surgical instruments," *IEEE sensors journal*, vol. 16, no. 5, pp. 1294–1303, 2015.

[142] A. Al-Azzawi, A. M. Boudali, H. Kong, A. H. Göktoğan, and S. Sukkarieh, "Modelling of uniaxial egain-based strain sensors for proprioceptive sensing of soft robots," in *2019 IEEE/RSJ International Conference on Intelligent Robots and Systems (IROS)*. IEEE, 2019, pp. 7474–7480.

[143] C. Tutcu, B. A. Baydere, S. K. Talas, and E. Samur, "Quasi-static modeling of a novel growing soft-continuum robot," *International Journal of Robotics Research*, 2019.

[144] B. Gorissen, D. Reynaerts, S. Konishi, K. Yoshida, J. W. Kim, and M. De Volder, "Elastic Inflatable Actuators for Soft Robotic Applications," *Advanced Materials*, vol. 29, no. 43, pp. 1–14, 2017.

[145] M. Wang, X. Dong, W. Ba, A. Mohammad, D. Axinte, and A. Norton, "Design, modelling and validation of a novel extra slender continuum robot for in-situ inspection and repair in aeroengine," *Robotics and Computer-Integrated Manufacturing*, vol. 67, no. August 2020, p. 102054, 2021.

[146] N. Tan, M. Huang, P. Yu, and T. Wang, "Neural-dynamics-enabled Jacobian inversion for model-based kinematic control of multi-section continuum manipulators," *Applied Soft Computing*, vol. 103, p. 107114, 2021.

[147] M. Giorelli, F. Renda, M. Calisti, A. Arienti, G. Ferri, and C. Laschi, "Neural Network and Jacobian Method for Solving the Inverse Statics of a Cable-Driven Soft Arm with Nonconstant Curvature," *IEEE Transactions on Robotics*, vol. 31, no. 4, pp. 823–834, 2015.

[148] Y. Chen, L. Wang, K. Galloway, I. Godage, N. Simaan, and E. Barth, "Modal-based kinematics and contact detection of soft robots," *Soft Robotics*, 2020.

[149] C. B. Black, J. Till, and D. C. Rucker, "Parallel Continuum Robots: Modeling, Analysis, and Actuation-Based Force Sensing," *IEEE Transactions on Robotics*, vol. 34, no. 1, pp. 29–47, 2018.

[150] I. Van Meerbeek, C. De Sa, and R. Shepherd, "Soft optoelectronic sensory foams with proprioception," *Science Robotics*, vol. 3, no. 24, 2018.

[151] Q. Qiao, D. Willems, G. Borghesan, M. Ourak, J. De Schutter, and E. Vander Poorten, "Estimating and localizing external forces applied on flexible instruments by shape sensing," in *2019 19th International Conference on Advanced Robotics (ICAR)*. IEEE, 2019, pp. 227–233.

[152] V. K. Venkiteswaran, J. Sikorski, and S. Misra, "Shape and contact force estimation of continuum manipulators using pseudo rigid body models," *Mechanism and Machine Theory*, vol. 139, pp. 34–45, 2019.

[153] B. Xiao, W. Xu, J. Guo, H. K. Lam, G. Jia, W. Hong, and H. Ren, "Depth estimation of hard inclusions in soft tissue by autonomous robotic palpation using deep recurrent neural network," *IEEE Transactions on Automation Science and Engineering*, vol. 17, no. 4, pp. 1791–1799, 2020.

[154] R. L. Truby, C. D. Santina, and D. Rus, "Distributed proprioception of 3d configuration in soft, sensorized robots via deep learning," *IEEE Robotics and Automation Letters*, vol. 5, no. 2, pp. 3299–3306, 2020.

[155] L. O. Tiziani and F. L. Hammond, "Optical sensor-embedded pneumatic artificial muscle for position and force estimation," *Soft robotics*, vol. 7, no. 4, pp. 462–477, 2020.

[156] S. Sun, X. Wang, B. Moran, and W. S. Rowe, "A hidden semi-Markov model for indoor radio source localization using received signal strength," *Signal Processing*, vol. 166, p. 107230, 2020.

[157] X. Tong, Y. Su, Z. Li, C. Si, G. Han, J. Ning, and F. Yang, "A double-step unscented kalman filter and HMM-Based zero-velocity update for pedestrian dead reckoning using MEMS sensors," *IEEE Transactions on Industrial Electronics*, vol. 67, no. 1, pp. 581–591, 2020.

[158] E. B. Joyee and Y. Pan, "A fully three-dimensional printed inchworm-inspired soft robot with magnetic actuation," *Soft Robotics*, vol. 6, no. 3, pp. 333–345, 2019.

[159] T. Ranzani, M. Cianchetti, G. Gerboni, I. D. Falco, and A. Menciassi, "A Soft Modular Manipulator for Minimally Invasive Surgery: Design and Characterization of a Single Module," *IEEE Transactions on Robotics*, vol. 32, no. 1, pp. 187–200, 2016.

[160] S. Sefati, R. Hegeman, F. Alambeigi, I. Iordachita, P. Kazanzides, H. Khanuja, R. Taylor, and M. Armand, "A Surgical Robotic System for Treatment of Pelvic Osteolysis Using an FBG-Equipped Continuum Manipulator and Flexible Instruments," *IEEE/ASME Transactions on Mechatronics*, vol. 4435, no. AUGUST, pp. 1–1, 2020.

[161] M. Wang, X. Dong, W. Ba, A. Mohammad, D. Axinte, and A. Norton, "Design, modelling and validation of a novel extra slender continuum robot for in-situ inspection and repair in aeroengine," *Robotics and Computer-Integrated Manufacturing*, vol. 67, no. August 2020, p. 102054, 2021.

[162] D. Rus and M. T. Tolley, "Design, fabrication and control of soft robots," *Nature*, vol. 521, no. 7553, pp. 467–475, 2015.

[163] F. Alambeigi, Y. Wang, S. Sefati, C. Gao, R. J. Murphy, I. Iordachita, R. H. Taylor, H. Khanuja, and M. Armand, "A Curved-Drilling Approach in Core Decompression of the Femoral Head Osteonecrosis Using a Continuum Manipulator," *IEEE Robotics and Automation Letters*, vol. 2, no. 3, pp. 1480–1487, 2017.

[164] N. Sarli and N. Simaan, "Minimal Visual Occlusion Redundancy Resolution of Continuum Robots in Confined Spaces," in *2017 IEEE/RSJ INTERNATIONAL CONFERENCE ON INTELLIGENT ROBOTS AND SYSTEMS (IROS)*, ser. IEEE International Conference on Intelligent Robots and Systems, Bicchi, A and Okamura, A, Ed. IEEE; RSJ; IEEE Robot & Automat Soc; IEEE IES; SICE; New Technol Fdn, 2017, pp. 6448–6454, IEEE/RSJ International Conference on Intelligent Robots and Systems (IROS), Vancouver, CANADA, SEP 24-28, 2017.

[165] X. Xiao, Y. Wu, Q. Wu, and H. Ren, "Concurrently bendable and rotatable continuum tubular robot for omnidirectional multi-core transurethral prostate biopsy," *Medical and Biological Engineering and Computing*, no. 0123456789, 2021.

[166] H. Mo, R. Wei, B. Ouyang, L. Xing, Y. Shan, Y. Liu, and D. Sun, "Control of a flexible continuum manipulator for laser beam steering," *IEEE Robotics and Automation Letters*, vol. 6, pp. 1074–1081, 2021.

[167] E. Franco and A. Garriga-Casanovas, "Energy-shaping control of soft continuum manipulators with in-plane disturbances," *International Journal of Robotics Research*, vol. 40, no. 1, pp. 236–255, 2020.